SPECTROSCOPIC AND STRUCTURAL STUDIES OF METALLOPORPHYRINS AS POTENTIAL MATERIALS FOR NONCOHERENT PHOTON UP-CONVERSION BY TRIPLET-TRIPLET ANNIHILATION ENHANCED SOLAR CELLS

A Thesis Submitted to

The College of Graduate Studies and Research

In Partial Fulfillment of the Requirements

For the Degree of Doctor of Philosophy

In the Department of Chemistry

University of Saskatchewan

Saskatoon

By

Concepcion P. Ponce

© Copyright Concepcion P. Ponce, April, 2016.

All rights reserved.

Permission to use

In presenting this thesis in partial fulfilment of the requirements for a Postgraduate degree from the University of Saskatchewan, I agree that the Libraries of this University may make it freely available for inspection. I further agree that permission for copying of this thesis in any manner, in whole or in part, for scholarly purposes may be granted by Professors Matthew F. Paige and Ronald P. Steer who supervised my thesis work or, in their absence, by the Head of the Department or the Dean of the College in which my thesis work was done. It is understood that any copying or publication or use of this thesis or parts thereof for financial gain shall not be allowed without my written permission. It is also understood that due recognition shall be given to me and to the University of Saskatchewan in any scholarly use which may be made of any material in my thesis.

Requests for permission to copy or to make other use of material in this thesis in whole or part should be addressed to:

The Head

Department of Chemistry

University of Saskatchewan

Saskatoon, Saskatchewan S7N 5C9

Canada

Abstract

Non-coherent photon up-conversion by triplet-triplet annihilation (NCPU-TTA) is a promising approach to improve the incident photon to current conversion efficiency of dye-sensitized solar cell (DSSC). This is because it converts below-band-gap photons, which are normally transmitted through a solar cell, into usable high energy photons. NCPU-TTA involves interaction of two long-lived triplet states of a fluorophore, to produce one molecule in the ground state and one in a higher excited electronic state (i.e. $2T_1 \rightarrow S_2 + S_0$). This interaction has been demonstrated to take place, with good efficiency in both solution and solid state, using closed-shell metalloporphyrin (MP) systems - macromolecules that are related in structure to nature's light harvesting molecules. The implementation of NCPU-TTA in single-threshold cells has been predicted to theoretically increase the maximum efficiency limit from 30% to 40%. Of particular interest to the author is the homomolecular (*homo*-NCPU-TTA) scheme, where the sensitizer and emitter, are one and the same molecules (dual S-E). However, before *homo*-NCPU-TTA can be used in DSSCs, there are many potential problems that need to be investigated and overcome.

Thus, the goal of this thesis is to contribute to a fundamental understanding of conditions needed to implement *homo*-NCPU-TTA in DSSCs. This thesis focuses on problems related to excited state energy losses of MPs to other DSSC components and problems related to controlling distance and mutual orientation of MPs in the solid state, both of which crucially affect NCPU-TTA efficiencies.

First, work on energy loss by collisional quenching of a model MP's excited states with iodide is presented. Iodide is a component of a commonly used redox shuttle in DSSCs and is a known effective fluorescence quencher. Iodide quenching of the S_1 state

can contribute to light to electrical conversion inefficiencies in MP-based DSSCs, while quenching of the S_2 state indicates that there is no advantage of adding the MP up-converter as additional component in DSSCs. Investigation of the photophysical interactions between the S_1 and S_2 excited states of a model MP with iodide ions showed significant quenching of S_1 and a small but noticeable quenching of S_2 fluorescence. The minimal iodide quenching of the S_2 state indicates that no significant loss of efficiency will be introduced by using iodide as component of the electrolyte system in NCPU-TTA enhanced solar cells.

Second, minimization of energy losses arising from the mismatch between the photoanode band gap and upconverted photons of the dye is explored. This thesis approached this problem by tuning the band gap of a semiconductor such that its conduction band energy lies between those of the upconverted and the absorbing states of the model dual S-E, zinc tetraphenylporphyrin (ZnTPP), – *e.g*. *b*etween S_2 and S_1 of ZnTPP. The band gap (E_g) of TiO_2, a common photoanode in DSSCs, lies below the S_1 and S_2 states of ZnTPP. It was expected that ZnTPP will show competing up-conversion (UC) and electron injection processes on TiO_2 as photoanode. On the other hand, the E_g of ZrO_2 lies above ZnTPP's S_2 state and only UC was expected. The introduction of ZrO_2 as a defect in TiO_2 allowed for tuning of its band gap to lie between the ZnTPP's upconverted and prompt S_1 excited states. Optimum electron injection efficiency from the ZnTPP S_2 state was expected for this system. Contrary to expectations, UC was observed for pure and mixed metal oxide films, regardless of the relative energies of the states. Measurements in this study suggested that ZnTPP was heavily aggregated on all metal oxide surfaces and contributed significantly to the observed UC. Thus, controlling MP dye

aggregation was deemed important and explored in the third and fourth projects of this thesis.

Langmuir-Blodgett (LB) deposition was used as a facile means of preparing ordered MP assemblies in thin films. The LB technique requires molecules to be amphiphilic to form stable monolayers. Since ZnTPP is hydrophobic, it was synthetically modified to make it surface-active. The resulting compound, referred to as ZnDATPP, exhibited typical solution phase Soret and Q-bands as well as efficient *homo*-NCPU-TTA observed with ZnTPP. Langmuir films of ZnDATPP showed faceted domains indicative of rigid and crystalline or well-ordered structures. LB films prepared from these monolayers showed UV-Vis spectral shifts consistent with J-aggregation, which was the desired aggregation pattern as studies have shown that J-aggregates can act as energy funnels in photosensitization applications. However, NCPU-TTA was not observed in J-aggregated ZnDATPP films despite the controlled aggregation and close proximity of the molecules. This suggested that both appropriate spatial separation and orientation of MPs were necessary requirements for efficient solid-state *homo*- NCPU-TTA.

In search of the appropriate distance and orientation of MPs, the reticular synthesis strategy of judiciously assembling metal-metalloporphyrin frameworks (MMPFs) was used. MMPFs were made from zinc ions as nodes, and Zn (II) tetrakis(4-carboxyphenyl)porphyrin (ZnTCPP) as a dual S-E strut. This MMPF was referred to as ZMP in this work. In addition, bipyridine (BPY) was used as molecular pillar of ZMP to form a MMPF referred to as ZMPB. Incorporation of these MMPFs into the solid state followed two approaches. First, thin films of MMPFs were prepared using layer-by-layer (LBL) growth. Second, bulk powder MMPFs were prepared and dispersed in polyvinyl

alcohol (PVA) films. Spectroscopic and pXRD data suggested that both MMPFs satisfy Dexter ET distances and assumed approximate face-to-face stacking (H-aggregates). Results of prompt and UC emission measurements suggested that BPY reasonably quenched the S_2 states of ZMPB. ZMP dispersed in PVA, on the other hand, showed measurable UC emission even in aerated conditions. Observation of UC in only one of the MMPFs in this work, despite both of them having small intermolecular distances and adapting similar stacking patterns, points to a complex interplay of processes that need to be investigated further. Observation of *homo*-NCPU-TTA in MPs is inherently difficult due to the low quantum yields of the singlet excited states generated from TTA and to the sensitivity of the triplet states to oxygen. Thus, detecting *homo*-NCPU-TTA for the first time in solid state (and in aerated conditions) shows the great promise of MMPFs as dual S-E molecules and opens them up for further exploration.

There remain additional challenges that must be overcome before *homo*-NCPU-TTA can realistically be implemented in real devices. These are given in Chapter 7. To address some of these challenges, suggestions for future work are also given. These will hopefully serve as guidelines for studies to further improve our understanding of the conditions needed for *homo*-NCPU-TTA or NCPU-TTA, in general, to be incorporated in DSSCs.

Dedication

This thesis is dedicated to:

the late Mauro Q. Ponce who risked rebuke from his own family for sending me, a girl and a younger child, to University. Your words, etched in my heart, kept me going when I felt like giving up. "My little girl, study hard because education is the only treasure I can give you."

my mother, Nenita Palangan-Ponce, for your love and sacrifices.

AND

M. Cynthia Goh for taking me under your wings, treating me like a member of your family, trusting me, encouraging me to dream and for providing me the means to achieve my dreams.

Acknowledgments

No one who achieves a milestone in life does so without looking back to the brilliant mentors and nurturing family and friends who are always there to guide and encourage in every step of the way.

To my mentors, Dr. Matthew F. Paige and Dr. Ron P. Steer, thank you is not enough to express my gratitude for your patience and expert guidance especially when I am stuck and at a loss on how to proceed. To Dr. Paige, thank you for those times you have gracefully but cautiously allowed me to be crazy when I screamed in frustration at my results and looked at everyone with dagger eyes. To the other members of my Academic Committee – Dr. Richard Bowles, Dr. Richard Evitts and the various Graduate Committee Chairs (Dr. Marek Majewski, Dr. Robert Scott, Dr. Michel Gravel, Dr. Stephen Foley) – thank you for mustering the patience to sit and listen to me wiggle out of questions about fundamental aspects of my research; questions that I should have known the answers by then but never did. Thank you for your kindness and understanding in times when I strung so many words into one without pause for breath… because I was just so nervous. Thank you for the constructive criticisms that helped me progress in my research.

For someone who gets deathly scared to push buttons of unfamiliar instruments, this thesis would not have been possible without the expert technical help of these people: Dr. Sophie Brunet, Sunish Sugunan, Neeraj K. Giri, Neeraj K. Joshi, Brook Danger, Phillip Boutin for help with spectroscopy; Nicholas Randell, Kianoosh Poorkazem, Anindya Ganguly, Mahesh Gangishetty for help with instruments in Dr. Tim Kelly's lab; John Hayes, Ester Alluri, Cheng Lu (University of Toronto) for help with pXRD; Ala Eftaiha,

Hessamaddin Younesi, Javeria Rehman for help with AFM, BAM and LB; Dr. Ken Thoms for help with MS and elemental analysis; Dr. Keith Brown for help with NMR; and Rick Elvin and Garth Perry for help with glassworks and electronics.

Of course, I would not have access to a lot of important resources without the SSSC Champions, whose foresight provided this generation of researchers the privilege to use state of the art equipment. I salute Dr. Steer and his colleagues for this legacy. I extend my respect and gratitude to principal investigators – Dr. Andrew Grosvenor, Dr. Robert Scott, Dr. Tim Kelly, Dr. M. Cynthia Goh (University of Toronto) who generously shared their resources so I can freely play with metalloporphyrins, aptly called "*the colors of life".*

Aside from availability of expert personnel and facilities, this thesis has been made possible through grants provided to Dr. Steer and Dr. Paige by the Natural Sciences and Engineering Research Council of Canada via Discovery Grants, the Canadian Foundation for Innovation, Western Economic Diversification and the University of Saskatchewan. I am also grateful for financial grants and awards from the Saskatchewan Innovation and Opportunity Scholarship, Dr. O. Kenneth Johannson Scholarship and M. Cynthia Goh of the University of Toronto.

Life of a graduate student in the sciences does not revolve around the lab bench only. If a student is to become a *compleat* mentor one day, teaching and community involvement is an important component of his or her training. My gratitude goes to Dr. Alexandra Bartole-Scott and Dr. Valerie McKenzie as well as to Dr. Juxia Fu and Dr. Pearson Ahiahonu. Your comments and suggestions on how I can improve my teaching skills are greatly appreciated. The laboratory management techniques that you have

imparted will surely help me when I resume my duties as laboratory instructor and professor at the University of the Philippines. Aside from training me to become a better educator, these friends along with Dr. Marcelo Sales, Dr. Pia Wennek, Linda Connell, Brenda Weenk, Cathy Surtees, Heather Lynchuk, Linda Duxbury, Ronda Duke, Leah Hildebrandt were all out in supporting my teaching and science outreach initiatives outside of the University. Your support helped plant a seed of scientific inquiry in young minds, who will hopefully be the scientists, inventors and innovators of tomorrow.

Speaking of support in science outreach activities, I am grateful to Let's Talk Science, U of S Department of Chemistry, U of S Division of Science Outreach, U of S College of Engineering Outreach and Engagement and Pueblo Science who provided financial and in-kind support to bring science to underserved communities of Saskatchewan. I thank Dr. Reid who tagged me along in his outreach activities and gave me the opportunity to watch how a seasoned demonstrator perform science wonders. Most especially, I thank the volunteers who helped make every outreach activity a fulfilling experience for everyone. There are too many of you to mention but know that you are all volunteers extraordinaire. Thank you for giving your late nights and weekends in preparing outreach materials to make sure our target audience have an unforgettable learning experience.

Given the struggles of academic life – research projects that refused to cooperate; courses that had very high activation barriers to pass; extra-curricular activities that were supposed to balance your load – one can easily break without family and friends who care and lend strength. To my two close friends, Michelle H. and Terri, thank you for being all-around friends: editor; chauffeur, adventure guide, gastronome associate, rant absorber, fitness motivator, etc. To Penny and Wilma, thank you for your motherly care

especially after my surgery. To Lenly G., my BFF, thank you for your unwavering friendship. To Michelle Li, Louis, Myron and Ronnie, thank you for the good conversations. To Ate Jane and Rich L, thank you for the sumptuous dinners and helpful synthesis tips. To all my friends in my friendship circles below, who made a difference in my graduate student life, thank you for the good company and good cheer; thank you for making my stay in Saskatoon and Toronto memorable. To my colleagues at the University of the Philippines, thank you for taking my academic load in my absence. To my family, thank you for always being there for me. And last but not least, I thank my God for all the blessings. To Him be the glory.

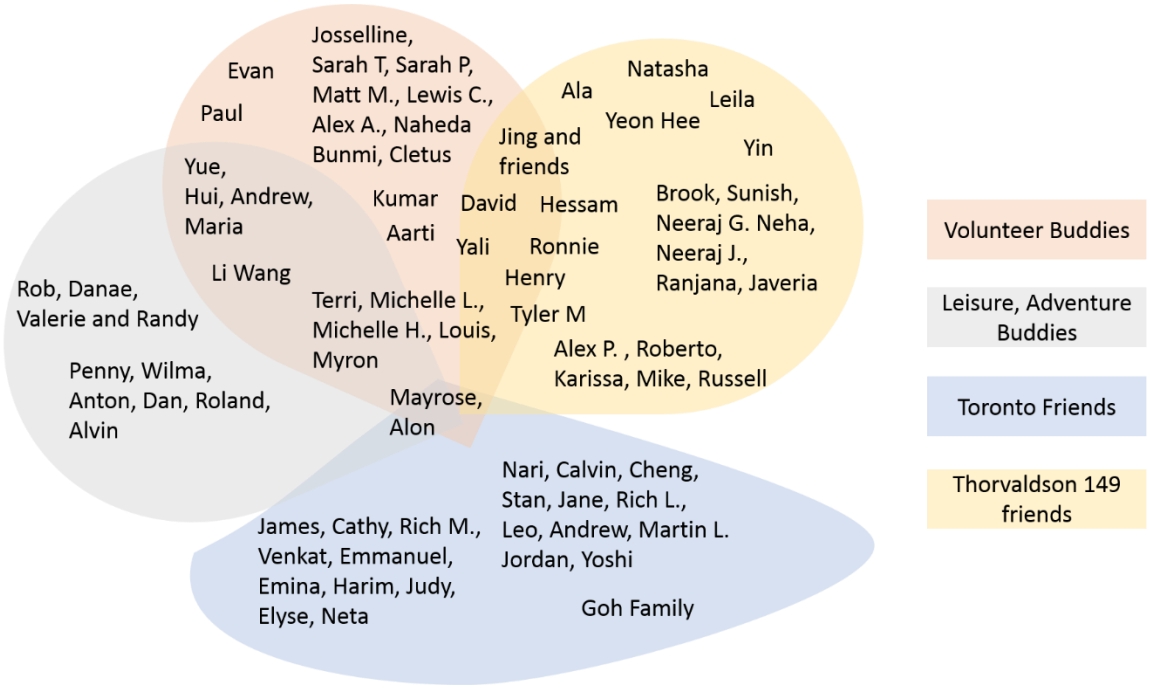

My Friendship Circles

List of Papers

1. Ponce, C. P.; Steer, R. P.; Paige, M. F., Photophysics and halide quenching of a cationic metalloporphyrin in water. *Photochemical & Photobiological Sciences* **2013,** 12, (6), 1079-1085.
2. Giri, N. K.; Ponce, C. P.; Steer, R. P.; Paige, M. F., Homo-molecular non-coherent photon up-conversion by triplet-triplet annihilation using a zinc porphyrin on wide bandgap semiconductors. *Chemical Physics Letters* **2014,** 598, 17-22.
3. Ponce, C.P.; Araghi, H.Y.; Joshi, N.K.; Steer, R.P.; and Paige, M.F. Spectroscopic and structural studies of a surface active porphyrin in solution and in Langmuir-Blodgett films. *Langmuir* **2015**, 31, (50), 13590-13599

Table of Contents

List of Tables

List of Figures

List of Abbreviations

A	absorbance
ADB	4’4-(anthracene-9,10-diyl)-dibenzoate
AFM	atomic force microscopy
APTMS	3-aminopropyltrimethoxysilane
ASPT	trans-4-[P-(N-ethyl-N-hydroxylethyl-amino)styryl]-N-methylpyridinium tetraphenylborate
BAM	Brewster angle microscopy
BPY	4,4'-bipyridine
btc	benzenetricarboxylate
dabco	1,4-diazabicyclo[2,2,2]-octane
DEF	N,N-diethylformamide
DMF	N,N-dimethylformamide
DMSO	dimethylsulfoxide
DPA	9,10-diphenylanthracene
DSSC	dye-sensitized solar cell
E	Energy
ESI	electrospray ionization
ET	energy transfer
F	fluorescence
FC	Franck-Condon
FCF	Franck-Condon factor
HOMO	highest occupied molecular orbital
I	intensity
IC	internal conversion
ISC	intersystem crossing
ITO	indium-tin oxide
IUPAC	International Union of Pure and Applied Chemistry
IVR	internal vibrational relaxation
LB	Langmuir-Blodgett

LBL	layer-by-layer assembly
LBO	Lithium triborate, $LiBr_3O_5$
LFP	laser flash photolysis
LMCT	ligand to metal charge transfer
LUMO	lowest unoccupied molecular orbital
MCP-PMT	micro channel plate photomultiplier tube
MLCT	metal to ligand charge transfer
MMA	mean molecular area
MMPF	metal-metalloporphyrin framework
MOF	metal organic framework
MP	metalloporphyrin
MS	mass spectroscopy
NCPU	noncoherent photon up-conversion
Nd-YAG	neodymium-doped yttrium aluminium garnet; $Nd:Y_3Al_5O_{12}$
P	phosphorescence
PMMA	poly(methylmethacrylate)
p-n	Positive-negative
PV	Photovoltaic
Q	quencher
QToF	quadruple time of flight
RET	resonance energy transfer
RMS	root-mean-square
S	singlet
S-E	sensitizer-emitter pair
SV	Stern-Volmer
T	triplet; transmittance; temperature
TA	transient absorption
TCSPC	time-correlated single photon counting
TEM	transmission electron microscopy
TLC	thin layer chromatography
TTA	triplet-triplet annihilation

TTET	triplet-triplet energy transfer
UC	up-conversion
XRD	X-ray diffraction
ZMP	zinc-metalloporphyrin framework
ZMPB	zinc-metalloporphyrin-bipyridine framework
ZnATPP	5-(4-aminophenyl)-10,15,20-triphenylporphyrin zinc (II)
ZnDATPP	5-(4-N-diglycolic acid aminophenyl)-10,15,20-triphenylporphyrin zinc (II)
ZnTCPP	5,10,15,20-(4-carboxyphenyl) porphyrin zinc (II)
ZnTMPyP	tetrakis(N-methyl-4-pyridyl)porphyrin zinc (II) tetrachloride
ZnTPP	5,10,15,20-tetraphenylporphine zinc(II)

List of Symbols

A	absorbance
k_B	Boltzmann constant
β	Full width at half maximum
$C_{\infty v}$	point group symmetry for linear molecules; anti-symmetric with respect to C_2 perpendicular to the principal axis
D	diffusion coefficients; donor molecule; crystallite size
$D_{\infty h}$	point group symmetry for linear molecules; symmetric with respect to C_2 perpendicular to the principal axis
$\Delta G°$	Change in Gibb's Free energy
ΔX	Change in quantity X
e	electronic coordinates; charge of an electron
ε	molar absorptivity
E	energy
E_g	band gap energy
Φ	quantum yield
F	fluorescence
f	fraction
g	gerade
γ	quenching efficiency
η	solar incident photon to current efficiency
h	Planck's constant; thickness of LB or LBL films
I_n	Light Intensity
K_{SV}	Stern-Volmer constant
k_X	rate constant where X represents an event in which rate of change is monitored
λ	wavelength
l	light path length
[ ] or M	Molar concentration
$\overrightarrow{M_{21}}$	transition dipole moment from Ψ_1 to Ψ_2
n	nuclear coordinates; refractive index
N_A	Avogadro's number
N_{Sn}	population of molecules at the state S_n
Π	Molecular term symbol when the projection of the orbital angular momentum along the internuclear axis, $\Lambda = 1$
θ	Bragg diffraction angle
R	sum of radii of atoms/ions in an encounter pair
r_c	Onsager length

Σ	$\Lambda = 0$; summation
σ	absorption cross section
T	temperature
t	time
τ	lifetime
u	ungerade
$\hat{\mu}$	transition dipole moment operator
V	quenching sphere volume
Ψ_n	wavefunction
Z_n	charge of ion n
Λ	total angular momentum

CHAPTER 1. INTRODUCTION AND LITERATURE REVIEW

Increasing world population and continuing rise in consumer societies are putting the global energy system under stress. The world's energy consumption is estimated at 100 000 TWh and is forecasted to increase by 40% in 2040.[1, 2] The bulk of these energy needs is satisfied by nonrenewable resources such as oil, natural gas and coal.[2] While these nonrenewable resources remain easily accessible and cheap, they are used at a much faster rate than they are produced. In addition to dwindling supplies, concerns on the impact of overconsumption of these non-renewable resources on the environment are growing. The growing realization of the need for sustainable use of resources has motivated world governments to support development of energy sources that are accessible, affordable, inexhaustible and environment friendly.[3]

1.1 Solar Photovoltaics

Solar energy is abundant, non-greenhouse gas producing and free – which makes it an attractive alternative to fossil fuels. Technologies that harness the energy from the sun and convert it to electricity, called solar photovoltaics (PVs), have their beginnings more than a century ago but their solar conversion efficiencies, η, were too low for widespread use.[4] The first practical use of PVs was demonstrated by Bell Labs in 1954 with their single p-n junction silicon based solar cell powering a toy Ferris wheel and a radio transmitter.[4, 5] These early solar cells (also called first generation or traditional solar cells) were expensive to produce. Moreover, they were not sufficiently efficient for mainstream use and were relegated to supplying power to earth-orbiting satellites. In these instances, cheap non-renewables were not accessible and chemical batteries ran the risk of running out in days, thereby jeopardizing the satellite's operations.[4] Since then,

improvements in solar cell design, advances in materials and development of emerging technologies have made PVs useful in non-space applications, such as in powering devices and equipment in facilities far from power lines or supplying electricity to households in remote locations. Further advances in solar cell technology have made possible their mainstream use as seen in the increasing numbers of solar farms around the world for large-scale power generation.

However, solar PVs are not yet competitive with cheap fossil fuels. For PVs to be competitive, the cost of production has to go down further and conversion efficiency must improve. With traditional PVs, there is a limit to how much production cost can be reduced, thus, there has been a significant research thrust aimed at the development of cheaper materials.

1.2 Dye-Sensitized Solar Cells

The challenge of making solar PVs cost-effective can be met by dye sensitized solar cells (DSSCs), which were pioneered by the group of Michael Grätzel.[6] In a DSSC, dye molecules are adsorbed to a metal oxide (most commonly TiO_2) surface. A current is generated when a dye molecule absorbs a photon, enters an excited electronic state and injects an electron into the conduction band of the metal oxide photoanode. The circuit is completed when the dye is regenerated by electron transfer by a redox system – typically an I^-/I_3^- redox couple dissolved in a low volatility solvent. The electrolyte system is in turn reduced at the counter electrode (see diagram in Figure 1.1).[6, 7] DSSCs have attracted considerable attention as they make use of relatively cheap materials and can be manufactured with ease and without the use of elaborate equipment. However, the efficiency of DSSCs does not yet match the performance provided by solid state

photovoltaics.[6-8] Single junction gallium arsenide based PVs recorded η of >40% while silicon based PVs have η of >20%.[8] Champion DSSCs have η of *ca.* 10%.[8] Thus, much of the research activities on DSSCs are centered on improving their η primarily by changing the structure, morphology or nature of the semiconductor electrode;[9] designing panchromatic sensitizer dyes[10] with efficient anchoring groups;[11] or making use of low volatility [12] or polymer based electrolytes.[13]

Another approach to improving DSSC performance that is of particular relevance in this thesis is to make more efficient use of the solar spectrum. The solar spectrum is rich in red/near IR photons and current solar cell technology is highly inefficient at collecting and using these photons. Recently, it has been suggested that photon up-conversion, that is, the conversion of two low-energy photons into one higher energy photon or excited state, has potential for improving DSSC conversion efficiency through up-conversion of red and near-IR solar photons.[14-16] This has been shown to take place in metalloporphyrin (MP) systems by the photophysical process triplet-triplet annihilation (TTA) with decent efficiency, both in solution and in the solid state.[17, 18] However, there are aspects of NCPU-TTA that are not yet well-understood. Thus, the main purpose of this PhD research is to provide a fundamental understanding of the spectroscopic properties of MP molecules that have potential application as NCPU sensitizers in DSSCs. As can be seen in Figure 1.1, a DSSC is a complex device and its efficiency is affected by an interplay of various processes in the system. Incorporating NCPU-TTA into a DSSC device requires an understanding of how these processes or parameters affect NCPU-TTA efficiency. The succeeding sections in this chapter give a brief review of these processes and parameters in relation to the general mechanism of NCPU-TTA.

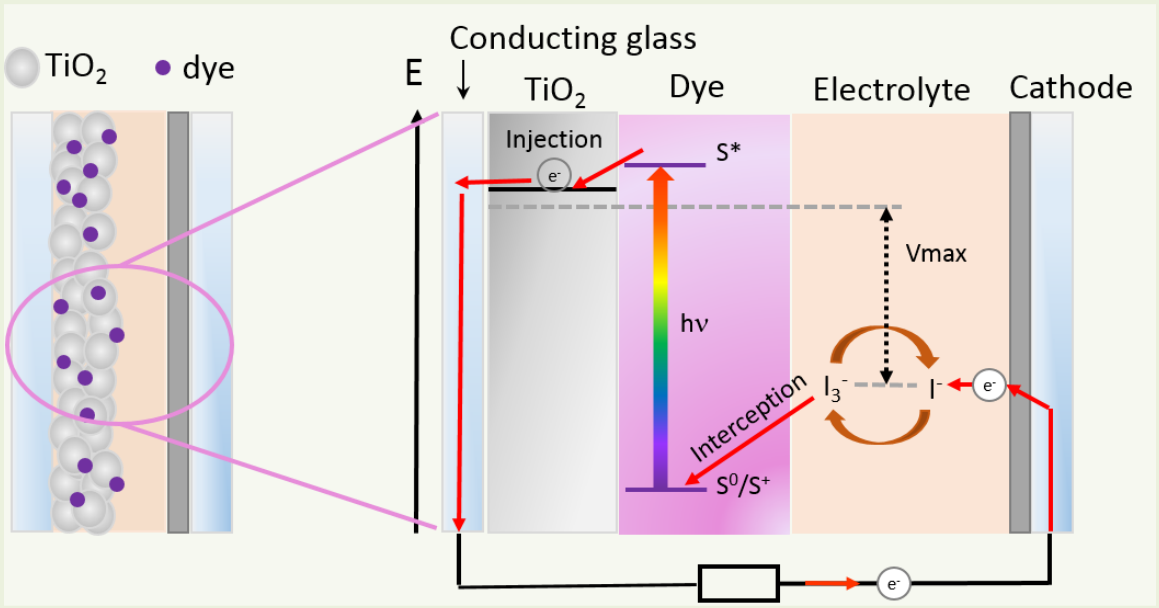

Figure 1.1 Schematic illustration of the working principles of Grätzel's DSSC. Adapted and redrawn from Grätzel (2001).[19]

1.3 Transmission Losses in DSSCs

The low efficiencies of all PVs are the result of an interplay of various factors. In the case of solar PVs based on p-n junction cells, the η limit is known as the Shockley-Quiesser limit. Shockley and Quiesser estimated the theoretical efficiency for a semiconductor with a band gap energy (E_g) of 1.1 eV (band gap of Si) to be *ca.* 33% based on these energy losses: (1) radiative recombination; (2) radiative losses; (3) vibrational relaxation following absorption of photons of energy greater than E_g; and (4) transmission losses when the energy of the incident photons is less than E_g.[20] The last two losses comprise majority of the energy losses in single junction PVs, accounting to about 48% and are a consequence of the mismatch between the solar spectrum and the single threshold of the absorber.[21]

DSSCs or organic PVs in general, convert incident photons to electricity by a fundamentally different mechanism, thus, the factors limiting their efficiencies are also different. Nevertheless, DSSCs are also adversely affected by the above-mentioned transmission loses since even the best performing sensitizer dyes absorb only a portion of the solar spectrum, typically the UV-Vis region, and waste photons from the red-near infrared (IR) region.[22] This is where photon up-conversion can be important. Up-converting red/near IR photons into radiation usable by the sensitizer dye recovers some of these transmission losses and can potentially increase η of PVs.

1.4 Photon Up-conversion

As noted above, photon up-conversion is the process in which higher energy photons are generated by simultaneous or sequential absorption of two or more photons with lower energy. This is an emerging technique that can be used to increase the efficiency of solar cells.

Potential improvements in the efficiency of solar cells when combined with an inorganic up-converter have been calculated by Trupke *et al*.[15] Using different cell geometries and different illumination conditions, they have predicted that the upper limit of the energy conversion efficiency of a bifacial solar cell with an up-converter behind it is 63.2% for concentrated sunlight and 47.6% for nonconcentrated sunlight. In 2006, the group extended their theoretical treatment of UC systems to realistic air mass spectra and also presented proof of principle experimental results.[23] They used a prototype consisting of bifacial silicon solar cell with $NaYF_4:Er^{3+}$ up-conversion phosphor attached to the backside and have shown that the system performed better than solar cells employing the impurity photovoltaic effect in silicon.[23] To date the most well studied

phosphors for up-conversion in solar cell applications are the Er^{3+} or Yb^{3+} doped $NaYF_4$. [23-27] Several workers explored the use of other rare earth ions and up-conversion host materials to silicon solar cells but the predicted solar cell efficiency enhancement is not so significant.[28, 29] The mechanism of up-conversion in the systems cited above involves ground state absorption followed by an energy transfer up-conversion. The active ion absorbs energy and becomes electronically excited. It then transfers energy to the neighboring ion (also in the excited state) giving rise to high energy photons. [25, 26, 29]

The concept of combining an UC phosphor with solar cells has been extended to systems other than silicon. For example, Shan and Demopolous[30] used rare earth doped metal oxides layered on the TiO_2 electrode as up-conversion materials in DSSC. These groups have shown that the UC-TiO_2 layer absorbs infrared light and emits green light which is then absorbed by the N719 dye used in their experiments, thus improving the sunlight conversion efficiency of the dye sensitized solar cell.

Aside from inorganic phosphors, up-conversion has been demonstrated in organic materials as well. Up-conversion in organic materials such as in trans-4-[P-(N-ethyl-N-hydroxylethyl-amino)styryl]-N-methylpyridinium tetraphenylborate (ASPT) occurs via a multi-photon process in which two or more photons of longer wavelength from a high power pulsed laser are simultaneously absorbed by the dye and up-converted to shorter wavelengths.[31] However, multi-photon processes are not ideal for DSSC applications because of the difficulty of finding a suitable dye with large multi-photon absorption cross sections. Moreover, the requirement of excitation with high power per unit area generally requires the use of coherent light sources, and thus solar photons are not useful.[32] A more practical approach to photon up-conversion using organic materials is by exploiting the

process of triplet-triplet annihilation (TTA) which can be effected by non-coherent and low power excitation sources. This is discussed in the following section with particular emphasis on MPs as model compounds exhibiting the TTA process.

1.5 NCPU-TTA in ZnTPP and its derivatives

1.5.1 Overview

NCPU-TTA involves a sensitizer and an emitter (S-E). The S-E system can be composed of two distinct chromophores (heteromolecular NCPU-TTA) or of identical molecules that can function as dual sensitizer and emitter (*homo*-NCPU-TTA). This work mostly deals with MPs as sensitizers in NCPU-TTA. In particular, 5,10,15,20-tetraphenylporphine zinc(II) (ZnTPP) (or its derivatives) can serve as both the sensitizer and emitter in the *homo*-NCPU-TTA scheme.

MPs are among the few organic materials that readily exhibit NCPU-TTA. They are metallated derivatives of the deeply colored compounds containing the porphine basic structure (Figure 1.2), an aromatic macrocycle composed of four modified pyrrole subunits interconnected in their alpha carbons via methine bridges.[33] Figure 1.2 show the structure of the porphine central ring and the various MPs used in this thesis.

MPs have been of interest since the early 20th century owing to their tunable electronic properties and thus their functionalities. The electronic absorption spectra of MPs show a strong band in the visible region at around 400 nm, called the Soret band and weaker absorption in the 470-700 nm region, called the Q bands.[33, 34] Both the Soret and Q bands arise from transitions between two nearly degenerate highest occupied molecular orbitals (HOMOs) to the first two lowest unoccupied degenerate molecular

orbital (LUMOs) of the molecule (discussed in detail in Section 1.5.2). The identities of the metal center and the substituents on the porphine ring affect the relative energies of these transitions. The environment surrounding the macrocycle also affect the electronic spectroscopic properties of the molecule.[33, 34] Thus, changing the metal centers or substituting functional groups around the porphine macrocycle give a variety of applications ranging from photodynamic therapy, optoelectronic devices, catalysis, dyes and coatings, alternative energy generation etc.[33, 34]

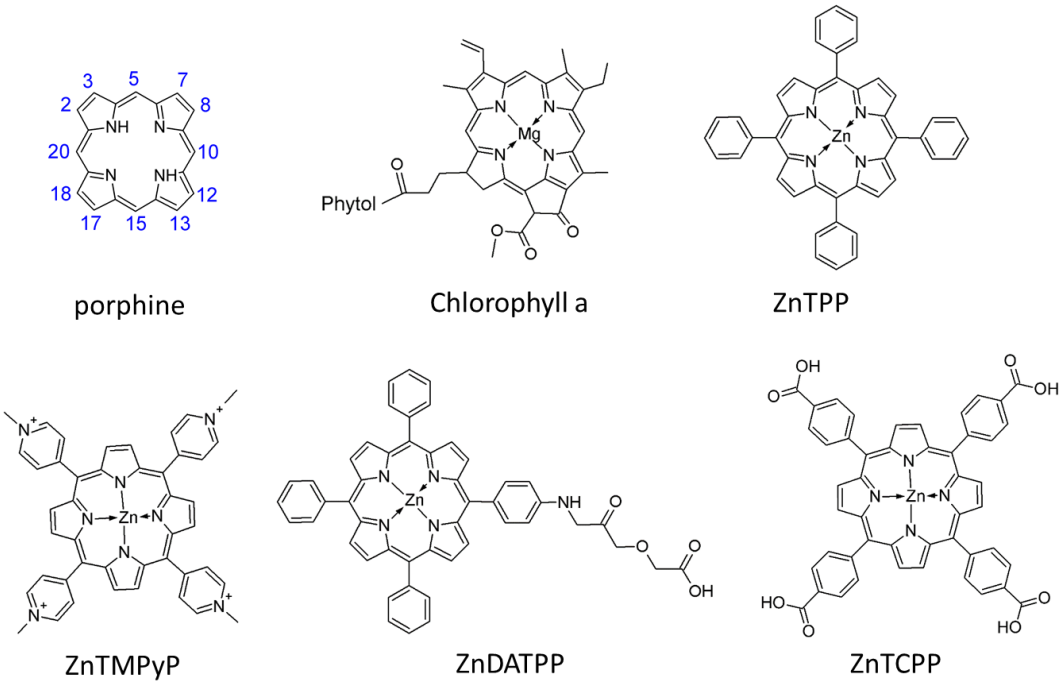

Figure 1.2 Structures of MPs used in this study. The structures of porphine and its IUPAC numbering system and of chlorophyll a are also shown for comparison.

To facilitate understanding of the photophysical processes involved in NCPU-TTA involving MPs, the shape and position of the electronic spectra of MPs are discussed on the basis of selection rules and the symmetry of the central macrocycle in MPs. The

following notations are used to represent the different energy levels in MPs: 1) the lowest electronic energy state or the ground state of the MP dye molecule belonging to the D_{4h} point group symmetry has an A_{1g} symmetry and is an $^1A_{1g}$ state – this is denoted as S_0; 2) the first singlet excited state has an E_u symmetry and is an ^1E_u state – this is denoted as S_1 3) S_2 is the second singlet excited state, 2 ^1E_u; 4) T_1 is the lowest triplet state, 1 ^3E_u. The orbital configurations of the singlet and triplet state are shown in Figure 1.3.

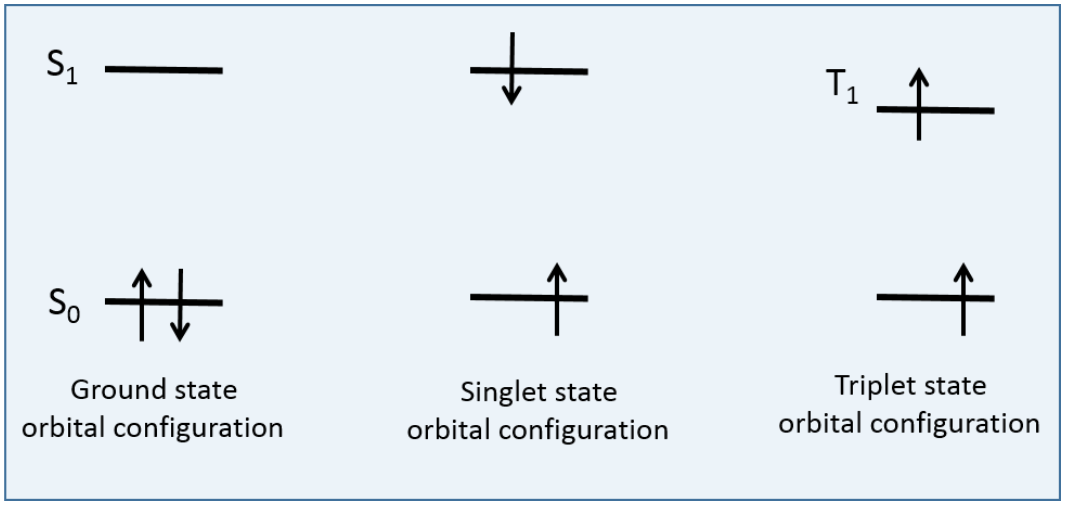

Figure 1.3. Orbital configurations of singlet and triplet state.

The mechanism of *homo*-NCPU-TTA is illustrated in the form of a Jablonski diagram in Figure 1.4. The first step involves absorption of low energy photons by the sensitizer with subsequent excitation into the lowest singlet excited state (1.1). By intersystem crossing (ISC), the singlet excited state is converted into the triplet state (1.2). Two molecules in the triplet state can then annihilate each other and form a molecule in the second (or higher) singlet excited state and a molecule in the ground state (1.3). Finally, the S_2 state formed from TTA relaxes back to the ground state by emitting a photon that is higher in energy than the absorbed photon. Details of these processes relevant to

understanding NCPU-TTA are discussed in the succeeding subsections and are based on textbooks by Kelley,[35] Lakowicx[36] and Turro[37] with additional references given in the text as needed. More detailed discussions of these principles are provided in these sources.

$$S_0 + h\nu_{low} \rightarrow S_1 \quad (1.1)$$

$$S_1 \rightarrow T_1 \quad (1.2)$$

$$T_1 + T_1 \rightarrow S_0 + S_2 \quad (1.3)$$

$$S_2 \rightarrow S_0 + h\nu_{high} \quad (1.4)$$

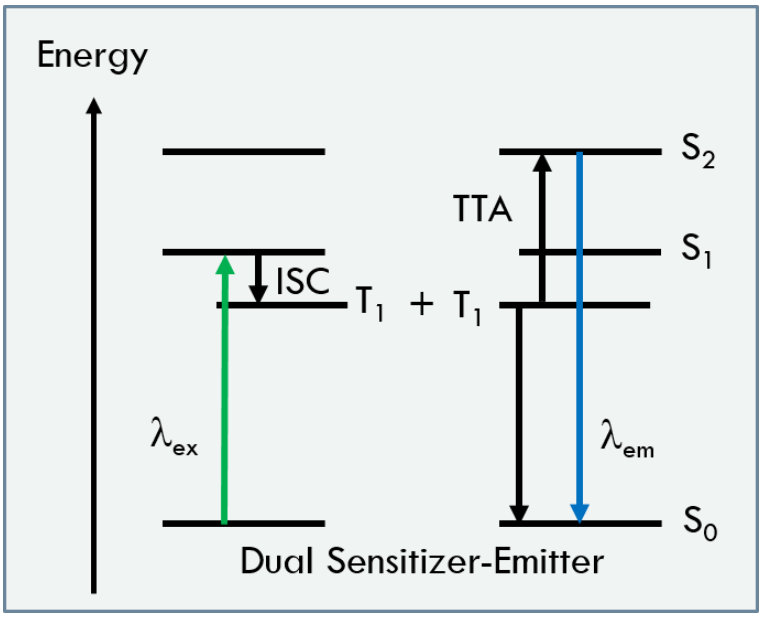

Figure 1.4 Simplified diagram of the photophysical processes involved in *homo*-NCPU-TTA.

1.5.2 Electronic Absorption of ZnTPP

The probability and strength of electronic transitions can be described with reference to selection rules. These selection rules determine whether a transition is allowed or forbidden. To understand these selection rules, an overview of transition moment is given.

Molecular electronic absorption is viewed as light-matter interaction in which the electric component of an oscillating electromagnetic radiation field can induce an oscillating electric moment in a molecule. This light-matter interaction is said to be tresonant if the frequency of the induced electric moment is the same as the energy difference between the lower state given by the wavefunction, Ψ_1, and upper state given by Ψ_2. The strength of light-matter interaction that causes transition from Ψ_1 to Ψ_2 is generally given by the transition moment integral:

$$\vec{M}_{21} = \int \Psi_2^* \hat{\mu} \Psi_1 d\tau \quad (1.5)$$

$$\hat{\mu} = \hat{\mu}_n + \hat{\mu}_e \quad (1.6)$$

where $\vec{M}_{21}$ is the transition dipole moment from Ψ_1 to Ψ_2 and $\hat{\mu}$ is the transition dipole moment operator which depends on the electronic and nuclear coordinates denoted with subscripts e and n in equation 1.6, respectively. As with probability density, the probability of the transition is given by $\left|\vec{M}_{21}\right|^2$. The transition between eigenstates Ψ_1 and Ψ_2 is electric dipole allowed if $\vec{M}_{21} = \int \Psi_2 \hat{\mu} \Psi_1 d\tau \neq 0$. The transition moment integral itself does not need to be calculated to determine the selection rule as long as the symmetry of the transition moment function, $\Psi_2 \hat{\mu} \Psi_1$, is known. Ψ is a complex function and detailed treatment of this function is beyond the scope of this introduction. However, it is noted

that based on the Born-Oppenheimer approximation, which assumes that the motion of atomic nuclei and electrons in a molecule are separable, that is, Ψ can be separated into electronic (ψ_{es}), vibrational (ψ_v), and rotational (ψ_r) parts and the electronic wavefunction further separated into the orbital (ψ_e) and spin (ψ_s), wavefunctions. Mathematically, this can be written as

$$\Psi = \psi_{es}\psi_v\psi_r \tag{1.7}$$

Applying (1.6) and (1.7) to the square of (1.5) and ignoring the rotational part of Ψ gives the transition probability as:

$$\left|\vec{M}_{21}\right|^2 = \left[\int (\psi_{es2}\psi_{v2})^* (\hat{\mu}_n + \hat{\mu}_e)(\psi_{es1}\psi_{v1})\, d\tau\right]^2 \tag{1.8}$$

Integrating (1.8) in two parts, with μ_e and μ_n, respectively gives a product of two integrals shown in (1.9) that form the basis of electronic absorption selection rules.

$$\left|\vec{M}_{21}\right|^2 = \left[\left\{\int \psi^*_{es2}\hat{\mu}_e\psi_{es1}d\tau_{es}\int \psi^*_{v2}\psi_{v1}d\tau_v\right\} + \left\{\int \psi^*_{v2}\hat{\mu}_n\psi_{v1}d\tau_v\int \psi^*_{es2}\psi_{es1}d\tau_{es}\right\}\right]^2 \tag{1.9}$$

The electronic wavefunction (ψ_{es}) contains both spatial and spin parts, but the dipole moment operator acts only on spatial coordinates. In addition, electronic wavefunctions are orthogonal making $\psi_{es2}\psi_{es1} = 0$. The second term on the right hand side (RHS) of (1.9) vanishes, thus simplifying it to:

$$\left|\vec{M}_{21}\right|^2 = \left[\left\{\int \psi^*_{e2}\hat{\mu}_e\psi_{e1}d\tau_e\int \psi^*_{s2}\psi_{s1}d\tau_s\int \psi^*_{v2}\psi_{v1}d\tau_v\right\}\right]^2 \tag{1.10}$$

The first two integrals on the RHS of (1.10) defines the electronic transition rules while the last integral defines the vibrational selection rule. On the basis of (1.10) being

nonzero, electronic transition selection rules (which take into account the total orbital angular momentum along the molecular axis, parities and spin multiplicities of the molecule) are summarized below.

1. Orbital selection rule: the total angular momentum change should be $\Delta\Lambda = 0$ for $\Sigma \leftrightarrow \Sigma$ transition and $\Delta\Lambda = \pm 1$ for $\Sigma \leftrightarrow \Pi$ transitions where Σ and Π are labels for the absolute magnitude of the orbital angular momentum. A given electronic transition is electric dipole allowed ($\psi_{e2}^{*}\hat{\mu}_e\psi_{e1} \neq 0$) if the direct product of the symmetry species of the initial state, the final state, and the operator involved contains the totally symmetric irreducible representation of the symmetry point group of the molecule (*e.g.* $\Sigma^+ \leftrightarrow \Pi$ in heteronuclear diatomic with $C_{\infty v}$ symmetry or $\Sigma_g^+ \leftrightarrow \Pi_u$ in $D_{\infty h}$ are allowed transitions).

2. Laporte selection rule: for centrosymmetric molecules, transitions are only allowed between states having different parity (symmetry of the molecular wavefunction reflecting against its symmetry axis). For example, in molecules with $D_{\infty h}$ symmetry, $g \leftrightarrow u$ is allowed while $g \leftrightarrow g$ and $u \leftrightarrow u$ are both forbidden. Distortions in the molecule or the presence of vibronic coupling give rise to observation of electronic absorption of symmetry forbidden transitions.

3. Spin selection rule: spin cannot change ($\Delta S = 0$) since states of different spin multiplicity are orthogonal and will make $\psi_{s2}^{*}\psi_{s1} = 0$. Thus, only transitions between different singlet states or between different triplet states are allowed, but transitions between a singlet and a triplet, for example, are spin-forbidden. Singlet to triplet transitions can be observed in molecules when there is spin-orbit coupling but the interaction is generally weak.

The last integral in (1.10) is related to the strength of vibrational overlap of the ground state and excited state and is called the Franck-Condon factor (FCF) when calculated with Condon approximation. The Condon approximation imposes further restriction in the electronic transition – that is, the electronic transition occurs on a shorter time scale compared to nuclear motion so that the transition probability can be calculated at a fixed nuclear position. The FCF determines the relative intensity of the vibrational bands in electronic absorption spectra, whose overall intensity is given by the electronic part. Given that the total intensity of an electronic transition is distributed among all possible vibrational transitions and that these possible transitions increase in number as the number of atoms increases, electronic spectra do not appear as sharp lines but as a set of closely spaced lines which may be partially resolved or completely unresolved resulting in a broad absorption band. Figure 1.5 shows a Jablonski diagram of the excitation of a molecule from the lowest vibrational level of the electronic ground state (S_0) to a number of vibrational levels in the S_1 (green upward arrows) and S_2 (blue upward arrows) excited states. These higher energy states are referred to as Franck-Condon (FC) excited states.

Thus far, selection rules, which affect the intensity of the absorption spectra of MPs, have been discussed. The symmetry of MPs will now be discussed in more detail.

Figure 1.2 shows that the various MPs used in the majority of this work are derivatives of ZnTPP, and so, the following discussion centers around the point group symmetry of ZnTPP and its relation to the observed absorption spectra described in Section 1.5.1. The porphine central ring of ZnTPP has D_{4h} symmetry. The four-orbital model devised by M. Gouterman[38] gave the HOMOs of D_{4h} MPs to be a_1u and a_2u orbitals

that are nearly degenerate and the LUMOs to be a degenerate set of e_g orbitals. Transitions between these orbitals gave rise to two excited states. The lowest singlet excited states have configurations, $^1(a_{2u},e_g)$ and $^1(a_{1u},e_g)$ that are nearly degenerate and have a strong electron interaction. The resulting interaction where the transition dipoles of the two configurations nearly cancel yields the relatively weak Q bands while the interaction where the transition dipoles add constructively yields the intense Soret band.[38]

While (1.10) forms the basis for mathematical interpretation of spectroscopic data, this work is more concerned with using the developed selection rules to eliminate possibilities which are forbidden as illustrated in Chapter 4. Instead, description of the electronic absorption strength is given in quantities directly related to what is measured in the laboratory. These are the absorption cross section (σ) and molar extinction coefficient or molar absorptivity (ε), which are experimentally measured quantities given in (1.11) and (1.12):

$$I_l = I_0(e^{-\sigma l N_A}) \tag{1.11}$$

$$I_l = I_0(10^{-\varepsilon l M}) \tag{1.12}$$

where I_0 is the incident light intensity before passing through the sample; I_l is the intensity after passing through the sample of path length, l (in cm); N_A is Avogadro's number and M is the concentration in moles/liter. Equation (1.12) can be re-arranged into an equation known as the Beer-Lambert's law (1.13):

$$\frac{I_0}{I_l} = 10^{\varepsilon l M}$$

$$log\ \frac{I_0}{I_l} = \varepsilon l M$$

$$A = \varepsilon l M \quad (1.13)$$

where A is the absorbance of the sample defined as $log\ \frac{I_0}{I_l}$. As seen in (1.11) and (1.22), absorbance is proportional to the number or the concentration of molecules and can be used in estimating the population of molecules in the ground state and excited state as will be shown in the supporting information for Chapter 5.

1.5.3 Excited State Decay Pathways

Following the excitation of molecules from a lower energy state to the FC excited states, the molecules eventually dissipate the excess energy, either by radiative or non-radiative pathways to return to the equilibrium ground state. These pathways are discussed in the following sub-sections and illustrated in Figure 1.5.

Internal Conversion

The molecules in FC excited states higher in energy level (e.g. S_2 or higher vibrational levels of S_1 (v > 0)) than the equilibrium excited state, convert their excess energy into vibrational or rotational energy, which can be transferred to the surrounding medium. This relaxation is a non-radiative process and is termed internal vibrational relaxation (IVR) for energy dissipation within the same electronic energy level but different vibrational level (e.g. S_1 (v = 1) to S_1 (v =0)) or internal conversion (IC) for energy dissipation from one electronic level to another (e.g. S_2 to S_1). The mechanism for both non-radiative relaxation is the same and will subsequently be referred to as internal conversion.

Fluorescence

IC occurs on very fast time scales (10^{-15} s) such that molecules accumulate in the lowest vibrational level of S_1. From here, photon emission (fluorescence) can occur. Most molecules typically emit in accordance with Kasha's rule, which states that in condensed phases, fluorescence is only observed from S_1. This is especially valid for molecules with small S_2-S_1 energy gap. For molecules with sufficiently large S_2-S_1 energy gap, as is the case with MPs, Kasha's rule can be violated. Because the energy level of the equilibrium excited state is lower than the initially absorbed photon, fluorescence is typically observed at lower energy or at longer wavelength than absorption. Moreover, because the electronic transitions are to different vibrational levels of the ground state, the shape of fluorescence spectra exhibits the same general features as the absorption spectra. In fact, for rigid molecules like MPs, the fluorescence spectra mirror the absorption spectra.

Intersystem Crossing and Phosphorescence

In NCPU-TTA, an important step is the conversion of an excited singlet into a much longer-lived excited triplet state. Intersystem crossing (ISC) is an isoenergetic, non-radiative transition, between two electronic states of different multiplicities. When a molecule absorbs a photon and goes to an excited state such as S_1, it keeps the orientation of its spin in accordance with the Pauli exclusion principle. The molecular electronic state in which electrons are paired is called a singlet state while the molecular electronic state in which the two electrons are unpaired is called a triplet state (recall orbital configuration shown in Figure 1.3). The triplet state is achieved when an electron from a singlet energy level flips and crosses into a triplet energy level (S_1 to T_1 crossing in Figure 1.5). From the T_1 energy state, a photon can be emitted (phosphorescence) but

at a much lower emission intensity and at longer time scales than singlet-singlet transitions due to spin restrictions.

Kinetics of electronic transitions

As with electronic absorption discussed in Section 1.5.2, the excited state decay pathways described above are preferably characterized in terms of quantities that can be measured in the laboratory. This section enumerates these relevant measurable quantities which are population of states, fluorescence quantum yield and lifetime and transition rate.

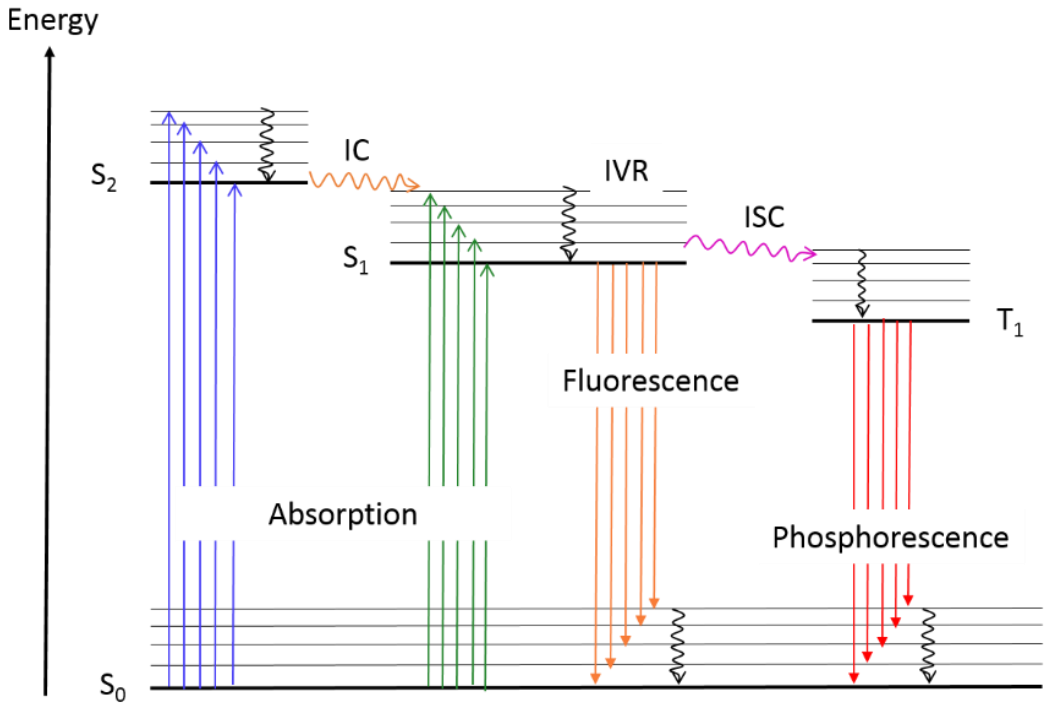

Figure 1.5 Generic photophysical processes (presented as a simplified Jablonski diagram) for MPs excited to the second excited singlet state. The photophysical processes shown are absorption, the radiative decays - fluorescence and phosphorescence and

nonradiative decays - intramolecular vibrational relaxation (IVR), internal conversion (IC) and intersystem crossing (ISC). [Adapted and modified from Condensed-Phase Molecular Spectroscopy and Photophysics by Anne Myers Kelly].[35]

When a molecule undergoes a transition from S_0 to say for instance S_1 ($S_0 \rightarrow S_1$), the Boltzmann distribution can be used to estimate the relative population of molecules in a given state at a given time using the equation:

$$\frac{N_{S_1}}{N_{S_0}} = \exp\left(-\frac{\Delta E}{k_B T}\right) \quad (1.14)$$

where N_{S1} is the population of molecules in the S_1 state, N_{S0} is the population of molecules in the S_0 state, k_B is the Boltzmann constant, T is the temperature in K and ΔE is the difference in energy between the two states. When more than one state has the same energy, Equation (1.14) is multiplied by the degeneracy factor, $f = (g_f/g_1)$, where g_f and g_i are the degeneracies of the final and initial states.

If the photophysical processes in Figure 1.5 are taken as unimolecular processes, and the depopulation of S_1 after the initial photon absorption is considered ($S_1 \rightarrow S_0$), an exponential decay is expected for the population of molecules in S_1 and an exponential rise is expected for S_0. The expression for these are given in (1.15) and (1.16), respectively, where k_F is the fluorescence rate constant).

$$N_{S_1}(t) = N_{S_1}(t=0)e^{-k_F t} \quad (1.15)$$

$$N_{S_0}(t) = N_{S_0}(t=0)(1 - e^{-k_F t}). \quad (1.16)$$

As with elementary reaction kinetics, the time at which the concentration of the S_1 state has decreased to 1/e of its original value is $t = 1/k_F$. This is called the fluorescence lifetime if the only depopulation route is fluorescence and is denoted as τ_F. If the S_1 state decays via three possible pathways – internal conversion with rate constant, k_{IC}, intersystem crossing with rate constant, k_{ISC}, and fluorescence, (1.15) becomes:

$$N_{S_1}(t) = N_{S_1}(t=0)e^{-(k_F+k_{IC}+k_{ISC})t} \qquad (1.17)$$

and its lifetime becomes, $\tau = 1/(k_F+k_{IC}+k_{ISC})$. Due to competing radiationless decay pathways, the number of photons emitted is most often less than the number of photons initially absorbed. The ratio of the photons emitted to that of the photons absorbed is defined as the quantum yield, denoted as Φ_{em}. The emission quantum yield Φ_{em} in practice, is most often calculated by the relative comparison to a standard fluorescent molecule with a well-known quantum yield. Using this relative method, the emission quantum yield of a compound can be calculated from (1.18),

$$\Phi_{em,x} = \Phi_{em,r}\,\frac{F_{em,x}}{F_{em,r}}\,\frac{\left(1-10^{-A_r(\lambda_{ex,r})}\right)}{\left(1-10^{-A_x(\lambda_{ex,x})}\right)}\,\frac{n_x^2}{n_r^2} \qquad (1.18)$$

where the subscripts x and r denote sample and reference standard, ex and em are excitation and emission wavelengths, F is the integrated spectral fluorescence (corrected), $A(\lambda_{ex})$ is the absorbance at the excitation wavelength, n is the refractive index of the medium containing the compound.

1.5.4 Resonance Energy Transfer

Energy transfer (ET) is an important aspect of DSSC and NCPU-TTA studies. Molecules in the excited state can dissipate their excess energy by transferring it to another molecule. This process can be described in terms of electronic motion between occupied (HOMO) and unoccupied (LUMO) orbitals of the donor and acceptor (sensitizer and emitter in this case). Figure 1.6 schematically show these electronic motions, where the electrons involved are represented as upward and downward arrows to depict the spin multiplicity of the ET process.[37, 39-41] ET can occur via a Coulombic interaction route referred to as Förster mechanism.[37, 40] In the Förster mechanism, oscillating electrons of an excited-state sensitizer are coupled with those of the emitter by an induced dipole interaction, resulting in formation of the sensitizer's ground state and emitter's excited state. This mechanism requires an overlap of emission spectra of S and absorption spectra of E and can work at a range between 10-100 Å. ET can also occur via an electron exchange interaction route referred to as Dexter mechanism.[37, 39] Dexter ET is the most relevant mechanism involved in *homo*-NCPU-TTA and is discussed in more detail below.

Dexter Energy Transfer

In contrast to the Förster mechanism, where S-E can interact at a longer range, Dexter ET is a short-range, non-radiative collisional or exchange energy transfer with electron exchange between sensitizer and emitter molecules. This electron exchange between S-E require not only an overlap between emission spectra of S and absorption spectra of E but also an overlap of their wavefunctions.[37] For this to be satisfied, the excited molecules of the sensitizer and the ground-state emitter should be in close proximity (<10 Å) so the exchange can happen.[37, 39] In cases where the intermolecular

distances between S-E molecules are longer than 10Å, molecular diffusion has to occur prior to electron exchange.

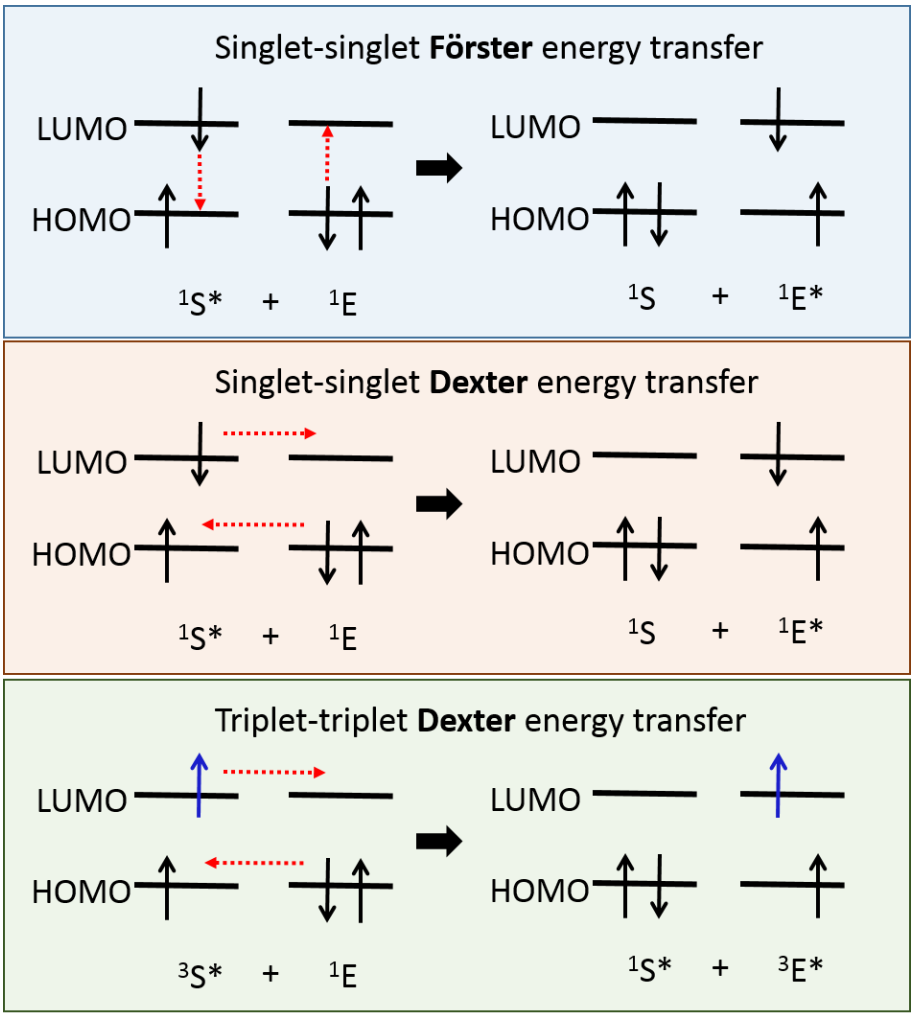

Figure 1.6. Schematic representation of energy transfer mechanisms through dipole-dipole interactions (Förster) and electron exchange (Dexter).

Dexter ET requires adherence to the spin conservation rule. In Figure 1.6, the spin-allowed processes can be a singlet-singlet energy transfer, where the singlet excited

sensitizer exchanges an electron with the ground state emitter producing the ground state sensitizer and singlet excited emitter: $^1S^* + {}^1E \rightarrow {}^1S + {}^1E^*$. It can also be a triplet-triplet energy transfer, where the triplet excited state of the sensitizer exchanges an electron with the ground state emitter producing a triplet excited emitter and ground state sensitizer: $^3S^* + {}^1E \rightarrow {}^1S + {}^3E^*$. Triplet-triplet energy transfer is forbidden by the dipole-dipole mechanism and can only occur via electron exchange mechanism. It is for this reason that control of S-E distances is crucial in NCPU-TTA studies.[37, 42]

Triplet-Triplet Annihilation

As discussed above, a triplet state of the sensitizer can excite the ground state of the emitter to its triplet state. When an emitter triplet encounters another emitter triplet, TTA can occur. In the case of ZnTPP acting as both sensitizer and emitter, this means that TTA occur between two ZnTPP triplets, forming a molecule in the S_2 state and another in the S_0 state as has been schematically shown in Figure 1.4. Upconverted fluorescence is observed when the S_2 state emits a photon to return to the ground state. Studies have shown that the upconverted fluorescence varies quadratically with the triplet state concentration at low excitation power (weak annihilation limit) and linearly with high excitation power (strong annihilation limit).[14, 43-48] The final mathematical forms of the power dependence of upconverted fluorescence are summarized in (1.19) to (1.26). Details of the kinetic derivation were described by Bachilo and Weisman[44] and will not be shown here. The upconverted fluorescence intensity, N_{NCPU}, is proportional to the square of T_1 population and is expressed as:

$$N_{NCPU} = \int_o^\infty \Phi_F k_{TTA}([T_1]_t)^2 \qquad (1.19)$$

Considering the simplified *homo*-NCPU-TTA mechanism given in (1.1)- (1.4) and ignoring for now the build-up of T_1 population from ISC, the time dependence of the concentration of MP triplet molecules can be described as:

$$\frac{d[T_1]_t}{dt} = -k_d[T_1]_0 - k_{TTA}([T_1]_0)^2 \quad (1.20)$$

where k_d is the sum of rate constants of the intrinsic phosphorescent and other unimolecular first order or pseudo-first order decay pathways of the triplet state and k_{TTA} is the rate constant of the TTA process. The analytical solution to (1.19) from Bachilo and Weisman[44] is given as:

$$[T_1]_t = [T_1]_0 \frac{1-\beta}{e^{k_d t}-\beta} \quad (1.21)$$

$$\beta = \frac{\alpha}{k_d+\alpha} = \frac{k_{TTA}[T_1]_0}{k_d+k_{TTA}[T_1]_0}; \alpha = k_{TTA}[T_1]_0 \quad (1.22)$$

In the weak annihilation kinetic regime, the majority of emitter triplets are decaying by some first or pseudo-first order relaxation pathway ($k_d >> k_{TTA}[T_1]_0$), thus pooling of molecules in the triplet state is low. The expression in 1.21 reduces to:

$$[T_1]_t = [T_1]_0 e^{-k_d t} \quad (1.23)$$

Substituting (1.23) into (1.19) and integrating gives:

$$N_{NCPU} = \frac{\Phi_F k_{TTA}}{2k_d}[T_1]_0^2 \quad (1.24)$$

Expression (1.24) shows that when TTA becomes rate limiting, NCPU-TTA requires the diffusional annihilation of two triplets or the annihilation of two triplets in short distance from each other. The power dependence plot for this case displays quadratic behavior.

In the strong annihilation limit, the triplet concentration is high, (k_{TTA} $[T_1]_0$ >> k_d). Taking this condition to simplify (1.21) then substituting the result into (1.19) before integrating yields:

$$[T_1]_t = \frac{1}{1+k_{TTA}t[T_1]_0} \quad (1.25)$$

$$N_{NCPU} = \Phi_F k_{TTA}([T_1]_0)^2 \frac{1}{k_{TTA}[T_1]_0} = \Phi_F[T_1]_0 \quad (1.26)$$

Thus, in the strong annihilation regime, TTA can occur with the absorption of a single additional photon, thus giving a linear power dependence plot.[44]

The general mechanism of *homo*-NCPU-TTA presented in Figure 1.4 shows formation of S_2 from TTA. However, the singlet state is not the only possible product of a triplet-triplet encounter. The probability that TTA yields an excited singlet molecule is equal to the factor of 1/9 as determined by spin statistics.[44] The other possibilities in addition to the formation of a higher singlet state are shown in (1.27) - (1.29). In these equations, MP states are denoted ^{n}(MP) where an asterisk superscript denotes an excited state.

$^3(MP)^* + {}^3(MP)^* \rightarrow {}^5(MP\text{-}MP)^* \rightarrow {}^5(MP)^* + {}^1(MP)$ (5/9) (1.27)

$^3(MP)^* + {}^3(MP)^* \rightarrow {}^3(MP\text{-}MP)^* \rightarrow {}^3(MP)^* + {}^1(MP)$ (3/9) (1.28)

$^3(MP)^* + {}^3(MP)^* \rightarrow {}^1(MP\text{-}MP)^* \rightarrow {}^1(MP)^* + {}^1(MP)$ (1/9) (1.29)

According to the spin statistical factor in (1.29), the yield for up-conversion from TTA is a maximum of only 11% if Φ_F from the MP S_2 state is 100%. Fortunately, the triplet and quintet excimers can return back to the triplet excited state thereby improving the TTA efficiency. This recycling of the triplet and quintet excimers back to T_1 has been shown to improve heteromolecular NCPU-TTA efficiency to *ca.* 40%.[49]

Fluorescence/Phosphorescence Quenching

TTET in heteromolecular NCPU-TTA systems can be described as quenching, a physical process that decreases the molecular fluorescence/phosphorescence of the sensitizer molecule. Thus, TTET efficiency is often measured using Stern-Volmer quenching experiments with the emitter as the quencher. The Stern-Volmer equation is given below (1.30):

$$\frac{\int I_0}{\int I} = 1 + K_{SV}[Q] = 1 + k_Q \tau_0 [Q] \qquad (1.30)$$

where $\int I_0$ and $\int I$ are the integrated fluorescence intensity of the sensitizer in the absence and presence of quencher, respectively; k_Q is the quenching rate constant (here $k_Q = k_{TTET}$) and τ_0 is triplet excited state lifetime of the sensitizer in the absence of the quencher and [Q] is the molar concentration of the quencher.

In *homo*-NCPU-TTA, quenching is not a necessary step and is in fact, an undesirable process when it occurs as it lowers the efficiency of NCPU-TTA. In this case, the quencher is another molecule present in the DSSC heterojunction such as the iodide in the electrolyte system.

1.5.5 Spectroscopic Signatures of MP H- and J-Aggregates

MPs can aggregate in solution even at low concentrations due to strong π-π interactions.[50] Two well-studied superstructures formed from π-π stacking of molecules are commonly referred to as J- and H-aggregates. In J-aggregates, the monomers are displaced with respect to each other in a “head to tail” type arrangement in which the stacking direction is roughly parallel to the molecular plane (Figure 1.7A). Meanwhile, H-

aggregates have the monomers stacked on top of each other in a “face-to-face” arrangement in which the stacking direction is roughly perpendicular to the molecular plane (Figure 1.7B).

Figure 1.7. Typical arrangements of H- and J-aggregates for a π-conjugated molecule (monomer).

A notable property of MP aggregates is that the absorption and fluorescent spectra of the aggregated molecules differ from the spectra of aggregated MPs while the electronic structure is not drastically modified. A number of articles have reported spectral signatures of MP J- and H-aggregates and details of their exciton dynamics will not be presented in this introduction. Please refer to references 51-56 for detailed discussions on this subject.[51-56] For this introduction, only a description of the position of the absorption and emission peaks of aggregated MP relative to the monomer will be presented. H- and J-aggregates are most conveniently distinguished on the basis of their electronic spectra. Considering the electronic π–π* transitions of the monomer, H-aggregates are characterized by a hypsochromic (blue-shifted) and J-aggregates by a bathochromic (red-shifted) absorption with respect to the monomer UV-vis absorption band.[51-56]

1.6 Motivation of and Overview of Thesis

The benefit of incorporating MP systems exhibiting NCPU-TTA into real devices such as the silicon solar cells or DSSCs depends on the efficiency of the up-conversion. This work aims to understand the different factors that affect the efficiency of NCPU-TTA when up-converting MPs are incorporated as additional component within a TiO_2-dye heterojunction in DSSCs. As seen in Figure 1.1, DSSCs are complex systems, thus, this work limits its contribution to only a few processes.

Recall in Figure 1.1 that following the absorption of low energy photons, the sensitizer must undergo intersystem crossing from the singlet state (S_1) to the triplet state (T_1). This ISC is an important step in NCPU-TTA as its efficiency is dependent on the T_1 population. However, before ISC can happen, the S_1 state can transfer its energy to the electrolyte used in the DSSC. A common electrolyte in DSSCs is the iodide/triiodide redox pair, and iodide ion is known to be a very efficient fluorescence quencher. When the energy or the electron from the MP S_1 state is lost by quenching, the efficiencies of both traditional and NCPU-TTA enhanced DSSCs are adversely affected. When the S_2 state is quenched by the electrolyte, then adding an up-converting MP system will not improve conversion efficiency. Thus, the first approach used in this work to understand the conditions needed to incorporate up-converting MPs into DSSCs is to investigate the effect of commonly used iodide/triiodide redox couple on the spectroscopic properties of a derivative of ZnTPP. Results of this study are discussed in Chapter 3.

Another important event in the operation of DSSCs is the injection of an electron from an excited state of the sensitizer to the conduction band of the photoanode. In the case of traditional DSSC, this is from the S_1 state, while in NCPU-TTA enhanced DSSC,

this is from the S_2 state. It is desirable that the energy from the S_2 state is used to inject electrons to the conduction band of the semiconductor rather than lose its energy by emitting radiation or by vibrational relaxation. This is addressed in Chapter 4 which looks at tuning the band gap of the commonly used titania (TiO_2) photoanode such that the conduction band falls in between the S_2 and S_1 energy level of MP. The approach used in Chapter 4 is to dope the TiO_2 with ZrO_2. Titania's band gap lies below the S_2 energy level of ZnTPP complicating the analysis of NCPU-TTA occurrence.[11] Zirconia's band gap, on the other hand, lies above it.[11, 47, 57] Given this information, when ZnTPP is adsorbed on zirconia (used as proxy for the TiO_2 photoanode) and is excited in the Q-band region, observation of ZnTPP S_2 emission is an indication of NCPU-TTA.

It is also known that *homo*-NCPU-TTA requires the sensitizer and emitter to be in close proximity to each other, especially in solid state devices where collisional encounters of two triplet states are limited or absent. To exploit the potential of *homo*-NCPU-TTA in solid state devices, a means of controlling their molecular aggregation and spatial orientation on semiconductor surfaces is of utmost importance.[55, 58, 59] This is addressed in Chapter 5 which explores using Langmuir Blodgett (LB) deposition to control the assembly of MPs on solid substrates. The LB method of film preparation typically starts with spreading a monolayer of amphiphilic molecules with long alkyl chains at the air-liquid interface. Controlled compression of the monolayer at the liquid surface results in the formation of assembled domains with controllable molecular distances and orientations which can then be deposited onto solid substrates to produce LB films.

In addition to controlling the intermolecular distances between MP molecules in *homo*-NCPU-TTA, controlling the specific orientation of MPs with respect to each other is

also important. Several studies in the literature have reported orientation effects on singlet energy transfer in porphyrinic artificial light harvesting systems.[60-62] Orientation effects on triplet-triplet energy transfer (TTET) and particularly on TTA are less well-explored.[62] It is however recognized that TT coupling depends on the degree of orbital overlap between S-E and is highly sensitive to molecular shape, size and orientation.[41] To precisely control the orientation of MPs, the use of metal organic frameworks (MOFs) are explored in Chapter 6. MOFs are crystalline compounds formed through extension of repeating coordination entities (metal ions and organic ligands such as MPs) in two or three dimensions. The repeating coordination units in MOFs forms structures with well-defined intermolecular distance and spatial orientation. This makes them the ideal matrices for studying orientation effects on *homo*-NCPU-TTA efficiency.

In Chapter 7, the results of the above-mentioned investigations are discussed as a whole and in the context of existing knowledge. Gaps in that knowledge as well as the problems encountered are identified. Recommendations on future work to resolve these problems, in order to further advance the fundamental understanding on implementation of MPs as NCPU sensitizers in DSSCs, are given.

CHAPTER 2. EXPERIMENTAL TECHNIQUES

This chapter briefly describes the most common spectroscopic measurements as well as a key technique – removal of oxygen – employed in studying NCPU-TTA processes. These spectroscopic techniques include steady state absorption and emission, transient absorption, time-resolved emission behavior, and photon up-conversion by triplet-triplet annihilation. Techniques that are specific to a particular study are described in detail in the Experimental Section of said study and will only be enumerated in this section. Techniques specifically used in Chapter 4 are powder X-ray diffraction and transmission electron microscopy to characterize the respective crystallinity and size of the prepared metal oxide powders; diffuse reflectance to calculate using Tauc plot the band gap of metal oxides on glass supports as well as determine the absorbance of MPs adsorbed on the metal oxides; profilometry to determine the thickness of films. Techniques used in Chapter 5 include: nuclear magnetic resonance (NMR) and mass spectroscopy (MS) to verify the formation of surface active porphyrin; Langmuir to prepare and characterize monolayers of MPs at the water surface; Langmuir-Blodgett (LB) to transfer monolayers from the water subphase onto quartz substrates; Brewster angle microscopy (BAM) to visualize Langmuir monolayers upon compression; AFM to measure the thickness of the monolayer/multilayer LB films. Chapter 6 also used powder XRD to characterize the metal-metalloporphyrin frameworks (MMPF), thus, powder XRD instrument details will not be included in Chapter 6.

2.1 Removal of Oxygen

Because of the importance of the triplet state, which is sensitive to quenching by molecular oxygen, an important technique in the study of NCPU-TTA is the removal of

oxygen from liquid and solid samples. For liquid samples, custom-made 1 cm x 1 cm quartz cuvettes with provisions for attachment of a sample bulb and connection to a high vacuum line was used to facilitate degassing of samples using the freeze-pump-thaw method. For solid-state NCPU-TTA studies, a sample holder designed in the the laboratory of R.P. Steer was used. This sample holder consists of a brass triangular cell equipped with piping that can be connected to a high vacuum line. Solid samples on glass or quartz supports were mounted sample side onto the vacuum chamber as shown in Figure 2.1. This design was able to maintain pressure below 5 mTorr which was sufficient to minimize triplet state quenching by oxygen.

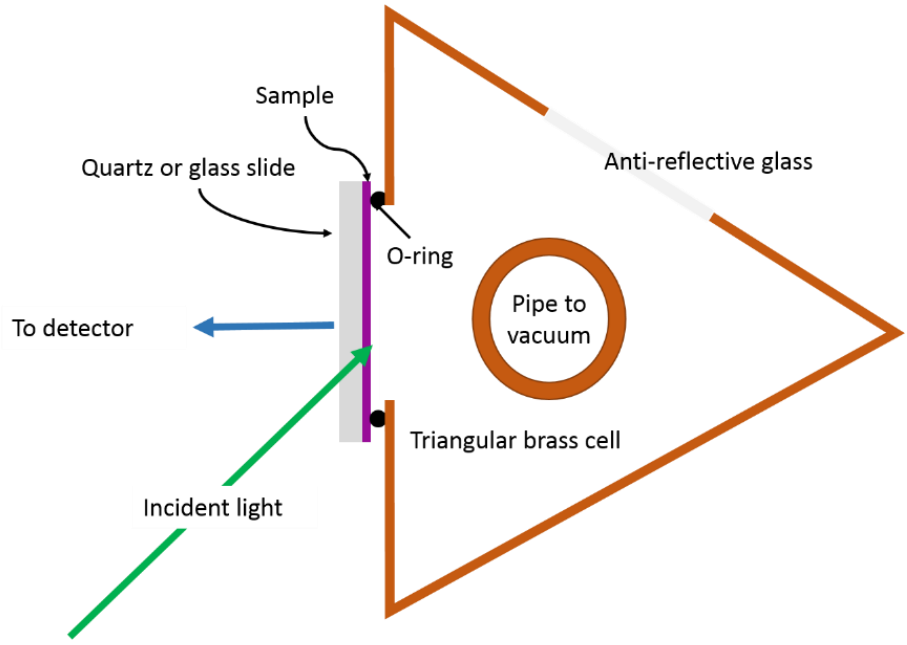

Figure 2.1: Cartoon depiction of excitation of a thin film sample mounted on the custom designed solid state sample holder (view is from the top).

2.2 Steady State Absorption

The steady absorption spectrum of a sample can be measured by UV-Vis absorption spectroscopy. In this technique, the intensity I of light of varying wavelengths, after passing through the absorbing medium, is compared to the intensity I_0 of the same light before entering the medium. The ratio I/I_0 is the transmittance T of the medium, and the absorbance A can be calculated using Beer-Lambert's law, which was given in Equation 1.23.

$$A = -\log(T) = \varepsilon l M$$

The absorption spectra of the various samples in this study were recorded with a Varian Cary 6000i UV-Vis spectrometer.

2.3 Steady State Emission

While absorption measurements described above are relative since the light intensity before the sample is compared to the light intensity after the sample, emission measurements are absolute measurements. Therefore, the wavelength dependence of the efficiency of the spectrofluorometer used to measure an emission spectrum needs to be known and corrected.

The steady state fluorescence measurements were carried out using a PTI Quantamaster spectrofluorometer. The instrument is equipped with software that corrects for the wavelength dependent efficiency of the emission monochromator and the sensitivity of the detector used for detection of emitted photons. Also, the correction software takes into account the detected emission signal by the excitation lamp intensity in the sample chamber (*i.e.* the wavelength dependent efficiency of the excitation

monochromator and excitation light source output, as well as time dependent fluctuations in the excitation light intensity). Correction factors not included in the software such as reabsorption and inner filter effects were manually done following the procedure described by Karolczak *et al.* [63]

2.4 Emission Lifetimes

Emission decay kinetics of MPs involved in NCPU-TTA can be studied using time-correlated single photon counting (TCSPC).[64] In this technique, the output of a mode-locked femtosecond Ti-sapphire laser (Coherent, Mira 900D) pumped by a continuous wave diode laser (Coherent Verdi V10) was passed through an acousto-optic modulator to obtain a 4.5 MHz excitation repetition rate. The output beam was frequency doubled by an LBO crystal and the plane-polarized second harmonic output was focused onto a quartz cuvette containing the sample. The fluorescence signal was measured at the magic angle by a cooled photomultiplier tube (MCP-PMT R3809-50U) coupled to a prism monochromator (Carl Zeiss M4QIIID). The instrument response function was measured using scattered excitation light from a colloidal silica (LUDOX) solution. The data was acquired using an SPC-830 acquisition board (Becker and Hickl). Fluorescence decay parameters were obtained using a non-linear least squares iterative convolution process based on the Marquardt algorithm. The goodness-of-fit was evaluated using reduced chi-squared values and the distribution of weighted residuals.

2.5 Transient absorption

Transient absorption (TA) spectra and kinetic traces can be collected by using a pulsed xenon arc lamp to record the sample absorbance before and at different time-delays after the laser pulse excitation. This technique can be used to study the kinetics

of non-emissive triplet states in NCPU-TTA. It can also be used to reveal if laser-induced photochemical reactions are occurring, which can be seen as a delay of the ground state recovery of a chemical species with respect to the decay of its excited state absorption.

Triplet transient absorption and triplet decay laser flash photolysis experiments were performed using Edinburgh Instruments LP920 spectrometer. In brief, a xenon flash-lamp (pulse width ~ 0.5 to 10 ms with 10 Hz repetition rate) was used as probe light, while a Q-switched Tempest 300 Nd:YAG laser (pulse width ~ 3−5 ns pulses) operating at a frequency of 10 Hz was used as the excitation source. The second harmonic of the Nd:YAG laser (532 nm) was used to excite the samples. The absorption spectrum and the time-dependent absorption kinetics of the transients formed upon excitation with the laser pulse were probed using xenon arc lamp (Xe920). The excitation beam and the probe beam cross each other at 90° in a 10 mm × 10 mm quartz cuvette containing the sample. The transmitted light is then focused onto a Czerny−Turner grating monochromator (TMS300) and finally detected using an LP900 photomultiplier. The time resolution of the instrument is ∼7 ns. Data acquisition was facilitated using L900 software supplied by Edinburgh Instruments.

2.6 Photon Up-conversion by Triplet-Triplet Annihilation

NCPU-TTA was monitored using a modified Jobin-Yvon Spex Fluorolog spectrofluorometer equipped with a double grating monochromator and a cooled single-photon-counting detector on the emission side. The emission measurements were made in the front face geometry with the excitation beam intercepting the sample at ∼32°, which is less than the critical angle of incidence. Residual excitation light was removed by adding an NF533-17 (Thorlabs) notch filter before the emission monochromator.[17] MPs

adsorbed on metal oxides or assembled as Langmuir-Blodgett films on quartz substrates were mounted as the front window on a triangular brass cell, with the sample facing the inner, evacuable side of the cell (recall Figure 2.1) when connected to a grease-free high-vacuum line. These thin film samples were degassed under vacuum for at least 1 h, down to a pressure < 5 milliTorr, prior to measurements.

Polarized excitation was performed by inserting a half-wave plate in between a 532 nm diode laser and the sample and collecting emission spectra with the half-wave plate angle set at 0° and 90°.

CHAPTER 3. PHOTOPHYSICS AND HALIDE QUENCHING OF A CATIONIC METALLOPORPHYRIN IN WATER

As established in Chapter 1, the overall goal of this thesis is to understand the different factors that affect the efficiency of NCPU-TTA when up-converting MPs are incorporated as additional component within a TiO_2-dye heterojunction in DSSCs. There are three major photophysical processes-related components of a conventional DSSC device – dye sensitizer, redox shuttle and photoanode. This chapter looked into the relationship between the dye sensitizer and redox shuttle.

The commonly used iodide/triiodide DSSC redox couple is a known fluorescence quencher. Quenching of the MP S_1 and S_2 state adversely affects the efficiencies of both traditional and NCPU-TTA enhanced DSSCs. Thus, in this work, the effect of iodide on the spectroscopic properties of a ZnTPP derivative was investigated.

This chapter is reprinted with minor revisions from a paper published in *Photochemical & Photobiological Sciences* **2013,** 12, (6), 1079-1085 (Reproduced from Ref. 61 with permission from The Royal Society of Chemistry).[65]

For this contribution, the author carried out majority of the experimental work except for additional trials on TCSPC data collection, which was performed by Dr. Neeraj K. Giri. The author was mainly responsible for the data analysis and preparation of the manuscript. Dr. Matthew Paige and Dr. Ron Steer provided extensive guidance in planning the experimental work and interpreting results. Both senior authors edited the manuscript prior to publication.

PHOTOPHYSICS AND HALIDE QUENCHING OF A CATIONIC METALLOPORPHYRIN IN WATER

Concepcion P. Ponce, Ronald P. Steer* and Matthew F. Paige*

Department of Chemistry, University of Saskatchewan, 110 Science Place, Saskatoon, Saskatchewan, Canada

3.1 Abstract

In this work, the steady state S_0–S_1 and S_0–S_2 absorption and emission behaviour of the water-soluble tetrakis(N-methyl-4-pyridyl)porphyrin zinc(II) tetrachloride (ZnTMPyP) in media of constant and high ionic strength, both with and without iodide ions as a fluorescence quencher, was measured. The quenching of the ZnTMPyP S_1 state by iodide ions proceeds primarily through diffusion-limited interaction in an encounter pair but the formation of a loose association between the ZnTMPyP S_1 state and iodide ions also provides a minor quenching pathway. The ZnTMPyP S_2 state was quenched minimally by iodide,

likely through an electron transfer mechanism at an average donor–acceptor distance of ~0.7 nm. The results presented here highlight the notion that significant iodide quenching of the ZnTMPyP S_1 state can be a source of inefficiencies in porphyrin-based dye-sensitized solar cells. The minimal quenching of the S_2 state indicates that no significant loss of efficiency will be introduced by using iodide as

component of the electrolyte system in up-conversion by triplet–triplet annihilation (UC-TTA) enhanced solar cells.

3.2 Introduction

Metalloporphyrins have been of significant interest as dye sensitizers in semiconductor-based dye sensitized solar cells (DSSCs) since the technology was introduced by Grätzel and his group in the early 1990s.[6] The structure and spectroscopic properties of MPs are similar to those of natural photosynthetic systems[66], a similarity which generated initial interest in this class of molecules as potential sensitizers. However, most DSSCs sensitized with MPs produce solar energy-to-electricity conversion efficiencies (η) which are significantly lower than those achieved by "champion" ruthenium black dyes.[66-68] This has been attributed to poor overlap of the absorption spectra of MPs with the solar spectrum[69] as well as their propensity to form random aggregates on semiconductor surfaces.[70] While these shortcomings have limited MPs' successful application to DSSCs, recent progress in developing photon-up-conversion schemes has the potential to change this. An emerging approach to improve DSSC performance is to harness solar energy more efficiently by up-conversion (UC) of its abundant but under-utilized near infrared photons to higher energy.[15, 71, 72] This has been shown to take place in MP systems by the photophysical process of triplet-triplet annihilation (TTA) with good efficiency, both in solution and in the solid state.[14, 57]

Before MPs can be effectively utilized in solar energy conversion and storage systems especially as a component of UC-TTA enhanced DSSCs, the various photophysical interactions between their excited states and with potential electron acceptors that are present in DSSCs must be understood. In photosensitized reactions, one of the most important processes is excited state quenching. The quenching of excited states of a sensitizer dye in a DSSC typically occurs by either: 1) electron injection to the

conduction band of the semiconductor; or 2), through encounter with a quencher molecule such as iodide, a component of the widely-used I^- / I_3^- redox electrolyte system.

In this chapter, we explore the photophysical properties of the water soluble tetrakis(N-methyl-4-pyridyl)porphyrin zinc (II) tetrachloride (ZnTMPyP) (structure shown in Scheme 1), when excited in its Soret band in media of high ionic strength with and without iodide as an electron transfer agent. Our interest in this specific system is motivated by ZnTMPyP's desirable properties for UC-TTA processes. These properties include: 1) strong absorbance in the visible region of the solar spectrum to allow low energy excitation; 2) efficient intersystem crossing from the singlet state (S_1) to the triplet state (T_1); 3) a long-lived triplet state to enable diffusional quenching processes; and 4) a large singlet and triplet state energy gap to prevent back intersystem crossing to the singlet state (see review by Singh-Rachford and Castellano, 2010).[14] We have compared our results with previous studies on a similar water soluble sulfonated porphyrin, having a charge of the opposite sign and quantify the effect of charges on the diffusion-controlled bimolecular quenching rate constant.[73]

3.3 Experimental

3.3.1 Materials

Tetrakis(N-methyl-4-pyridyl)porphyrin zinc (II) tetrachloride (ZnTMPyP, Frontier Scientific Porphyrin Products), salts (sodium chloride, sodium iodide, sodium thiosulfate; Sigma-Aldrich), and spectrophotometric grade ethylene glycol (≥ 99% purity; Sigma-Aldrich) were used as received.

3.3.2 Preparation of Samples

Stock solutions of ZnTMPyP, NaCl and NaI were prepared in ultrapure water (Millipore; resistivity 18.2 MΩ) and in ethylene glycol. The reducing agent, $Na_2S_2O_3$, was added to the sodium iodide solutions to prevent the formation of I_3^-. The solutions were then mixed and diluted to make a working solution composed of 5μM ZnTMPyP in various concentrations (0 to 1.0 M) of NaI as quencher at a constant total ionic strength of 1.0 M made by adding the appropriate amount of NaCl. The emission spectra of degassed solutions of ZnTMPyP showed negligible differences compared with those of aerated solutions, suggesting that oxygen quenching of both the S_1 and S_2 electronic states of ZnTMPyP is insignificant. All measurements were then carried out using aerated solutions.

3.3.3 Spectroscopic Characterization

Steady state absorption and emission spectra as well as the lifetimes of the samples were collected using the instrumentation described in Chapter 2.

3.4 Results and Discussion

The baseline-corrected UV-Vis absorption spectra of 1.0 x 10^{-7} to 1.0 x 10^{-5} M ZnTMPyP in 1.0 M NaI (shown in Figure 3.1) followed Beer's law behaviour at 438 nm. The typical absorption spectra of MPs was observed with the intense feature at around 438 nm assigned to the B(0,0) or Soret band and the weaker features at 564 nm and 605.5 nm assigned to the Q(1,0) and Q(0,0) bands, respectively. The molar absorptivity of ZnTMPyP in aqueous iodide solutions was determined to be 1.61 x 10^5 $M^{-1}{\cdot}cm^{-1}$, which is ~25% smaller than the molar absorptivity (2.21 x 10^5 $M^{-1}{\cdot}cm^{-1}$) measured in ultrapure

water alone (Figure 3.1, inset). This decrease in molar absorptivity was not accompanied by a significant change in the overall shape of the spectra nor was it accompanied by significant changes in peak positions.

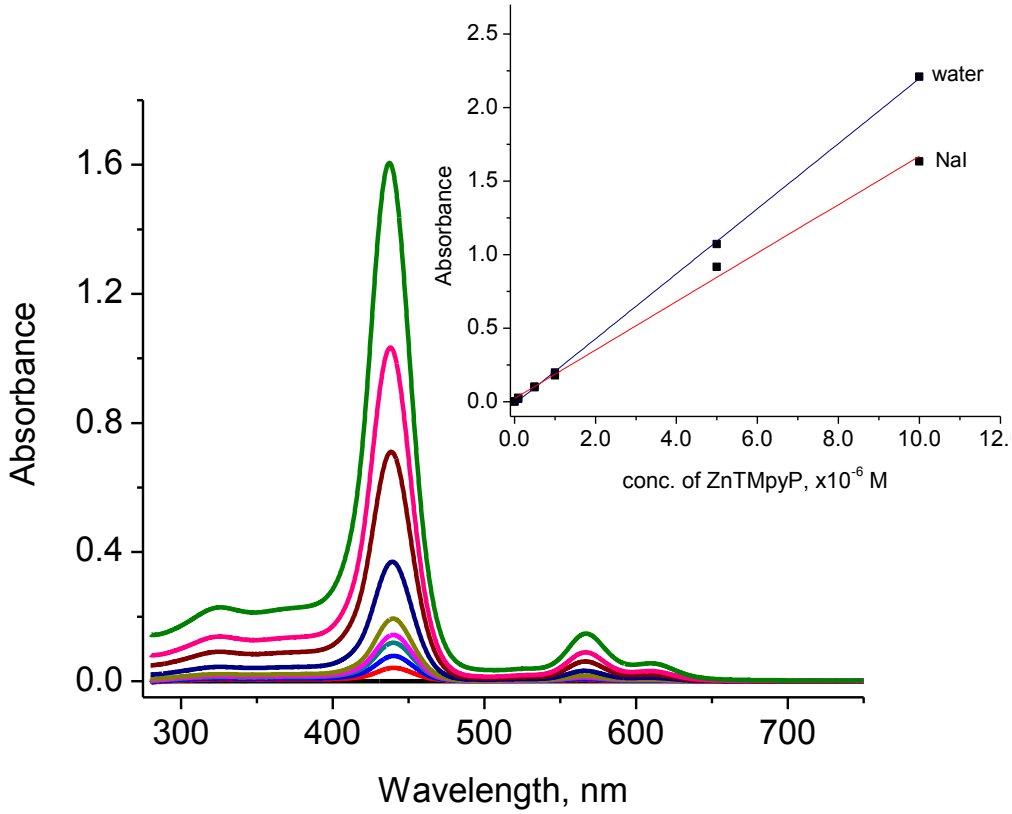

Figure 3.1 Absorption spectra of 1.0×10^{-7} M to 1.0×10^{-5} M ZnTMPyP solutions in the presence of 1.0 M NaI. Inset: Beer's law plot of ZnTMPyP in water (circles) and in aqueous 1.0 M NaI solution (squares) measured at 437 nm and 438 nm, respectively. The molar absorptivity of ZnTMPyP in ultrapure water is 2.21×10^5 M^{-1} cm^{-1} and is decreased to 1.61×10^5 M^{-1} cm^{-1} in 1.0 M aqueous NaI.

In water, a 5.0 μM ZnTMPyP solution showed a maximum absorption at 437 nm with a full width at half maximum (FWHM) equal to 28 nm (Figure 3.2, black). Changing

the media from ultrapure water to 1.0 M NaCl introduced a slight decrease in the absorption intensity as well as a Soret band shift of ~1 nm to the red but resulted in no significant band broadening (Figure 3.2, blue). Changing the media from ultrapure water to 1.0 M NaI introduced a 1.5-nm Soret band shift and a 2.5-nm Q band shift to the red (Figure 3.2, red). A bathochromic shift in the absorption spectrum is usually attributed to formation of porphyrin J-aggregates[56], however, the shift that we observed with our system was too small to be due to J-aggregate formation. The previously reported shift in absorption peaks for a water soluble porphyrin that forms J-aggregates is about 60 nm.[51, 54, 74] The observed shift of the Soret band of ZnTMPyP in 1.0 M NaI was accompanied by a decrease in peak height and an increase in FWHM by about 3.5 nm. However, the integrated absorption of 5.0 μM ZnTMPyP did not vary significantly in all three media. Despite a slight band broadening and a decrease in absorption intensity of ZnTMPyP in media of high ionic strength, the spectra did not show conclusive evidence of nonspecific aggregate formation over the ZnTMPyP concentration range used. Nonspecific aggregate formation often results in a considerable broadening of the absorption bands with no characteristic spectral features. The small shift of the Soret and Q band positions in aqueous NaI compared with aqueous NaCl is due to the replacement of Cl^- with I^- in the $[ZnTMPyP^{4+}]\cdot 4X^-$ ion pair (X^- is the halide ion). A similar effect was reported by Serra *et al.* [75] when hydrogens in the para-positions of the hydroxyphenyl groups of 5,10,15,20-tetrakis(3-hydroxyphenyl)porphyrin were substituted by halogens. In these cases, bromination or iodination of the original porphyrin resulted in a 1-3 nm shift in Soret peak position.

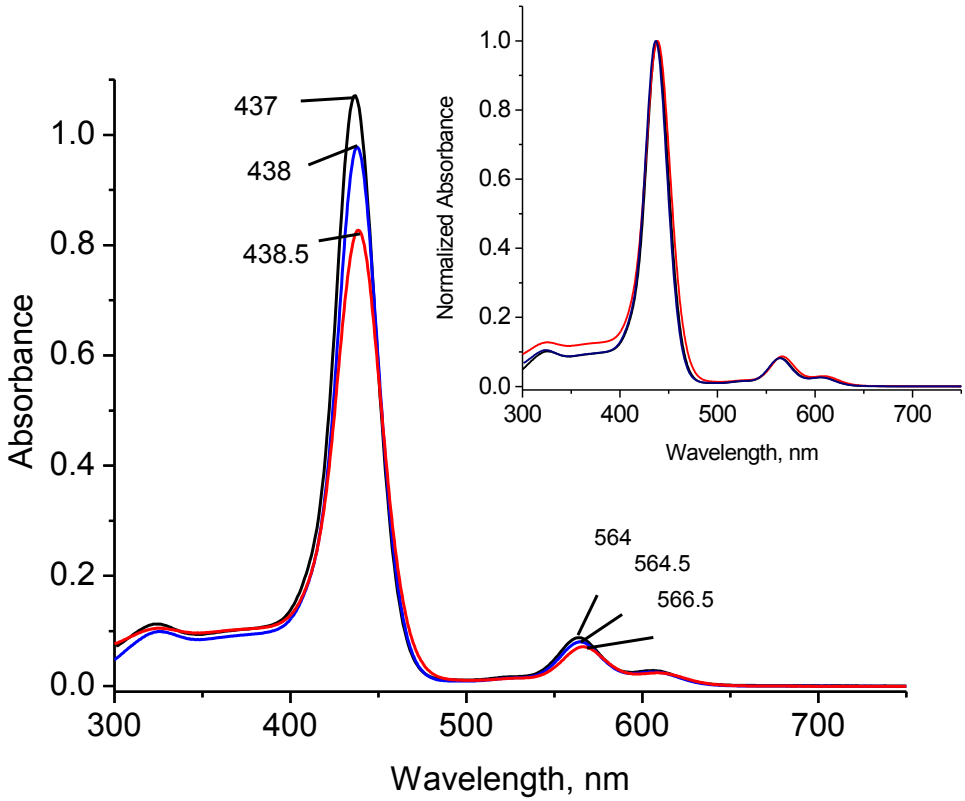

Figure 3.2. Absorption spectra of 5×10^{-6} M ZnTMPyP in ultrapure water (black); 1.0 M NaCl (blue); 1.0 M NaI (red). Inset is the normalized spectra showing the slight broadening of the 5×10^{-6} M ZnTMPyP in 1.0 M NaI (red) relative to that in ultrapure water (black).

We also followed the changes in the absorption spectra of ZnTMPyP as the concentration of NaI was increased at constant ionic strength and observed (Figure 3.3) a small but steady decrease in molar absorptivity. No significant changes were observed when the absorption spectra of the ZnTMPyP solution in 1.0 M NaI were collected at least 40 times using a sealed cuvette for a period of more than two hours (see Figure A3.1 in the Appendix). This indicates that non-specific aggregate formation is not extensive at the ZnTMPyP concentration used and on the time scale of the data collection (30 minutes to one hour). However, at higher concentrations of ZnTMPyP in a constant 1.0 M

concentration of NaI, some degree of aggregation occurred. As shown in Figure A3.2 in the Appendix, the plot of concentration of ZnTMPyP in 1.0 M NaI versus Absorbance starts to deviate from linearity at ZnTMPyP concentrations greater than 7.0 x 10^{-6} M.

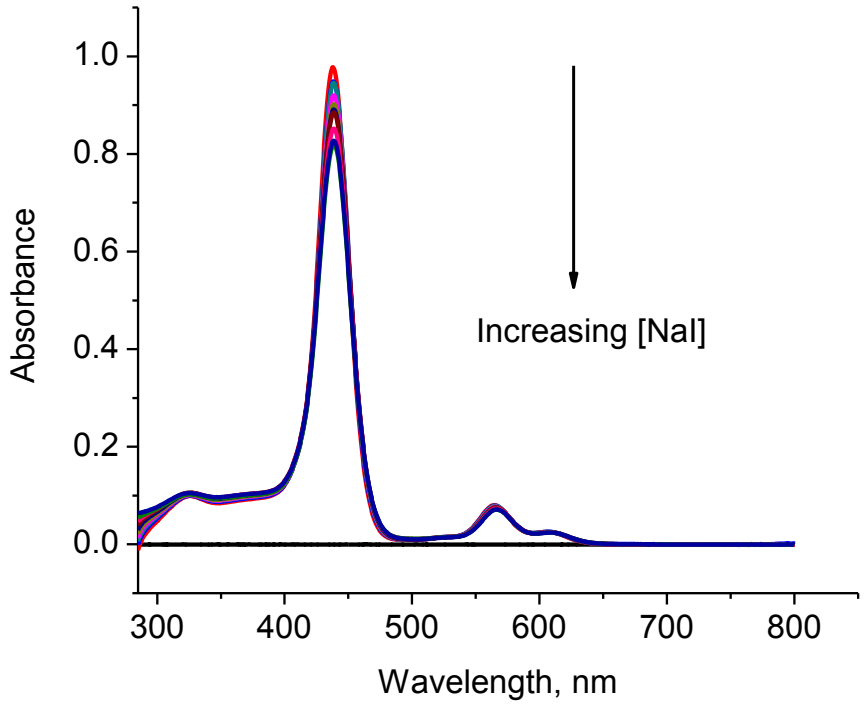

Figure 3.3. Absorption spectra of 5 × 10−6 M ZnTMPyP in the presence of NaI in concentrations ranging from 0 to 1.0 M in a constant total ionic strength of 1.0 M.

We investigated the effect of iodide concentration on the steady state S_1 fluorescence emission intensity of 5.0 × 10^{-6} M ZnTMPyP (Figure 3.4). The uncorrected steady state emission spectra of ZnTMPyP in water showed broad emission peaks at around 627 nm and 661 (data not shown) in agreement with literature values.[76] These peaks were shifted to 633 nm and 677 nm, respectively, when corrections to the steady state emission spectra described by Karolczak *et al.*[77] were applied. The corrections were

made to eliminate effects due to (1) Raman scattering as well as absorption of the solvent at the excitation wavelength; (2) variation of the detector response with respect to emission wavelength and; (3) reabsorption of emitted light by the porphyrin. The positions of the peak did not change significantly in the 1.0 M ionic strength media we used for this study. It can also be seen in Figure 3.4 that adding iodide to ZnTMPyP solutions at constant ionic strength resulted in a substantial quenching of the steady state S_1 fluorescence. Fluorescence quenching is traditionally described by two mechanisms: (1) a static mechanism when the quencher molecule/ion forms a complex with the fluorophore or when it is located within the quenching sphere of the excited species; and (2) a dynamic quenching mechanism when both reactants diffuse freely and collide. The two mechanisms can be differentiated by examining the relevant fluorescence lifetimes. Dynamic quenching is characterized by decreasing lifetimes as quencher concentration is increased while static quenching is characterized by a lifetime that is independent of quencher concentration. A Stern–Volmer (SV) plot for the quenching of the S_1 state of ZnTMPyP by aqueous iodide, obtained from the corrected emission spectra in Figure 3.4, integrated from 550–750 nm is shown in the inset of Figure 3.4. The plot is linear up to a concentration of 0.5 M NaI but starts to deviate from linearity at higher NaI concentrations. This could be attributed to some degree of ground state aggregation that was seen in the UV-Vis absorption spectra (Figure A3.1 and A3.2 in the Appendix). The linear portion of the SV plot yielded a K_{SV} value of 11.7 ± 0.1 M^{-1}. This value is consistent with the observed K_{SV} for the quenching of ZnTMPyP fluorescence by the dication methyl viologen[78] but is four times higher than the K_{SV} measured for another water soluble porphyrin (ZnTPPS), which carries a negative charge as opposed to the positive charge

of ZnTMPyP.[73] This difference is to be expected as the interaction of iodide with ZnTMPyP is attractive but repulsive with ZnTPPS. This same trend was observed in the repulsive interaction between ZnTMPyP and methyl viologen and in the attractive interaction between ZnTPPS and methyl viologen.[78] From the slope of the equation the SV plot of Figure 3.4, the dynamic collisional quenching rate constant for the quenching of ZnTMPyP S_1 state by iodide at 1.0 M ionic strength was calculated as 9.9×10^9 M^{-1} s^{-1} using:

$$\frac{\int I_0}{\int I} = 1 + K_{SV}[Q] \quad (3.1)$$

$$K_{SV} = k_Q \tau_0 \quad (3.2)$$

$\int I_0$ and $\int I$ in (3.1) are the integrated fluorescence intensity of the dye in the absence and presence of quencher, respectively; K_{SV} is the Stern–Volmer constant; k_Q is the quenching rate constant and τ_0 is the fluorescence lifetime of ZnTMPyP in the absence of quencher (1.18 ns measured using TCSPC); and [Q] is the molar concentration of the quencher.

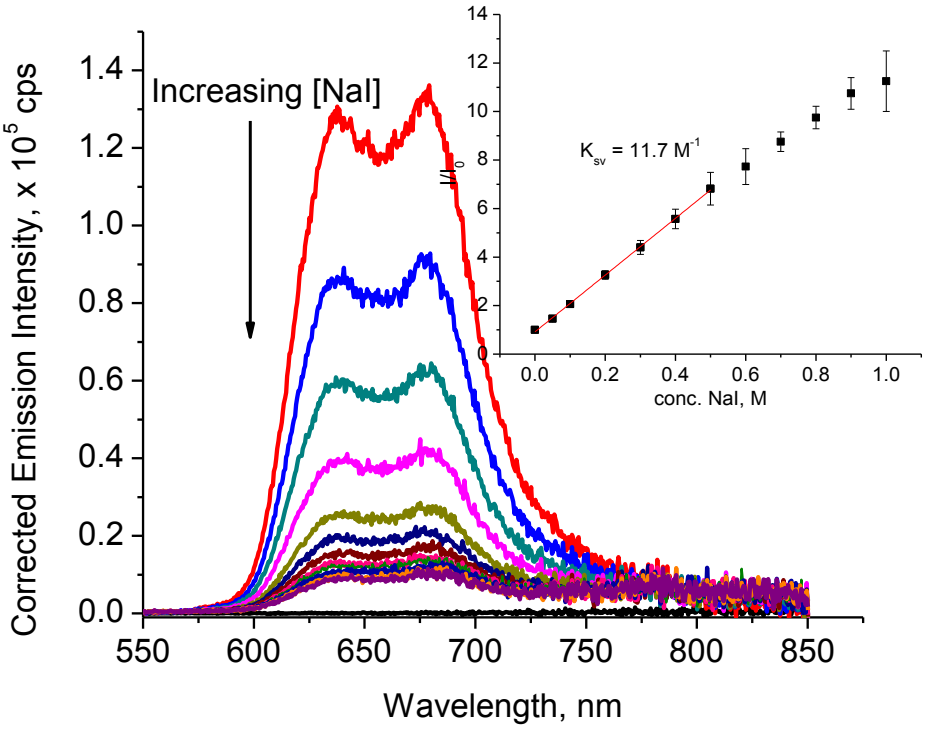

Figure 3.4 Corrected S_1 fluorescence spectra of aqueous solutions of ZnTMPyP (λ_{ex} = 425 nm) in the presence of various concentrations of NaI ranging from 0 to 1.0 M in a constant total ionic strength of 1.0 M. Inset: Stern–Volmer plot constructed from I_0/I data vs. NaI concentration. K_{SV} from the slope of the line is 11.7 M^{-1}.

Results from time resolved measurements showed that the fluorescence decay curves were best fitted using an equation consisting of a sum of two exponential fluorescence decay terms (see Figure A3.3 in the Appendix). Our value of 1.27 ns for the fluorescence lifetime of ZnTMPyP in water (data not shown) agreed with literature values of 1.3 ns.[76] Changing the medium to 1.0 M NaCl decreased the corresponding fluorescence lifetime to 1.18 ns and introduced a significant fraction of a second shorter-lived component with a lifetime of ~0.14 ns. Table 3.1 collects the measured fluorescence lifetimes and their corresponding fractions as a function of I^- concentration. Since the

fraction of the shorter lived component was significant and its contribution to quenching cannot be ignored, we calculated the average lifetime using the equation:

$$\bar{\tau} = \sum f_i \tau_i \qquad (3.3)$$

where f_i is the fraction of species with excited state lifetime, τ_i.These values are listed in the last column of Table 3.1. Plotting the ratio of average lifetimes $\frac{\bar{\tau_0}}{\bar{\tau}}$ vs. [Q] (see Figure A3.4 in the Appendix) gave a K_{SV} of 10.1 ± 0.1 M^{-1} which agreed well with the value obtained from steady state measurements.

Table 3.1 Fluorescence lifetimes and the corresponding fractions of the total emission obtained by iterative convolution of a biexponential fitting function with the instrument response function for excitation of aqueous ZnTMPyP at 430 nm.

[NaI]	[NaCl]	τ_1, ns	f_1	τ_2, ns	f_2	τ_{ave}
0.00	1.00	1.18	0.98	0.14	0.02	1.16
0.10	0.90	0.66	0.88	0.24	0.12	0.61
0.20	0.80	0.45	0.77	0.21	0.23	0.40
0.30	0.70	0.35	0.65	0.19	0.35	0.29
0.40	0.60	0.27	0.71	0.13	0.29	0.23
0.50	0.50	0.24	0.50	0.15	0.50	0.19

As seen in Table 3.1, the lifetime of the longer lived component decreases with increasing [NaI] whereas that of the shorter-lived component fluctuates around a mean of 0.18 ns. These results indicate that the ZnTMPyP quenching by iodide ion follows a combination of dynamic and static quenching. The dynamic quenching rate constant can

be determined experimentally from time-resolved fluorescence decay curves of ZnTMPyP in the absence and presence of iodide. The time resolved fluorescence data were fitted using an equation consisting of a sum of two exponential fluorescence decay terms. The longer lifetime component was assigned to emission from the excited S_1 state of ZnTMPyP quenched diffusionally by iodide. The shorter lifetime component is likely associated with an excited state complex. We used the decreasing fluorescence lifetimes shown in Table 3.1 to construct a Stern–Volmer plot (Figure A3.5 in the Appendix) using:

$$\frac{\tau_0}{\tau} = 1 + K'_{SV}[Q] \qquad (3.4)$$

where τ_0 and τ are the fluorescence lifetimes in the absence and presence of quencher, respectively, and K'_{SV} is the dynamic Stern–Volmer quenching constant. The K'_{SV} value of ZnTMPyP obtained from the slope of the SV plot shown in Figure A3.5 in the Appendix was 8.1 ± 0.2 M^{-1} which gives 6.8 × 10^9 M^{-1} s^{-1} as the value of the bimolecular quenching rate constant. This value is close to the theoretical value of the diffusion limited bimolecular interaction rate constant of ~10^{10} M^{-1} s^{-1} in water.

The bimolecular quenching rate constant, k_Q, is a useful parameter that gives information on the efficiency of quenching. It is the product of the quenching efficiency, γ, multiplied by the diffusion limited bimolecular rate constant for collision, k_{DS}. The theoretical rate constant for diffusion-limited bimolecular interaction between ZnTMPyP and iodide ions in solution, k_{DS}, is calculated from the Debye-Smoluchowski equation:

$$k_{DS} = k_S \frac{r_c/R}{\exp\left(\frac{r_c}{R}\right)-1} \qquad (3.5)$$

where k_s is the Smoluchowski diffusional rate constant, R is the sum of the radii of ZnTMPyP which is equal to 7 Å and iodide which is equal to 2.2 and r_c is the Onsager length and is given by

$$r_c = \frac{Z_1 Z_2 e^2}{4\pi\varepsilon k_B T} \quad (3.6)$$

where Z_1e is the charge of the fluorophore ($ZnTMPyP^{4+}$), Z_2e is the charge of the quencher (I^-).[79] The Smoluchowski diffusional rate constant can be calculated using

$$k_S = 1000\ x\ 4\pi N_A R(D_{ZnTMPyP^{4+}} + D_{I^-}) \quad (3.7)$$

where N_A is the Avogadro's number, R is as defined above and $D_{ZnTMPyP^{4+}}$ and D_{I^-} are the diffusion coefficients of $ZnTMPyP^{4+}$ and I^-, respectively. Values of the diffusion coefficients were calculated from the Stokes-Einstein equation. Equations 3.5-3.7 return a value of 2.95 x 10^{10} $M^{-1}s^{-1}$ for the diffusion-limited bimolecular interaction rate constant, k_{DS}, between $ZnTMPyP^{4+}$ and I^- in solution 1.0 M ionic strength at 25 °C. This value is 20 times higher than the k_{DS} calculated for the interaction between $ZnTPPS^{4-}$ and I^-, consistent with the different charges on the chromophore. However, the experimentally determined bimolecular quenching rate constant was augmented only by a factor of 4 when replacing repulsive interactions between $ZnTPPS^{4-}$ and iodide by the attractive interactions between $ZnTMPyP^{4+}$ and iodide. We assign this discrepancy to the fact that the Debye–Smoluchowski method of calculation does not take into account the presence of the counter ion, Na^+, also present at a constant 1.0 M concentration. The presence of Na^+ ions diminishes both the attractive interaction between $ZnTMPyP^{4+}$ and I^- and the repulsive interaction between $ZnTPPS^{4-}$ and I^- with the net effect of decreasing the

difference between the two bimolecular quenching rate constants. From the experimentally determined k_Q and the calculated k_{DS}, the quenching efficiency determined for a [ZnTMPyP^{4+}–I$^-$] encounter pair was only 0.23 despite the fact that iodide is often considered as an efficient quencher with values of γ close to unity. In fact, γ is equal to 0.95 in the [ZnTPPS^{4-}–I$^-$] encounter pair, recalculated from data reported by Lebold *et al*.[79] One would have expected to get a better quenching efficiency between an attractive pair compared with that of a repulsive pair. Examination of the experimentally determined K_{SV} values indeed indicate iodide was a better quencher for the ZnTMPyP excited state than it was for the ZnTPPS excited state. From the reciprocal of K_{SV}, the iodide concentration required to quench half of the ZnTMPyP S_1 fluorescence was only 0.10 M while a concentration of 0.40 M was required to quench half of the ZnTPPS S_1 fluorescence. This could be due to differences in the quenching mechanism followed by the two systems and to the negating effects of the 1.0 M Na^+ counter ions discussed previously. ZnTPPS S_1 state quenching by iodide follows almost exclusively a dynamic quenching mechanism while that of ZnTMPyP follows a more complex quenching mechanism which includes quenching due to ground state ion-pair formation.

For the static contribution to quenching, we examined the steady state emission data for contributions from a non-fluorescent ground state complex between porphyrin and iodide using the modified Stern-Volmer equation shown below:

$$\frac{I_0}{I} = (1 + K'_{SV}[Q])(1 + K_{SV}[Q]) \qquad (3.8)$$

where the first term is the dynamic contribution and the second term is the static contribution to quenching. Solving for the roots of the quadratic equation gives 6.92 M^{-1}

and 1.91 M^{-1}. Since, we already know that K'_{SV} is 8.08 ± 0.19 M^{-1} from fluorescence lifetime measurements, we assign the higher value to the dynamic contribution and the lower value to the static contribution to quenching. A static quenching constant of 1.91 M^{-1} indicates a weak association and supports the earlier hypothesis that the ZnTMPyP and iodide do not form extensive ground state aggregates.

We, thus examined the static contribution to quenching that arises from the close proximity of fluorophore and quencher at the moment of excitation. We use the equation given below to determine the effective quenching sphere, where V is the quenching sphere volume and N_A is Avogadro's number.

$$\frac{I_0}{I} = (1 + K'_{SV}[Q])\exp(VN_A[Q]) \qquad (3.9)$$

We used Grace plotting tool to fit (3.9) on the experimental data fitting only from 0.00 M to 0.50 M concentrations of quencher since our time resolved measurements were done at this range only. Our best fit returned an equation: $\frac{I_0}{I} = (1 + 10.7386[Q])\exp(0.1619[Q])$ and calculated the quenching radii for iodide to be 4.0 Å. This radius was slightly lower than 9.2 Å, the sum of the radii of $ZnTMPyP^{4+}$ and I^- ions, indicating that not every encounter between the ions lead to quenching, in agreement with the low quenching efficiency previously calculated. Equation (3.9) did not give meaningful results when fitted beyond 0.50 M concentration of iodide.

To confirm that the quenching mechanism followed by the ZnTMPyP-iodide system was a combination of dynamic and static quenching, we performed a similar experiment using spectrophotometric grade ethylene glycol, a high viscosity solvent.

The diffusion limited quenching rate constant is inversely proportional to the viscosity of the media; we, therefore, expected a decrease in the dynamic quenching rate constant in the ethylene glycol solvent. Further, the weak association between $ZnTMPyP^{4+}$ and I^- could be attributed to a loose ion pair formation. Increasing solvent viscosity was expected to decrease the diffusion of the ion pairs away from each other and would result in a higher contribution from static quenching. Table 3.2 showed the fluorescence lifetime values of ZnTMPyP in ethylene glycol and their corresponding fractions as a function of I^- concentration. Similar to that observed in aqueous solutions, the fluorescence decay curves were best fit with a trial equation consisting of a sum of two exponential fluorescence decay terms. The notable difference between the two systems was that the second component was longer-lived (0.47–0.49 ns) compared to that in aqueous solutions (0.13–0.24 ns). The Stern–Volmer plot (see Figure A3.6 in the Appendix) constructed from τ_0/τ gave a K'_{SV} equal to 1.59 ± 0.03 M^{-1} corresponding to a k_Q value of 1.17×10^9 $M^{-1}\,s^{-1}$. This k_Q value was qualitatively lower than the rate constant measured in aqueous solutions, thus, confirming our hypothesis (*vide supra*). The K_{SV} obtained from steady state measurements in ethylene glycol solutions is 3.03 M^{-1}. This is different from the K'_{SV} from lifetime measurements which can be attributed to the association constant for the weak ground state ion-pair formation between $ZnTMPyP^{4+}$ and I^-. Note, however, that its contribution to quenching was significantly greater than that observed in aqueous solutions.

Table 3.2 Fluorescence lifetimes and the corresponding fractions of the total emission obtained by iterative convolution of a biexponential fitting function with the instrument response function for excitation of ethylene glycol solutions of ZnTMPyP at 430 nm.

[NaI]	[NaCl]	τ_1, ns	f_1	τ_2, ns	f_2
0.00	1.00	1.36	0.98	0.47	0.02
0.10	0.90	1.15	0.93	0.49	0.07
0.20	0.80	1.01	0.90	0.49	0.10
0.30	0.70	0.91	0.79	0.49	0.21
0.40	0.60	0.83	0.74	0.47	0.26
0.50	0.50	0.75	0.70	0.47	0.30

The observation of the significant quenching of S_1 states by iodide, commonly used as a component for dye-sensitized solar cells (DSSC) is important. Durrant and coworkers[80] have reported DSSC systems with electron injection from the excited state of the sensitizer dye to the semiconductor electrode that are slower than the excited state decay. Slow electron injection rates reduce efficiencies by allowing for competition from kinetics of fluorophore excited state decay or from kinetics of the excited state quenching by the iodide in the electrolyte systems. NCPU-TTA enhanced DSSCs using dual absorber up-converters such as MPs, use the upper singlet state produced on triplet–triplet annihilation in the absorbing dye as the sensitizer. If the short-lived S_2 states of the dye are not quenched by the iodide in the DSSC electrolyte system, then, no significant loss of efficiency due to quenching is introduced.

We thus examined if the ZnTMPyP S_2 is quenched as efficiently by iodide as is the

S_1 state. Aqueous ZnTMPyP exhibited a very weak emission band centered at around 450 nm which was attributed to the S_2 state emission (Figure 3.5). Monitoring this emission as the iodide concentration was increased showed that the S_2 emission was also quenched by iodide but to a considerably smaller extent than for S_1 quenching. The Stern–Volmer plot in Figure 3.5 shows quenching of the S_2 state of ZnTMPyP by iodide ions is linear with K_{SV} = 0.78 ± 0.02 M^{-1}. Since the lifetime of the S_2 excited state of ZnTMPyP is <100 fs, we eliminate any possible dynamic quenching contribution and attribute the decrease in S_2 emission intensities with increasing iodide concentration to a "sphere of action" static quenching mechanism described by the equation:

$$\frac{I_0}{I} = (1 + K'_{SV}[Q])\exp(1000VN_A[Q])$$

$$= (1 + K'_{SV}[Q])(1 + VN_A[Q] + \cdots) \qquad (3.10)$$

where V is the volume of the quenching sphere, N_A is the Avogadro's number, and K'_{SV} and [Q] are as defined previously. Neglecting the first term since dynamic quenching is insignificant when $\tau_0 < 1 \times 10^{-13}$ s, we find a quenching sphere volume and radius of 1.3×10^{-27} m^3 and 0.68 nm, respectively. The calculated radius is smaller than the sum of the radii of ZnTMPyP and I^- (0.92 nm) but greater than the sum of the radii of the free Zn^{2+} and I^- (0.33 nm). This suggests that contact of the two ions is required for quenching to occur. In contrast to the ZnTPPS–iodide system where a very tight approach of quencher (axial position immediately adjacent to the central zinc atom) was necessary for quenching to happen [73], the ZnTMPyP–iodide system can allow for quencher approach from the periphery of the molecule.

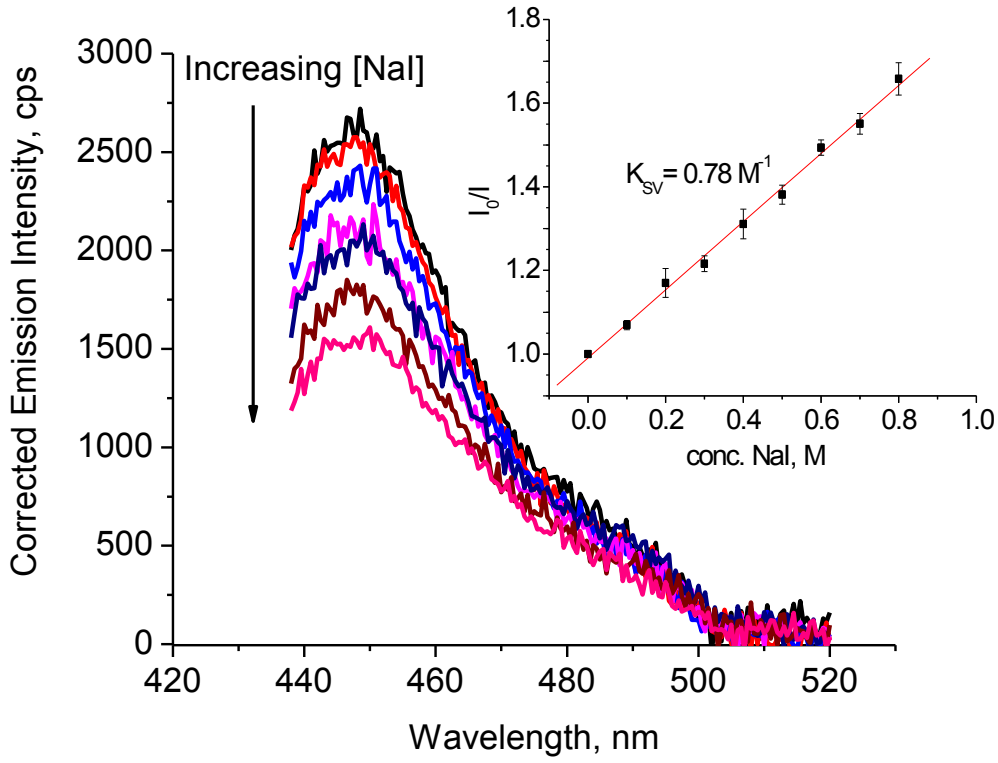

Figure 3.5 Corrected S_2 emission spectra of aqueous solutions of ZnTMPyP (ex = 425 nm) in the presence of various concentrations of NaI ranging from 0 to 1.0 M in a constant total ionic strength of 1.0 M. **Inset:** Stern-Volmer plot I_0/I of S_2 state of 5 μM ZnTMPyP. The K_{SV} from the slope of the line is 0.78 M^{-1}.

The quenching of S_2 emission of $ZnTPPS^{4-}$ by iodide was shown to be the result of an electron transfer [73, 79]. Due to the very fast decay of the S_2 fluorescence in ZnTMPyP (<100 fs), we were not able to determine the rate of the corresponding electron transfer process. Using only our steady state emission measurements to calculate the energy of the ZnTMPyP S_2 state, E_{00} (≈2.88 eV), and the equation for the Gibbs free energy change for the electron-transfer process ($\Delta G° = E_{ox} - E_{red} - E_{00}$, assuming negligible Coulombic attraction energy in water) from the iodide (E_{ox} = 1.33 V) to the S_2 state of ZnTMPyP (E_{red} = −0.85 V), we obtain a value of $\Delta G° \approx -0.70$ eV.[20] The negative value indicated that

electron transfer from S_2 is favourable within the quenching sphere of action, and should therefore be responsible for the observed fluorescence quenching process.

3.5 Conclusions

In summary, we have investigated the effect of iodide, a component of redox couples often used in dye-sensitized solar cells, on the spectroscopic properties of the water-soluble porphyrin, ZnTMPyP. We have demonstrated that iodide-quenching of the ZnTMPyP S_1 state is significant but quenching of the S_2 state is minimal. The results presented in this work provide important implications on the design of dye-sensitized solar cells, particularly those whose cell efficiencies are enhanced by incorporating a layer of an organic photon up-converter in their designs.

CHAPTER 4. HOMO-MOLECULAR NON-COHERENT PHOTON UP-CONVERSION BY TRIPLET-TRIPLET ANNIHILATION USING A ZINC PORPHYRIN ON WIDE BANDGAP SEMICONDUCTORS

In the previous chapter, it was determined that iodide-quenching of the ZnTMPyP S_1 state is significant but quenching of the S_2 state is minimal. This means that MPs have the potential to be incorporated in the design of DSSCs, particularly by including it as a photon up-converter layer in conventional DSSC designs as imagined in the cartoon depiction in Figure 4.1. However, before MPs can be incorporated in real devices, there are aspects of its implementation that need to be understood. Particularly, the relationship between S_1 and S_2 level of closed-shell MPs to the photoanode band gap need to be explored. For *homo*-NCPU-TTA to be useful in practical devices, the loss of energy by electron transfer from the lower excited singlet states (S_1 in the case of the MPs) must be minimized. This can be achieved by choosing a semiconductor whose conduction band energy lies between those of the upconverted and the absorbing states of the dual absorber/up-converter – *e. g*. between S_2 and S_1 of a closed-shell MP. The conduction band of TiO_2, a common DSSC photoanode, lies below S_1. The band gap of ZrO_2, on the other hand, is known to be above S_2. In this chapter, the approach of mixing TiO_2 and ZrO_2 to tune the band gap of the photoanode to the desired level is described. The photophysics of ZnTPP, as a model dual absorber/up-converter system, on TiO_2, ZrO_2 and mixed TiO_2-ZrO_2 surfaces were examined in order to understand the conditions needed to implement *homo*-NCPU-TTA in a DSSC device.

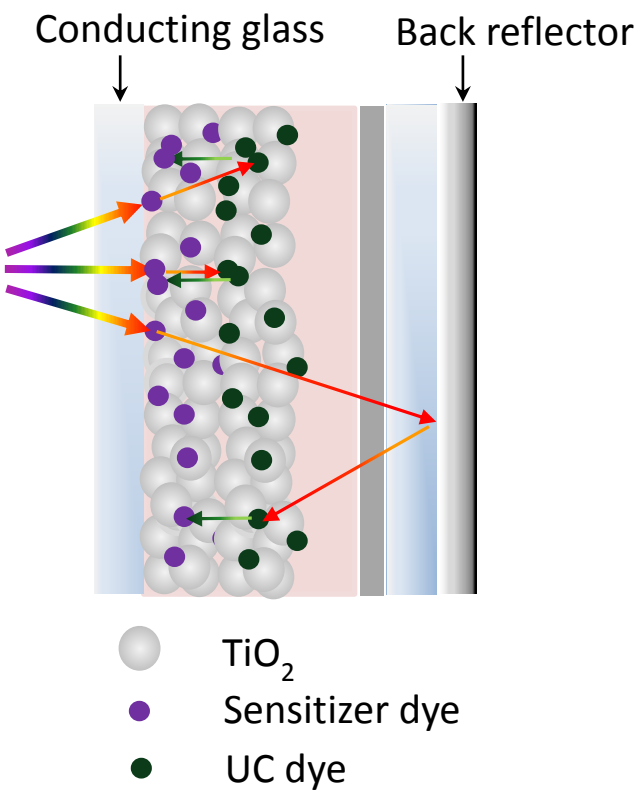

Figure 4.1 Cartoon of an imagined DSSC device incorporating MPs on TiO_2 as an additional photon up-converting layer.

This chapter is reprinted with minor revisions from a paper published in *Chemical Physics Letters* **2014,** 598, 17-22 (Reproduced from Ref. 80 with permission from Elsevier under license number: 3805120565593).[81]

The thesis author's contribution to this report include: preparation of TiO_2, ZrO_2 and mixed TiO_2/ZrO_2 thin films; profilometry data collection and analysis; diffuse reflectance spectra collection and Tauc plot generation. The author assisted Dr. Neeraj K. Giri in collecting steady state absorption and emission spectra as well as in measuring the upconverted emission of ZnTPP on metal oxide films. Dr. Neeraj K. Giri was mainly responsible for: synthesizing the metal oxide powders; collecting TEM images of the

metal oxide powders; and working with Dr. Andrew Grosvenor's group in collecting and interpreting powder XRD data. Both junior authors prepared the experimental as well as the results and discussion portion of the manuscript. Dr. Matthew Paige and Dr. Ron Steer wrote the introduction and conclusion part of the manuscript in addition to providing extensive guidance in planning the experimental work and interpreting results.

HOMO-MOLECULAR NON-COHERENT PHOTON UP-CONVERSION BY TRIPLET-TRIPLET ANNIHILATION USING A ZINC PORPHYRIN ON WIDE BANDGAP SEMICONDUCTORS

Neeraj K. Giri, Concepcion P. Ponce, Ronald P. Steer* and Matthew F. Paige*

Department of Chemistry, University of Saskatchewan, 110 Science Place, Saskatoon, Saskatchewan, Canada

4.1 Abstract

Non-coherent up-conversion, realized by homomolecular triplet–triplet annihilation of a zinc MP absorber, has been measured for the MP adsorbed on metal oxide films (ZrO_2, TiO_2 and ZrO_2/TiO_2 mixed oxides) in which the semiconductor conduction band energy lies between the MP's up-converted and prompt S_1 excited states. Up-converted emission was observed for pure and mixed metal oxide films, regardless of the relative energies of the states, indicating electron transfer from up-converted states to the semiconductor was not competitive. Up-conversion was attributed to aggregation of the absorber, likely in defects on the films, leading to efficient homomolecular triplet–triplet annihilation.

4.2 Introduction

It was noted in Chapter 1.3 that the efficiencies of single-junction solar cells and conventional dye-sensitized solar cells (DSSCs) are determined in principle by the Shockley-Queisser limit [82] and in practice by a wide range of interconnected dynamic processes involving charge separation and transport.[83] One of the major parasitic losses affecting efficiencies of PVs is called transmission or sub-bandgap loss, which depends

on the absorption threshold of the considered solar-cell technology. Photons with energies below the solar cell's absorption threshold do not provide sufficient energy for the excitation of electron–hole pairs or excitation of the sensitizer dyes. Approaches such as exciton splitting[84] and non-coherent photon up-conversion (NCPU),[25, 85] hold promise of circumventing the theoretical power conversion efficiency limit (*ca*. 34% for single threshold devices such as those based on silicon semiconductors). As depicted in Figure 4.1, NCPU circumvents these transmission losses by converting low-energy photons that are not absorbed by the main sensitizer dye into a usable high-energy photon.

The more frequently employed NCPU scheme is based on a sensitized process involving two organic components.[14] One component (the dye) strongly absorbs red and near infrared solar photons, produces triplet states in high yield and serves as a triplet energy donor (sensitizer) to the second component (the up-converter). The up-converter is chosen so that its triplet state is long-lived, is in near resonance with the dye triplet, has a large singlet-triplet energy gap and is strongly radiative from its lowest excited singlet state (which produces fluorescence in a range to the blue of the red-end absorption limit of the dye). Triplet-triplet energy transfer from the dye to the up-converter then can occur with high efficiency if the concentration of the up-converter is sufficiently large. Energy transfer to the up-converter is then followed by diffusional processes that enable pooling of some fraction of the electronic energy of two up-converter triplets by triplet-triplet annihilation (TTA) to form one short-lived highly fluorescent excited singlet state and one ground singlet state of the up-converter species. Blue-shifted (up-converted) delayed fluorescence of the radiating excited singlet state then can be used to augment the

incident photon flux of a conventional DSSC dye in a tandem cell [86-88] and can thus improve the overall power conversion efficiency.

A second, less frequently reported scheme involves using one organic component to serve as both absorbing dye and up-converter.[17, 18, 89] Here the requirements of the absorber/up-converter and its function are different from those of the two-component system but are chosen to serve the same purpose of increasing overall power conversion efficiency. In this scheme, the absorber must exhibit a large molar absorptivity throughout the near uv to near infrared region so as to capture as large a fraction of the solar spectrum as possible. It should also have a large triplet quantum yield, preferably with a minimum of energy loss – *i.e.* it should have an $S_1 - T_1$ energy spacing that is only as large as needed to minimize absorbed energy loss by back-intersystem crossing. The triplet must also be relatively long-lived (as is the case with the up-converter in the two-component scheme). The major difference between the sensitized two-component system and this one-component system is that TTA occurs in the absorber/up-converter itself and must produce an excited singlet state, S_n $n>1$, that is higher in energy than S_1, but nevertheless sufficiently long-lived to act as either an energy donor or (preferably) an electron donor.

The classes of organic compounds that exhibit the properties required for such a dual absorption/up-conversion function include MPs, aromatic thiones and non-alternant aromatic hydrocarbons, but are nonetheless rather limited in number.[90-92] Nevertheless, the closed-shell MPs in particular show promise of utility for the following reasons. First, the energy losses associated with producing the upconverted singlet state can be minimized because the TTA process favours the formation of a strongly radiative excited

singlet state that is resonant with twice the energy of the interacting triplet, *i.e.* $2T_1 \rightarrow S_n$ (n>1) + S_0 favors that excited singlet in which $2\Delta(T_1\text{-}S_0) \cong \Delta(S_n\text{-}S_0)$ and where the $S_n - S_0$ radiative transition has a large oscillator strength.[93] In the case of the closed shell MPs the favored product state is the same as that produced on one-photon excitation in their strong Soret bands (nominally S_2). Second, a significant number of closed-shell MPs have S_2 excited states with lifetimes in the picosecond range – short, but long enough to act as efficient energy and/or electron donors in well-chosen materials.[17, 18, 77, 89, 94-101] Third, the triplets of many potential dual absorber/up-converters can be formed by intersystem crossing in high yield with minimal thermal energy loss and have lifetimes in the tens or hundreds of microsecond range.[44] Fourth, derivatives of the MPs can exhibit strong photon absorption well into the near infrared, thus serving to capture a larger fraction of the solar spectrum than conventional dyes.[102] Finally, because the upconverted state lies at high energy relative to the threshold for photon absorption, the bandgap of the semiconductor used for electron capture can be larger than that employed in a single threshold device, leading to a potentially larger open-circuit voltage.

On the other hand, several potential problems associated with the practical implementation of dual absorbers/up-converters in DSSCs remain to be investigated. First, it is essential that electron transport from the upconverted state of the absorber to the conduction band of the supporting semiconductor be extremely fast – in the 100s of fs range if MPs are to be used. This goal is difficult but not in principle impossible to reach, and there has been significant progress in determining the structures of potentially useful materials that meet this requirement.[98, 101, 103] Second, the loss of charge separation by electron-hole recombination or by electron transfer from the lower excited singlet states

(S_1 in the case of the MPs) must be minimized. In practice this should involve the choice of a semiconductor whose conduction band energy lies between those of the upconverted and the absorbing states of the dual absorber/up-converter – *e. g*. between S_2 and S_1 of a closed-shell MP, as shown in Figure 4.2.

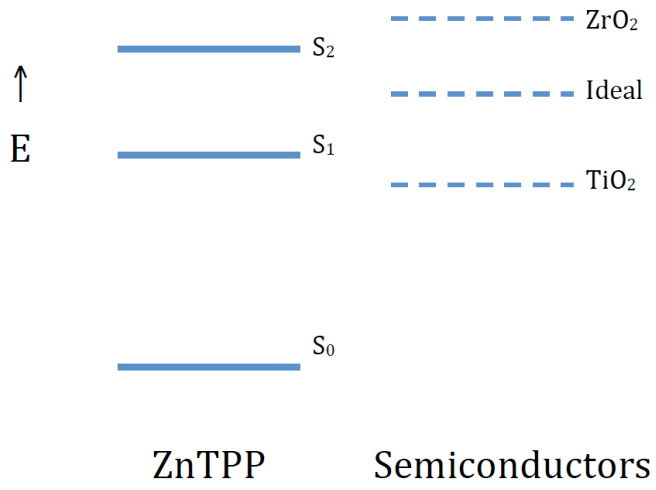

Figure 4.2. Energy levels in a dual absorber/up-converter DSSC based on ZnTPP relative to the energies of selected semiconductor conduction bands.

Photon up-conversion by two-component sensitized TTA on various mesoporous semiconductors has been observed previously.[47, 58] In particular, Moranderia and coworkers[47] have demonstrated that zirconia (ZrO_2), whose conduction band lies higher in energy than that of the emitting state of the up-converter, can act as a proxy for examining the photophysics of chemisorbed and physi-sorbed materials on mesoporous wide bandgap semiconductors relevant to DSSCs. Here we examine the photophysical behaviour of a model dual absorber/up-converter system, zinc tetraphenylporphyrin, on

zirconia and titania in order to elucidate the conditions needed to use this method in a practical device.

4.3 Experimental

4.3.1 Synthesis and characterization of metal oxides

Zirconium(IV) oxynitrate hydrate ($ZrO(NO_3)_2\_xH_2O$) (99.0% pure; Sigma–Aldrich), titanium(IV) isopropoxide (P99.0% pure; Sigma–Aldrich), glycine (99.0% pure; Alfa-Aesar), Aeroxide TiO_2 P25 (donated by Nippon Aerosil Co., Ltd.), ethyl cellulose, EC-46 (46 cP; Sigma–Aldrich), EC-10 (10 cP; Sigma–Aldrich) and terpineol (Sigma–Aldrich) were used as received. ZrO_2 was prepared using a solution combustion synthesis method. [104, 105] Briefly, zirconyl nitrate and glycine, the latter which served as a combustion fuel, were dissolved in deionized water and stirred continuously until a clear solution with no undissolved solid was obtained. The solution was heated at 60 °C with stirring to form a transparent gel, which was annealed in a furnace at 600 °C for 24 h. The ZrO_2/TiO_2 mixed oxides were prepared in a similar manner but with the addition of 'x' moles of titanyl nitrate ($TiO(NO_3)_2$) synthesized by the hydrolysis of titanium isopropoxide [106] to (1-x) moles of zirconyl nitrate and glycine. Samples were labeled as ZrO_2/TiO_2 (n) where n indicates the mole fraction of titanium present.

The phase composition and crystallinity of the nanoparticles were characterized using powder X-ray Diffraction (XRD) with a PANalytical Empyrean diffractometer and Co $Ka_{1,2}$ radiation. The mean crystallite size of samples can be estimated from Debye–Scherrer equation, as

$$D = \frac{0.89\lambda}{\beta cos\theta} \quad (4.1)$$

where D = crystallite size (in nm), λ = X-ray wavelength (1.789 Å), β = full width at half maximum (FWHM in radians), θ = Bragg diffraction angle. Particle sizes of samples were measured from transmission electron micrographs collected with a Philips CM10 TEM operating at 80 kV. High score plus software has been used to analyze the XRD data.

4.3.2 Preparation and characterization of ZrO_2, ZrO_2/TiO_2, TiO_2 films

ZrO_2, ZrO_2/TiO_2 mixed oxides and Aeroxide TiO_2 P25 were made into pastes following the procedure outlined by Ito *et al.*[107] with slight modifications. Two grams of the oxides were mixed with 2.5 g and 2.0 g of 10 wt % EC-10 and EC- 46 in ethanol, respectively. Four grams of terpineol were added and the mixtures diluted with ethanol. The mixtures were then homogenized with an ultrasonic horn operated with a duty cycle of 1 min work and 1 min rest for a total of thirty minutes. The ethanol was then evaporated in a rotary evaporator to make thick oxide pastes. The resulting pastes were coated onto piranha solution-cleaned glass slides using the "doctor-blade technique" to make thin films that were then gradually sintered in air at the following temperatures: 150°C for 10 min; 325°C for 5 min, 375°C for 5 min, 450°C for 15 min, and finally 500°C for 15 min. The thickness of the films were measured using a KLA-Tencor D120 profilometer and the band gaps of the oxides estimated from Tauc plots[108] derived from spectra of the films collected with the Diffuse Reflectance Accessory 1800 of a Varian Cary 6000i UV-Vis spectrophotometer.

4.3.3 Spectroscopic Characterization of dye loaded films

The sintered films were then soaked in 2mM ZnTPP in toluene for 24 hours, then dried in nitrogen and degassed prior to spectroscopic characterization. Steady state

absorption and emission spectra as well as upconverted emission spectra of degassed samples were collected using the instrumentation described in Chapter 2.

4.4 Results and Discussion

4.4.1 Characterization of metal oxide powders

Some as-synthesized samples (ZrO_2 and mixed oxides) exhibited photoluminescence upon 405 nm laser excitation; this photoluminescence has been attributed to oxygen vacancies[109] and can be minimized by further annealing at higher temperatures. [110] Hence, these samples were further annealed at 850 °C for 2 h. The photoluminescence was significantly reduced after annealing and appeared with very small intensity (425–500 nm region) relative to the fluorescence emission of the ZnTPP dye when excited with 405 nm laser (See Figure A4.1 in the Appendix). No photoluminescence of ZrO_2 and mixed oxide films was observed on 532 nm excitation and therefore we expect the S_2 emission (410–475 nm) of ZnTPP will be unaffected by this oxygen-vacancy source. The metal oxide samples consisted of nanoparticulate matter, with particle sizes (30–80 nm; Figure A4.2 in in the Appendix) as well as phase composition and crystal structure determined by TEM and XRD, respectively. The XRD patterns (Figure A4.3 in the Appendix) of the pure ZrO_2 matched well with the characteristic peaks of the monoclinic (88.8%), tetragonal (8.8%) and cubic (2.5%) phases of ZrO_2, which belong to the P121/c1, P42/nmc and Fm-3m space groups, respectively. When Ti was added to ZrO_2, the tetragonal phase was predominant; for ZrO_2/TiO_2 (0.02), 41.5% was monoclinic and 58.5% was tetragonal while for ZrO_2/TiO_2 (0.40), the monoclinic ZrO_2 phase completely disappeared, suggesting a complete transformation to the tetragonal phase. This is consistent with the stabilization of

tetragonal phase ZrO_2 at higher Ti concentrations as reported previously by Gionco *et al.*[111] However, even for higher concentrations of Ti, no TiO_2 phase was observed. This is likely due to the formation of a solid solution between ZrO_2 and TiO_2.[111, 112] The X-ray diffraction peaks of ZrO_2/TiO_2 (0.40) were broadened relative to the other samples indicating that the constituent crystallites were smaller. This is consistent with the particle sizes measured from the TEM images. The XRD pattern for TiO_2 (Aeroxide P25) indicated the presence of anatase (90.5%) and rutile (9.5%) phases. The average crystallite sizes for ZrO_2, ZrO_2/TiO_2 (0.02), ZrO_2/TiO_2 (0.40) and TiO_2 (Aeroxide P25) were calculated as 55 nm, 48 nm, 28 nm and 50 nm respectively.

4.4.2 Characterization of metal oxide films

Films prepared from the pure and mixed oxides ranged in thickness from *ca.* 1 μm to 22 μm (Figure A4.4 in the Appendix). When possible, spectroscopic measurements were taken from films with comparable thicknesses. From the diffuse reflectance spectra of the films, Tauc plots were constructed (Figure 4.3) to estimate the optical band gaps of the oxides, as summarized in Table 1 (band gaps determined as detailed in).[108] These estimated band gaps for TiO_2 and ZrO_2 agreed well with the range of values typically reported in the literature: 3.0–3.4 eV for TiO_2 and 5.0– 5.3 eV for ZrO_2.[113-115] Band gaps for the mixed oxides are more difficult to compare with literature values because finding mixtures with comparable phase composition and structures is difficult; nonetheless the values reported here are consistent with those reported for similar systems.[114, 115]

A 1.4 eV red shift in the band gap for the mixed oxides containing the highest mole fraction of Ti (n = 0.40) relative to pure ZrO_2 was observed. This red shift has also been observed by Livraghi *et al.* in Ti-loaded ZrO_2 synthesized by sol–gel synthesis or wet

impregnation.[115] The key result for up-conversion measurements is that the band gap energies of the mixed oxides fall between the values for TiO_2, whose band gap energy is below the S_1 state of ZnTPP, and ZrO_2 whose band gap energy is above the S_2 state of ZnTPP. Thus, the mixed oxides have the appropriate energy level spacing to study the model dual absorber/up-converter system, ZnTPP, as depicted in Figure 4.2.

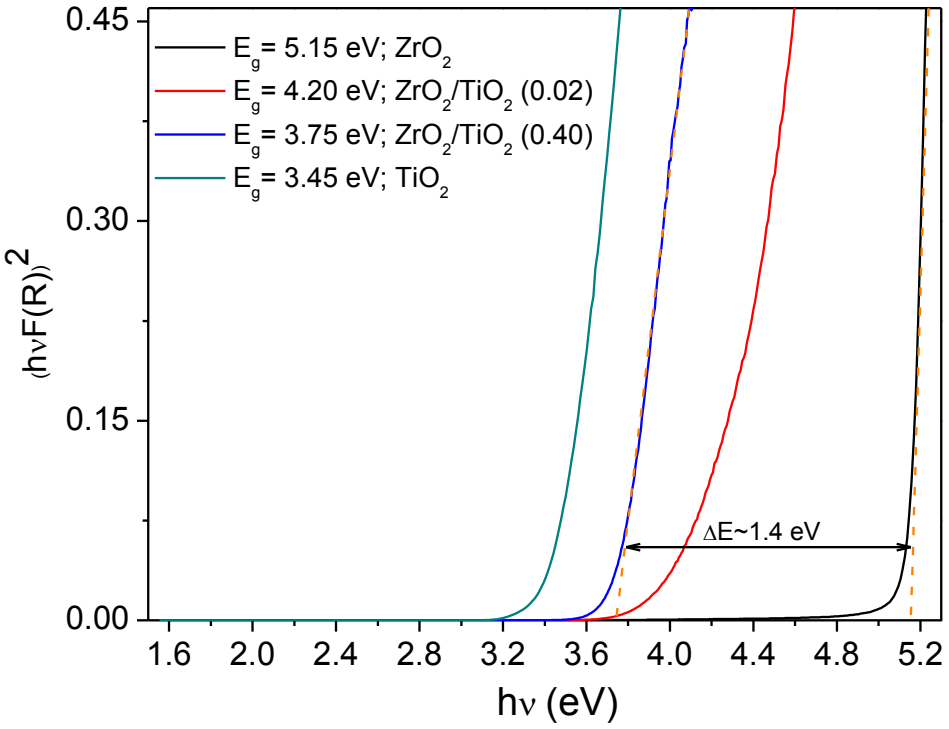

Figure 4.3 Tauc plot for band gap evaluation of ZrO_2 (E_g = 5.15 eV), mixed oxides ZrO_2/TiO_2 (0.02) (E_g = 4.20 eV), ZrO_2/TiO_2 (0.4) (E_g = 3.75 eV) and TiO_2 (Aeroxide P-25) (E_g = 3.45 eV).

4.4.2 Optical spectroscopy of dye-loaded metal oxide films

For all optical spectroscopic measurements of ZnTPP on the semiconductor films, we note that film preparation conditions lead to significant variability in the resulting data, including peak shapes, positions and spectral intensities (including absorption, normal and upconverted emission). The principal contributor to variability is likely a combination of the thicknesses of the films, their overall uniformity and the total accessible surface areas of the semiconductor available for dye adsorption. The latter is associated with differences in sizes and packing efficiencies of the metal oxide nanoparticles. The high degree of variability is entirely consistent with the reports of Morandeira and co-workers,[57] who noted that up-conversion efficiencies varied widely from one sample to another, depending on the film preparation conditions. Because of this variability, it was practical to interpret the data reported here in a qualitative manner only.

The steady state absorption spectra of ZnTPP in toluene consist of the characteristic absorption maxima of ZnTPP at 423 nm, which is assigned to the Soret or B(0,0) band, and at 548 nm and 586 nm, which are assigned to the Q-bands – Q(1,0) and Q(0,0), respectively. When physisorbed on the various metal oxide substrates, the ZnTPP Soret band in the diffuse reflectance spectra (Figure 4.4) was substantially broadened and red-shifted by about 7 nm. For reference, an absorption spectrum for a ZrO_2 film without normalization is presented in Figure A4.5 in the Appendix, both before and after dye-loading. Because of the film-to-film variability, no consistent trends could be identified from one type of metal oxide film to another, and within the variability of the measurements, all films showed comparable effects. Broadening of the Soret absorption band is consistent with aggregation of the ZnTPP, and has been reported previously in

our studies of ZnTPP-loaded poly(methylmethacrylate) films.[17] The extent of broadening is consistent with excitonic splitting (fitting these spectra with multiple Gaussian curves suggested that the Soret band consists of two bands centered at 413 nm and 435 nm).[116] Note also that the ratio of the molar absorptivity of the Soret band to that of the Q band is *ca.* 20 in liquid solution, but is reduced to *ca.* 2.5 upon adsorption to the metal oxide surfaces. This enhanced 'intensity borrowing' of the Q band from the Soret band has been attributed to B-Q coupling in J-aggregates.[55] The fluorescence lifetime of ZnTPP on ZrO_2 was also measured by TCSPC (Figure A4.6 in the Appendix), and showed a multi-exponential decay (characteristic of dye aggregation) with the major component having a short lifetime of 207 ps. This particular transient has previously been attributed to the radiative S_1 exciton lifetime of J-aggregates of porphyrin as reported by Verma *et al*.[55] Taken together, these data provide convincing evidence for aggregation of the ZnTPP when physisorbed on all of the metal oxide surfaces. Aggregation of the up-converter (or of the donor–acceptor up-converter pair in the case of heteromolecular up-conversion schemes) is of crucial importance for efficient up-conversion, as TTA requires donor and acceptor molecules to be in close proximity in systems where exciton diffusion is limited and Brownian diffusion is negligible, as is the case in these solid thin films.[17]

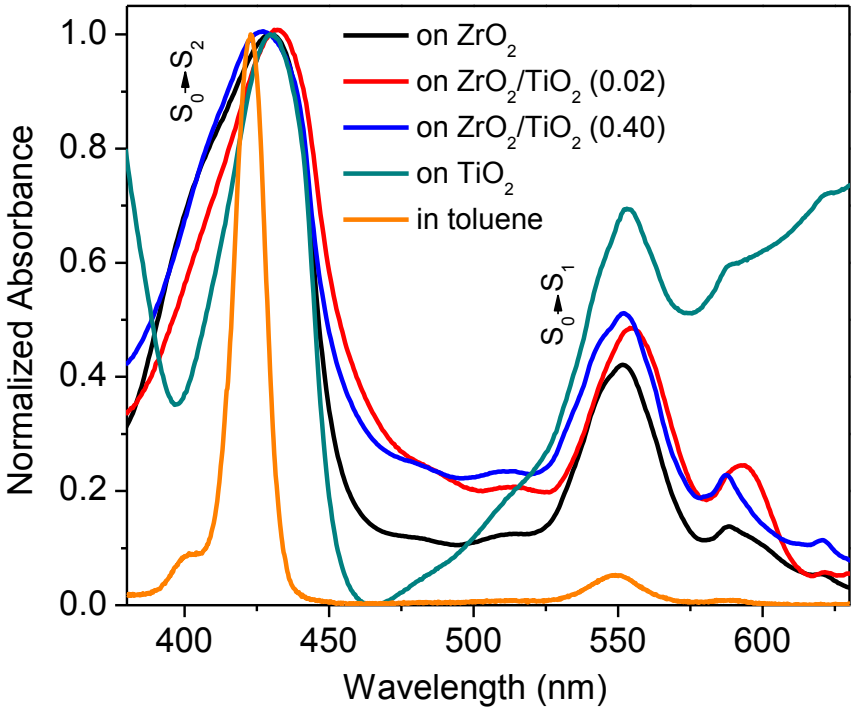

Figure 4.4. Absorption spectrum of ZnTPP loaded ZrO_2, mixed oxides ZrO_2/TiO_2 (0.02), and ZrO_2/TiO_2 (0.4) and TiO_2 (Degussa, P-25). Absorption of ZnTPP in toluene is shown as reference.

Since the interacting triplet states in homo-molecular TTA produce S_n ($n > 1$) and S_0 states of the MP, TTA can be monitored by following the S_2 emission of the dye when excited at lower energies. The upconverted S_2 and normal S_1 emission spectra of ZnTPP on oxide films excited with a low power cw 532 nm diode laser are shown in Figure 4.5. The S_2 emission (Figure 4.4A) is centered at 435–440 nm, which is red-shifted 5–10 nm from the long-wavelength Soret absorption band. The spectra have been normalized to their respective emission maxima to permit qualitative comparisons; again, precise widths, intensities and shifts of the ZnTPP spectra on different films could not be

compared quantitatively because of variability due to film preparation. Further, the S_1 emission spectra were obscured by a sharp emission peak centered at 620 nm (attributed to atomic emission of Eu impurities in the crystal of the laser excitation diode; emission spectra have been corrected for this effect). Nonetheless, both S_1 and S_2 emission was readily detectable on all the metal oxide films, including TiO_2, ZrO_2 and the mixed oxides of various compositions and film thicknesses, with S2 emission indicating homo-molecular TTA was occurring with detectable efficiency. Only de-gassed films exhibited upconverted emission, which was quenched with air saturated films (see Figure A4.7 in the Appendix).

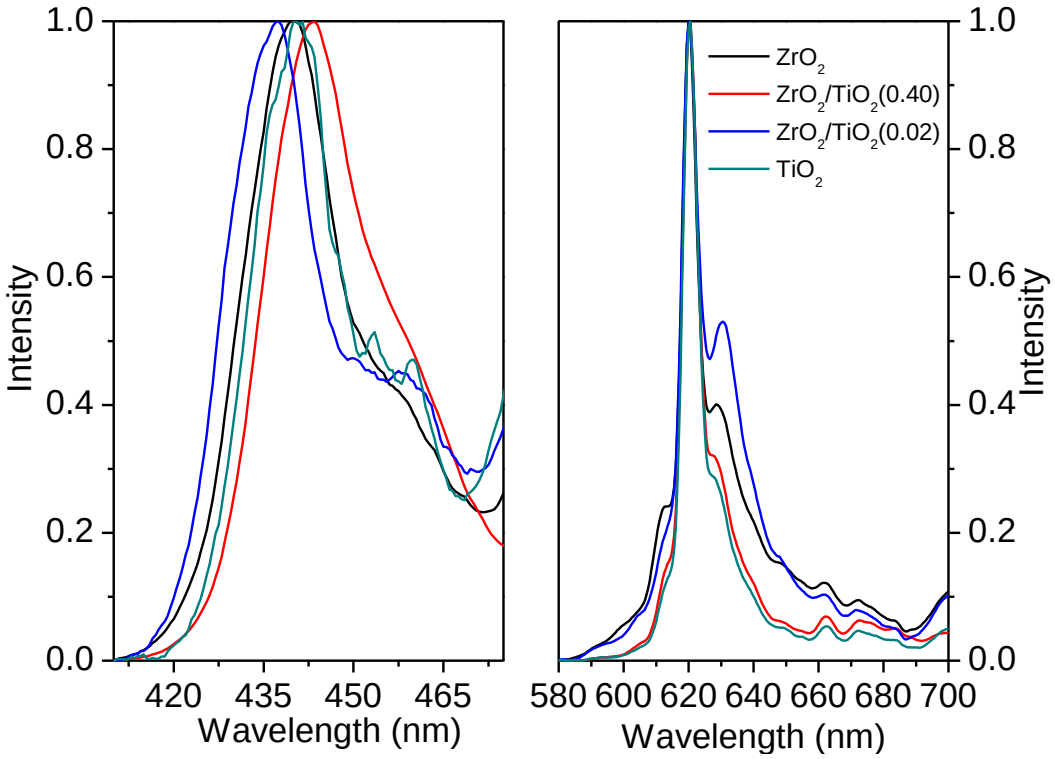

Figure 4.5. S_2 and S_1 emission spectrum of ZnTPP loaded ZrO_2, mixed oxides ZrO_2/TiO_2 (0.02), ZrO_2/TiO_2 (0.4) and TiO_2 (Aeroxide P-25) films on 532 nm laser excitation (12.03 mW) under deaerated condition.

The power density dependence of S_2 emission resulting from up-conversion was measured and is shown in Figure 4.6. The intensity of residual S_1 emission of the porphyrin can be used as a surrogate measure of the relative absorbed light intensity and the relative concentration of triplet states, as described previously for measurements in solution.[18, 117] For these measurements, ZrO_2 films were measured because the overall S_2 emission was generally larger on these substrates than for the other films investigated (vide infra). Depending on the efficiency of TTA, the slopes of these power density dependence plots may vary between 1 (linear) and 2 (quadratic). If first order radiative (phosphorescence) and non-radiative (triplet quenching and intersystem crossing from T_1 to S_0) processes dominate triplet relaxation (i.e. TTA is the rate limiting step in the overall up-conversion process), then the power dependence plot displays a quadratic behavior as a result of bimolecular triplet annihilation. At higher triplet concentrations, TTA may compete with first order triplet decay and may constitute the major decay process at very high absorbed intensities. In the latter case (the strong annihilation limit) the up-conversion intensity should vary linearly with respect to the triplet concentration, which in turn varies linearly with incident power density in these systems in which the intersystem crossing yields are large. The power dependence plot will show a slope of 1 in this case. Weisman *et al.* and other groups[43, 44, 49, 118] have suggested that highest TTA efficiency can be achieved in the region where the slope deviates from quadratic to linear.[43] This cross-over from the weak to the strong annihilation limit can be achieved by increasing the triplet concentration, which in turn can be achieved here by using a higher excitation power density, increasing the concentrations of the dual absorber/up-converter dye and choosing an excitation wavelength that coincides with strong dye absorption.[86, 118, 119] For

our power density measurements on ZrO_2, an average slope of 1.22 ± 0.11 was measured (Figure 4.6 shows the results from measuring one film; the value listed in the text is the average of multiple measurements), which given the measurement variability, we take as being reasonably close to the strong annihilation limit value of 1. The power densities used in these measurements are modest in comparison with those reported for annihilation limited TTA in liquid solutions[18, 119] for heteromolecular systems, implying that the effective concentration of up-converting species (i.e. aggregated ZnTPP) on the film is high.

The linear dependence of upconverted signal over a range of power densities, even at low excitation ones, is an unusual result, and some consideration must be given to other possible mechanisms by which the fluorescent Soret state might be reached by mechanisms other than TTA. There are no stray laser sources at or at shorter wavelengths to the S_1 absorption region, ruling out direct, trivial excitation. Neither sequential two photon absorption nor direct coherent two-photon absorption are viable mechanisms, because of symmetry reasons; single photon absorption leads to an S_1 state with *ungerade* parity and a subsequent allowed one-photon absorption would produce an upper state of *gerade* parity in the former, and coherent two-photon excitation requires *gerade* to *gerade* state symmetry as a selection rule (for unperturbed D_{4h} ZnTPP molecules) in the latter. Furthermore, the oxygen sensitivity is a powerful indicator that the upconverted emission must originate in triplet processes.

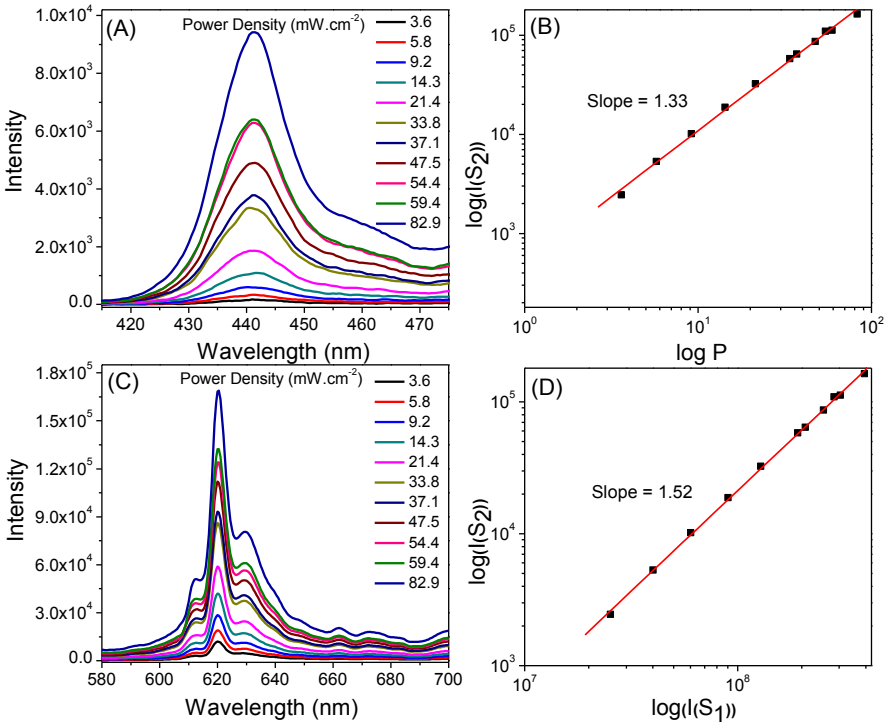

Figure 4.6 (A) Upconverted fluorescence spectrum of ZnTPP loaded ZrO_2 film as a function of incident cw laser power. (B) Double logarithmic plot of the data in (A). (C) S_1 fluorescence. (D) Plot of $\log_{10}$ of S_2 fluorescence intensity versus $\log_{10}$ of prompt S_1 fluorescence intensity as a function of increasing laser power using a 532 nm cw laser and back-face excitation.

These results are significant for two reasons: First, to our knowledge this is the first observation of photon up-conversion by homo-molecular TTA on semiconductor surfaces. Up-conversion through a dual absorber–emitter system has recently been observed on a semiconductor surface by Morandeira's group, through the use of platinum(II) octaethylporphyrin as the absorber/triplet energy donor and 9,10-diphenylanthracene as the triplet energy acceptor/up-converter.[57] Second, homo-molecular TTA is observed on TiO_2, whose conduction band lies below the S_1 energy

level of ZnTPP. Rochford and Gallopini[11] previously reported that electron injection from the S_1 state of a porphyrin to the conduction band of TiO_2 can result in strong quenching of S_1 fluorescence and that use of the wider band gap ZrO_2 as a semiconductor material precluded this quenching by electron injection. Morandeira's group used ZrO_2 as a proxy for TiO_2 based on this reported capability of ZrO_2 to inhibit electron injection from the excited states of the physisorbed dye.[57, 58] Our results indicate that regardless of the band gap energy of the metal oxide used as semiconductor, emission from the S_1 and S_2 state of ZnTPP can be observed.

Clearly, the condition of the metal oxide film strongly affects the overall up-conversion efficiency in these systems, significantly more so than the relative spacing of the metal oxide conduction bands and excited state energies of ZnTPP. In general, the highest up-conversion efficiencies observed in our experiments were from the ZrO_2 films, which is consistent with our initial hypothesis, but given the lack of consistency between samples, this result may well simply be fortuitous and it is likely that there are additional important influences at work. Factors that might reasonably be expected to affect up-conversion efficiency include the metal oxide film thickness, accessible surface area of the constituent nanoparticles for dye binding and the amount of dye loading, but also, and perhaps most important, the overall metal oxide film morphology. When comparing spectral properties between different metal oxides, samples were prepared with as uniform film thickness as possible, and further, the average nanoparticle sizes for the different mixed oxides were similar. Dye loading conditions were controlled rigorously, yet still the strong degree of variability was observed. We believe that one of the most important factors contributing to high up-conversion efficiencies is film morphology.

Atomic force microscope (AFM) images of pure TiO_2 films revealed topographic features on the order of hundreds of nanometers (RMS roughness of *ca.* 330 nm with some peak heights exceeding 2.5 μm for 50 μm x 50μm image; a typical AFM image is shown in Figure A4.8 in the Appendix), while films of pure ZrO_2 exhibited features whose height exceeded the dynamic range of the microscope (>6 μm). It is plausible that the various pits and defects on the metal oxide film surfaces behave as nucleation sites for aggregate formation, and thus, the major contributor to up-conversion.

4.5 Conclusions

Homo-molecular noncoherent photon up-conversion based on triplet–triplet annihilation has been observed, for the first time, on a series of metal oxide films with systematically varied conduction band gap using a zinc porphyrin up-converter. Measurable upconverted emission was found for all metal oxide films, independent of the position of the conduction band gap relative to the relevant energy levels of the MP. The precise intensities, spectral shapes and up-conversion efficiencies of the sensitized metal oxide films was strongly dependent on film preparation conditions, and measurements suggested that the ZnTPP was heavily aggregated on all metal oxide surfaces. Film morphology appears to play an important crucial role in contributing to dye aggregation and hence up-conversion efficiency and controlling this morphology presents a significant challenge in these systems.

CHAPTER 5. SPECTROSCOPIC AND STRUCTURAL STUDIES OF A SURFACE ACTIVE PORPHYRIN IN SOLUTION AND IN LANGMUIR-BLODGETT FILMS

Following the results of Chapter 4, it is recognized that working to control either the photoanode film morphology or the aggregation of the porphyrin on the film's surface will provide a better understanding of the *homo*-NCPU-TTA on semiconductor surfaces. This chapter explores the use of Langmuir-Blodgett (LB) deposition to control the assembly of MPs on solid substrates. For the LB method of film preparation to work, an amphiphilic molecule is required. Since, ZnTPP is not amphiphilic, this chapter also describes the synthetic modification of ZnTPP into a surface active compound which was then assembled into domains with controllable molecular distances and orientations using LB.

This chapter is reprinted with minor revisions from a recent article of the same title published in *Langmuir* **2015**, 31, (50), 13590-13599, © 2015 with permission from American Chemical Society.

The author's contribution in this work include: synthesis of the surface active porphyrin; preparation of Langmuir-Blodgett thin films; collection and interpretation of majority of the data; and preparation of the manuscript. In particular, the author was mainly responsible for collecting H^1-NMR, steady state absorption and emission as well as upconverted emission spectra, and Langmuir isotherms. Dr. Hessamaddin Younesi Araghi performed Brewster Angle Microscopy (BAM) and Atomic Force Microscopy (AFM) measurements while Dr. Neeraj K. Joshi performed Laser Flash Photolysis (LFP), Time-Correlated Single Photon Counting (TCSPC) measurements and also assisted in polarized emission measurements. Dr. Joshi also assisted in data analysis, specifically,

in estimating the excited state population necessary to observe NCPU-TTA in the solid state. The assistance of Dr. Ken Thoms and Dr. Keith Brown of the Saskatchewan Structural Science Center (SSSC) is acknowledged. Dr. Thoms collected mass spectra and performed elemental analysis while Dr. Brown helped interpret H^1-NMR data. Dr. Matthew F. Paige and Dr. Ron P. Steer, as always, provided extensive guidance in planning the experimental work, interpreting results and editing the manuscript prior to publication.

SPECTROSCOPIC AND STRUCTURAL STUDIES OF A SURFACE ACTIVE PORPHYRIN IN SOLUTION AND IN LANGMUIR-BLODGETT FILMS

Concepcion P. Ponce[1,2], Hessamaddin Younesi Araghi[1], Neeraj K. Joshi[1], Ronald P. Steer[1*], Matthew F. Paige[1*]

[1]Department of Chemistry, University of Saskatchewan, 110 Science Place, Saskatoon, Saskatchewan, Canada S7N 5C9

[2]Department of Chemistry, University of the Philippines Visayas, Miag-ao, Iloilo, Philippines 5023

5.1 Abstract

Controlling aggregation of the dual sensitizer-emitter (S-E), zinc tetraphenylporphyrin (ZnTPP), is an important consideration in solid state noncoherent photon up-conversion (NCPU) applications. The Langmuir Blodgett (LB) technique is a facile means of preparing ordered assemblies in thin films to study distance-dependent energy transfer processes in S-E systems and was used in this report to control the aggregation of a functionalized ZnTPP on solid substrates. This was achieved by synthetic addition of a short polar tail to one of the pendant phenyl rings in ZnTPP in order to make it surface active. The surface active ZnTPP derivative formed rigid films at the air-water interface and exhibited mean molecular areas consistent with approximately vertically-oriented molecules under appropriate film compression. A red shift in the UV-Vis spectra as well as unquenched fluorescence emission of the LB films indicated formation of well-ordered aggregates. However, NCPU, present in the solution phase,

was not observed in the LB films suggesting that NCPU from ZnTPP as dual S-E required not just a controlled aggregation but a specific orientation of the molecules with respect to each other.

5.2 Introduction

Natural light-harvesting systems form organized assemblies to achieve efficient energy migration with minimal loss from non-energy transfer quenching processes[120]. Understanding the self-organization of these systems continues to be a major theme in photosynthesis research and is used as a foundation for the design of artificial photosynthetic systems.[120, 121]

Metalloporphyrins (MPs) are of special interest since their structures and spectroscopic properties are similar to those of natural light harvesting systems,[66] a similarity which generated initial interest in this class of molecules as potential sensitizers for dye-sensitized solar cells (DSSCs). However, DSSCs sensitized with MPs give solar energy-to-electricity conversion efficiencies (η) which are significantly lower than those achieved by ruthenium black dyes.[66-68] This has been attributed partly to their propensity to form random aggregates on semiconductor surfaces.[68, 70] While these shortcomings have limited MPs' successful application to DSSCs, recent progress in controlling the hierarchical assembly of light harvesting systems has the potential to change this.[122] Of particular interest is the role of aggregation in noncoherent photon up-conversion (NCPU) processes, which can provide incremental improvements in the efficiency of photovoltaic cells by harvesting under-utilized near infrared solar photons.[15, 71, 72] Details of the mechanism and requirements of NCPU schemes can be found in a number of reviews.[123, 124]

Previous reports from our group have shown that NCPU can take place in MP systems by the photophysical process of homo-molecular triplet-triplet annihilation (TTA) with good efficiency, both in solution and in the solid state.[17, 18] NCPU by homo-molecular TTA involves using the same type of fluorophore (in this case, the MP) to serve as the dual S-E. The up-conversion mechanism in homo-molecular TTA involves photoexcitation of a MP into the S_1, which then undergoes highly efficient intersystem crossing to the T_1 state. The quantum efficiency of T_1 approaches unity, but a small yield of fluorescence from S_1 remains as a direct measure of the absorber power. When two MPs in T_1 are in close proximity, either by initial aggregation or by diffusion, they can undergo TTA to yield one MP in the S_0 state and one in the S_2 state. Upconverted fluorescence is then generated from the subsequent radiative relaxation of the S_2 state.[18]

To fully exploit the potential of MPs in NCPU schemes, a means of controlling their molecular aggregation and spatial orientation on semiconductor surfaces is of utmost importance.[55, 59, 125] Several approaches have been used to control aggregation of MPs in solid state NCPU-TTA, including dispersing the dyes in rigid,[17, 126] rubbery[14] or gel forming polymers;[127] and using covalent assembly[45] and employing supramolecular structures.[128] Dispersing high concentrations of MPs in polyurethanes[14] and gels[127] resulted in observation of NCPU-TTA since these matrices allowed for molecular diffusion and encounter pairs to form. In rigid matrices, such as PMMA[17] and polystyrene,[126] where molecular diffusion can be ruled out, the observation of NCPU-TTA was attributed to strong intermolecular interactions between sensitizer and emitter (S-E) by virtue of their proximity. However, the manner by which the dual S-E MPs aggregate in these matrices and how this affects *homo*-NCPU-TTA efficiency is still unclear. If high MP concentration

alone is sufficient for NCPU-TTA to occur in solid state, high dye loading on metal oxide surfaces should also result in the consistent observation of NCPU-TTA on these surfaces. However, studies on zirconia, titania and mixed zirconia-titania substrates showed lower NCPU-TTA efficiency and reproducibility than those observed in PMMA matrices.[57, 59]

A more systematic way of controlling the rates of S-E triplet-triplet energy transfer has been achieved by the covalent construction of S-E domains with precise distance between S and E, as demonstrated by the ruthenium bipyridine sensitizer and 9,10-diphenylanthracene (DPA) emitter example.[45] However, this approach did not translate to an overall improved NCPU-TTA efficiency due to a less well-controlled intermolecular emitter TTA spacing. Highly efficient NCPU-TTA has been achieved by the use of self-assembled amphiphilic emitters capable of solvophobic interactions with sensitizers in organic media.[128] This approach involved covalent functionalization of the commonly used DPA emitter with solvophobic and solvophilic groups which resulted in a supramolecular assembly of closely-packed DPA arrays with sensitizers bound within a bimodal average distance of 4.8 Å and 17.3 Å from the emitter.[128] In addition, use of a heteromolecular S-E system consisting of carboxylate functionalized Pd(II) mesoporphyrin adsorbed on the surface of $[Zn(adb)(DEF)_2]_n$ metal-organic frameworks (MOF) (adb = 4'4-(anthracene-9,10-diyl)-dibenzoate; DEF = N,N-diethylformamide) resulted in maximization of UC efficiencies under low excitation intensities. This was achieved by fast triplet-triplet energy transfer from the sensitizer to the emitter followed by a fast and long range triplet exciton diffusion in the well-ordered emitter molecules in MOFs.[42] These reports highlight the importance of a high level of assembly of emitter molecules as well as appropriate proximity of S-E pairs for achieving efficient NCPU-TTA.

In systems where the sensitizer and emitter are one and the same, as in the case with ZnTPP,[17, 18, 59] supramolecular control of S-E distances can be achieved through the use of Langmuir and Langmuir-Blodgett (LB) monolayer techniques. LB deposition has been used in the preparation of films to study distance-dependent energy transfer processes in S-E systems such as in J-aggregated cyanine dyes, perylenes and porphyrins.[129-131] The LB method of film preparation typically starts with spreading a monolayer of amphiphilic molecules with long alkyl chains at the air-liquid interface. Controlled compression of the monolayer at the liquid surface results in the formation of assembled domains with tunable molecular distances and orientations which can then be deposited onto solid substrates to produce LB films. Although the most common molecular constructs for MP based S-E systems assembled using the LB method involve dyes functionalized with long alkyl chains, well-behaved monolayers of porphyrin macrocycles with short hydrophilic tails have been reported.[132]

This paper reports a simple approach to control molecular proximity and organization in the well-studied model MP system, zinc(II) tetraphenylporphyrin (ZnTPP), on solid hydrophilic substrates. To enhance the surface activity of ZnTPP, the molecule was derivatized by replacing one pendant phenyl ring with the polar group 4-N-diglycolic acid aminophenyl. This yields a derivative labelled here as ZnDATPP (Figure 5.1) that exhibits photophysics similar to ZnTPP in liquid solution. The polar tail of ZnDATPP interacts strongly with water at the air-water interface, akin to a surface active material, thereby providing a means to exploit the LB technique in preparing well-ordered aggregates in solid thin films.

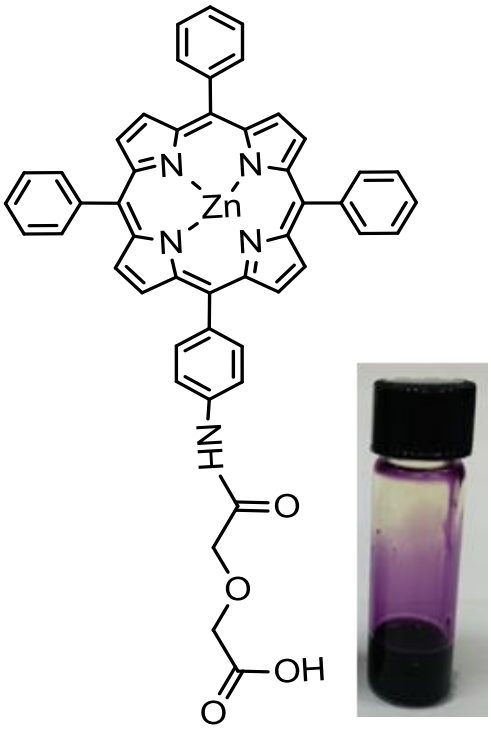

Figure 5.1: Chemical structure and photograph of ZnDATPP in methanol solution.

5.3 Experimental

5.3.1 Synthesis and Solution Preparation

The synthesis and characterization of the surface active porphyrin, 5-(4-N-diglycolic acid aminophenyl)-10,15,20-triphenylporphyrin zinc (II) (ZnDATPP) is described in the succeeding sentences. Commercially available zinc (II) 5-(4-aminophenyl)-10,15,20-triphenylporphyrin (ZnATPP, Frontier Scientific) was used directly without further purification. ZnATPP solution in DMF (0.139 mmol) was added with diglycolic anhydride (0.418 mmol) and the final solution was stirred at room temperature overnight (Figure A5.1-A). The reaction mixture was diluted with 10 mL of $CHCl_3$ then added with hexanes until precipitation occurred. The precipitate was filtered and washed with water to remove residual anhydride, and then dried under vacuum to yield 0.109 g (97%) of ZnDATPP. The reaction was monitored by TLC using EM Science silica gel 60 plates with UV indicator (F-254). Fractions were visualized by the inherent color of the spots. ^{1}H-NMR spectra were obtained on Bruker 500 MHz Avance spectrometer with DMSO-*d* (Cambridge Isotope Laboratories, Inc.) as solvent (see Figure A5.1-B and C in the Appendix for the NMR spectra before and after reaction). Mass spectra were obtained on an Applied Biosystems 4800 QToF instrument using ESI in methanol as the solvent (see Figure A5.1-D for the mass spectra of the product). Electronic absorption spectra were measured on a Cary 6000i UV–Vis spectrophotometer and fluorescence spectra were measured on a PTI quantamaster spectrometer. UV–Vis (CH_3OH) λ_{max}, nm (ε/M^{-1} cm^{-1}): 414 (406,000), 512 (16,900), 547 (9000), 589 (5400), 645 (4100). Anal. Calcd. (%) for $ZnC_{48}H_{33}N_5O_4$ (809.2 g mol^{-1}): C 71.2, H 4.11, N 8.65 Found: C 68.5, H 4.24. N 7.91; MS (ESI) M^{+2} 809.18); ^{1}H-NMR (δ (ppm)): 13.03 (1H), 10.38 (1H), 8.77-8.84 (8H), 8.10-8.25

(10H), 7.78-7.85 (9H), 4.35-4.37 (4H). ^{13}C-NMR (δ (ppm)): 172.11-172.51, 149.71-149.96, 143.23, 141.71, 138.36, 135.02, 134.65, 132.08-132.19, 127.09-127.96, 120.64-120.78, 118.11, 71.15, 68.76

Solutions of ZnDATPP were prepared fresh before each experiment in aerated DMSO-d6 (Cambridge Isotope Laboratories, Inc) for NMR measurements; de-aerated organic solvents methanol or chloroform (Fisher Scientific) for photophysical measurements in solution and in aerated chloroform for Langmuir monolayers characterization.

5.3.2. Langmuir and Langmuir Blodgett Films

Langmuir and LB film preparation was performed using a KSV 2000 Langmuir trough on an ultrapure water subphase (Millipore, resistivity 18 MΩ·cm) operating at a temperature of 21.0± 0.5°C. The subphase was cleaned by suction and cleanliness was verified by running a pure water blank isotherm. For ZnDATPP isotherm measurements, a 150-200 µL aliquot of 400-500 µM ZnDATPP in chloroform was spread on the clean subphase and the spreading solvent was allowed to evaporate for at least 10 minutes prior to film compression. Surface pressure was measured using a Wilhelmy balance equipped with a platinum Wilhelmy plate. The rate of compression for both π-A isotherm measurements and LB film deposition was 10 mm/min. For deposition measurements, films were compressed to π = 20 mN/m and the film was allowed to stabilize for at least 5 minutes before a pre-cleaned 25 x 25 x 0.5 mm quartz substrate (SPI Supplies) was pulled upward through the water-air interface in a single stroke at a rate of 5 mm/min. The transfer ratio for monolayer deposition was close to unity. Cleaning of the quartz substrate

involved a sequence of sonicating the substrates in 1:1 methanol-acetone mixture, drying with N_2 gas, soaking in boiling piranha solution for at least 30 minutes, drying in N_2 gas and finally plasma-cleaning for at least thirty minutes immediately before use.

AFM measurements of the Langmuir and LB films were carried out in tapping mode in air using a Dimension Hybrid Nanoscope system (Bruker). Commercially available silicon AFM probes (Bruker), with spring constant of ~12-103 N/m were used for measurements.

BAM measurements were performed on a KSV-NIMA UltraBAM microscope coupled to a Langmuir trough. The microscope used a 50 mW, 658 nm polarized laser for illumination and a CCD detector (collection rate of 20 frames per second). Lateral resolution of the instrument (Rayleigh criterion) was ~2 μm and the angle of the incident beam to the air-water interface was fixed at the Brewster angle (53.1°).

5.3.3 Spectroscopic Characterization

Steady state absorption and emission spectra, transient absorption, time-resolved emission behavior, and photon up-conversion by triplet-triplet annihilation of the samples were collected using instrumentation described in Chapter 2.

5.4 Results and Discussion

5.4.1 Spectroscopy and photophysical studies in solution

The steady state absorption spectrum of a 1 x 10^{-6} M ZnDATPP in methanol is shown in Figure 5.2A. The spectral profile is similar to that observed for ZnTPP and a number of related porphyrins. It exhibits a strong absorption band at 421.5 nm with a

weak shoulder at 400 nm assigned to the strongly allowed B transition (Soret band) and weak bands at 596.5 and 556.5 nm assigned to the Q(1,0) and Q(0,0) transitions.[11, 18] The fluorescence emission spectra of the same solution excited at 400 nm (Figure 5.2B) show the typical S_2-S_0 emission of MPs at 430 nm and the Q(0,0) and Q(0,1) bands at 600 nm and 650 nm, respectively.[133] To verify that the observed fluorescence is due to the absorbing species of ZnDATPP and not from impurities in the starting material, ZnATPP, a steady state fluorescence excitation measurement was performed. Figure A5.3 presented in the Appendix shows a good overlap between the individually normalized absorption and corrected fluorescence excitation spectra of ZnDATPP in methanol. This supports the assignment of the 430 nm fluorescence emission to that of the S_2-S_0 transition.[133]

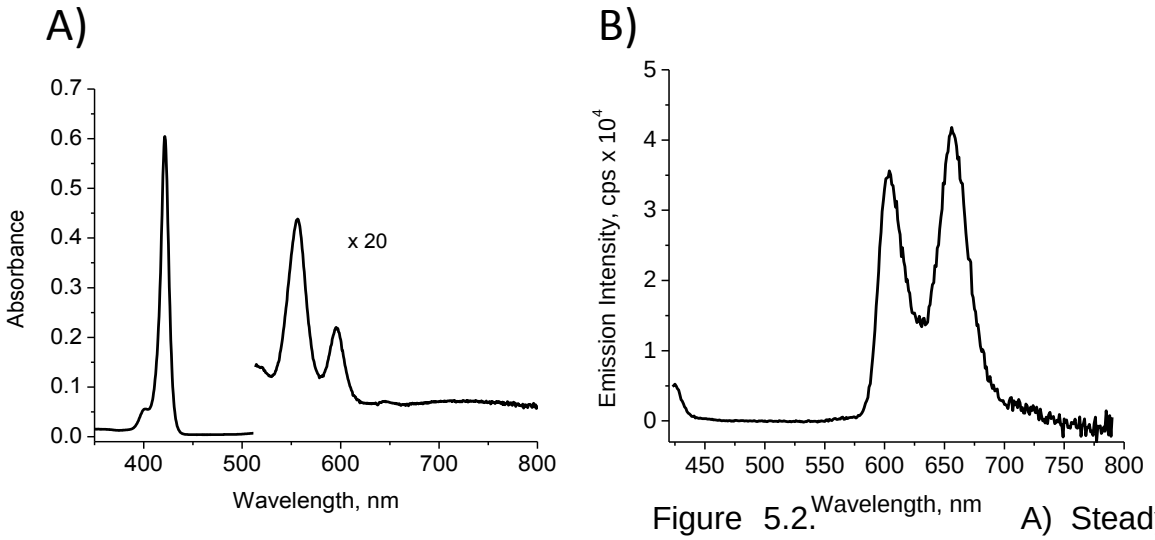

Figure 5.2. A) Steady-state absorption of 1.0 x 10^{-6} M ZnDATPP in methanol showing the B(0,0) peak at 421.5 nm and expanded Q(0,0) and Q(1,0) bands at 595.5nm and 556.5 nm, respectively. (B) Emission spectra of the same sample excited at 405 nm showing the edge of a characteristic S_2 emission of MPs as well as the $S_1 \rightarrow S_0$ bands at 600 nm and 656 nm.

To confirm that ZnDATPP can also act as a dual S-E in NCPU-TTA, methanol solutions were excited with a low power 532-nm cw diode laser and the upconverted emission was collected at wavelengths shorter than that of the excitation light. NCPU-TTA was not observed for dilute solutions (1 x 10^{-6} M) but was readily detected in higher concentrations (i.e. > 5 x 10^{-6} M). This supports the idea that proximity or aggregation of the MPs is necessary for NCPU-TTA to occur.[18] Figure 5.3 shows the dependence of the integrated UC emission intensity on the integrated prompt S_1 intensity, plotted on a double logarithmic scale. The intensity of the prompt S_1 emission can be used to estimate the concentration of the lowest triplet state (T_1) under a variety of excitation conditions using the relation, $I_f(S_1) \propto [T_1]$, because the quantum efficiency of intersystem crossing from S_1 to T_1 of MPs are high (close to unity).[18] The slope of the line in Figure 3 is 1.9 ± 0.1, close

to the expected value of 2.0 for a bimolecular triplet-triplet encounter under low power excitation conditions.[18]

Using laser flash photolysis (LFP) experiments, the lower limit of the probability of formation of the upconverted S_2 state by TTA can be reasonably estimated from the S_1 population and the spin statistical limit of TTA (in the lower limit, only 1/9 of TT encounters will produce S_2). Our result of 0.05 is consistent with the reported value of 0.043 for ZnTPP which was also calculated based on the case where TTA processes predominates over first order and pseudo-first order triplet decay.[48]

Other spectroscopic properties of ZnDATPP collected in Table A1 in the Appendix show no significant difference from those of the model compound, ZnTPP. Thus, we are able to introduce a hydrophilic tail into ZnTPP without drastically altering its spectroscopic properties. Moreover, spectral properties of ZnDATPP in chloroform were also measured to ensure that switching from methanol to chloroform as a solvent for the preparation of Langmuir monolayers did not significantly affect the spectral properties of the molecule. Use of chloroform did not appreciably alter the spectroscopic output of the molecule, with results summarized in Table A1.

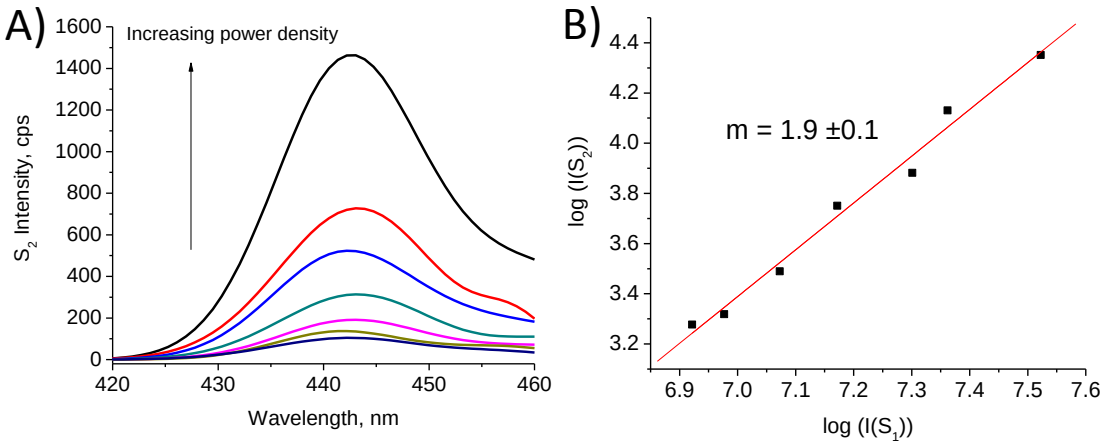

Figure 5.3 A) Upconverted emission intensity as a function of 532 nm diode laser excitation power; laser power ranged from 1.4 mW to 14.4 mW B) Double logarithmic plot of the integrated area under the S_2 fluorescence peak vs. integrated area under the S_1 fluorescence peaks. Integrated areas of emission intensity curves are denoted as $I(S_n)$ in the axis label.

5.4.2 Spectroscopy and structural studies in Langmuir and Langmuir-Blodgett films

The ultimate goal of making surface active ZnDATPP is to provide a means of controlling its molecular organization on hydrophilic surfaces without (or only minimally) changing its light harvesting properties. Hence, spectroscopic and structural characterization of ZnDATPP in Langmuir and LB films were performed.

Figure 5.4 shows a typical π-A isotherm of ZnDATPP spread at the air-water interface. A single compression of the ZnDATPP layer on the water subphase exhibits a reproducible isotherm similar in shape to those of related surface active porphyrin molecules reported elsewhere in the literature.[132, 134-136] The π-A isotherms features a

slow rise of π values from zero to *ca.* 5 $mN \cdot m^{-1}$ corresponding to the expanded monolayer and a steep rise from *ca*. 5 to 50 $mN \cdot m^{-1}$ corresponding to the formation of a condensed phase. Extrapolating the steep rise in the isotherm to zero surface pressure gives the limiting mean molecular area (A_0), the area occupied by one molecule in a close-packed structure, of *ca*. 82 $Å^2$. On the basis of the minimum energy equilibrium geometry of a ZnDATPP molecule calculated in Spartan using molecular mechanics (Merck Molecular Force Field, MMFF) and approximating the structure as a 23 x 16 x 5 Å rectangular block, the expected A_0 if the molecule is lying face-flat on the water subphase is >350 $Å^2$ and <80 $Å^2$ if oriented vertically on the surface (*cf*. Figure 5.4). The measured A_0 is consistent with ZnDATPP molecules oriented polar edge-on in the film, as observed in related meso-tetraphenylporphyrins with one polar group (A_0 values of these molecules are compiled in Table A2, Appendix).[132, 134-136] Tetraphenylporphyrins with all four phenyl groups functionalized with short hydrophilic tails occupy areas smaller than the expected value for edge-on oriented molecules.[134, 137, 138] These small limiting areas were attributed to the formation of crowded monolayers with non-monolayer aggregate regions.

The ZnDATPP Langmuir film exhibits strong hysteresis upon repeated compression-expansion cycles (Figure 5.4). After an initial compression to π = 65 mN/m and subsequent re-expansion, a steep drop to π = 2.5 mN/m in the expansion curve was observed, with the surface pressure changing minimally with continued expansion. The second cycle showed the steep rise in surface pressure occurring at a much lower MMA (starting at 30 $Å^2 \cdot molecule^{-1}$ or a ΔMMA *ca.* -50 $Å^2 \cdot molecule^{-1}$). This indicates either a substantive loss of surfactant below the subphase surface or a stacking of ZnDATPP into multilayers at the maximum expansion. Visual inspection of the Langmuir films after the

first compression-decompression cycle indicated formation of fragmented, needle-like and slab-like structures floating on the water surface (see Figure A5.7, Appendix for photographs of the films). This is consistent with reported rigid floating domains at the air-water interface of porphyrins not stabilized by long alkyl chains[134, 137-139] and can be rationalized by the interplay of factors affecting the ZnDATPP organization at the air-water interface, that is, a competition between hydrophilic interactions and hydrophobic π-stacking interactions.[136] The attraction between the ZnDATPP polar tail and water competes with the π-stacking interactions between neighboring ZnDATPP molecules. Based on the established strong π-stacking interactions of porphyrins, we conclude that this electrostatic interaction is not strong enough to break the porphyrin π-stacks and re-disperse the ZnDATPP molecules at the air-water interface upon repeated compression-decompression cycles as seen in Figure A5.7, Appendix. The stacking of ZnDATPP could be minimized, however, by compressing the films to lower surface pressures before re-expansion. When monolayers were compressed to π = 20 mN/m and subsequently expanded, isotherm hysteresis was minimal, which suggests that the Langmuir layers have good stability at this pressure. Monolayers compressed at rates from 1 mm·min^{-1} – 40 mm·min^{-1} show similar hysteresis profiles with ΔMMA *ca.* -10 Å^2·molecule^{-1} for all compression rates studied (Results for compression rates of 1 and 10 mm·min^{-1} are shown in Figure A5.7-D, Appendix). Repeated compression/decompression of the same Langmuir monolayer while varying the compression rate from 1 mm·min^{-1} – 40 mm·min^{-1} at the end of 2 cycles for each rate show similar lift-off areas at MMA *ca.* 73 Å^2·molecule^{-1} (Figure A7-E, Appendix). These results show that while there is some minimal hysteresis, the Langmuir monolayers form reproducible ordered structures at π = 20 mN/m

independent of compression rates used in this study. Because of this, all LB films were deposited at π = 20 mN/m and at a compression rate of 10 mm·min^{-1}.

To probe the organization of ZnDATPP at the air-water interface, BAM images of films were collected as a function of film compression (Figure 5.5). BAM allows for direct visualization of Langmuir films at the air-water interface, and provides the ability to measure changes in interfacial properties such as anisotropy and film thickness.[140] For these images, the instrumental settings have been adjusted such that water appears as bright (high reflectivity) areas and surface active domains appear as dark (low reflectivity) areas. In Figure 5.5A, isolated dark areas are seen floating on the water subphase before compression. Film compression to π values below the collapse surface pressure (Figure 5.5B-D) resulted in these domains growing larger. Note also the appearance of varying gray levels indicated by arrows in the images in Figure 5.5B-D. These differences in reflectivity suggest a difference in film thickness (i.e. formation of layers thicker than one molecule) or different molecular-level organization of ZnDATPP, which can be a variation in the tilt direction of the molecules. The facets in the domains suggest the films are rigid and crystalline, that is, they are highly ordered aggregates. This is an important observation as the goal of this work is to control aggregation and orientation of the S-E molecules in the solid state. Film compression approaching the collapse surface pressure shows the films are fragmenting, which provides further visual verification of the rigidity of the domains and overlapping of monolayers when π-stacking interactions become dominant.

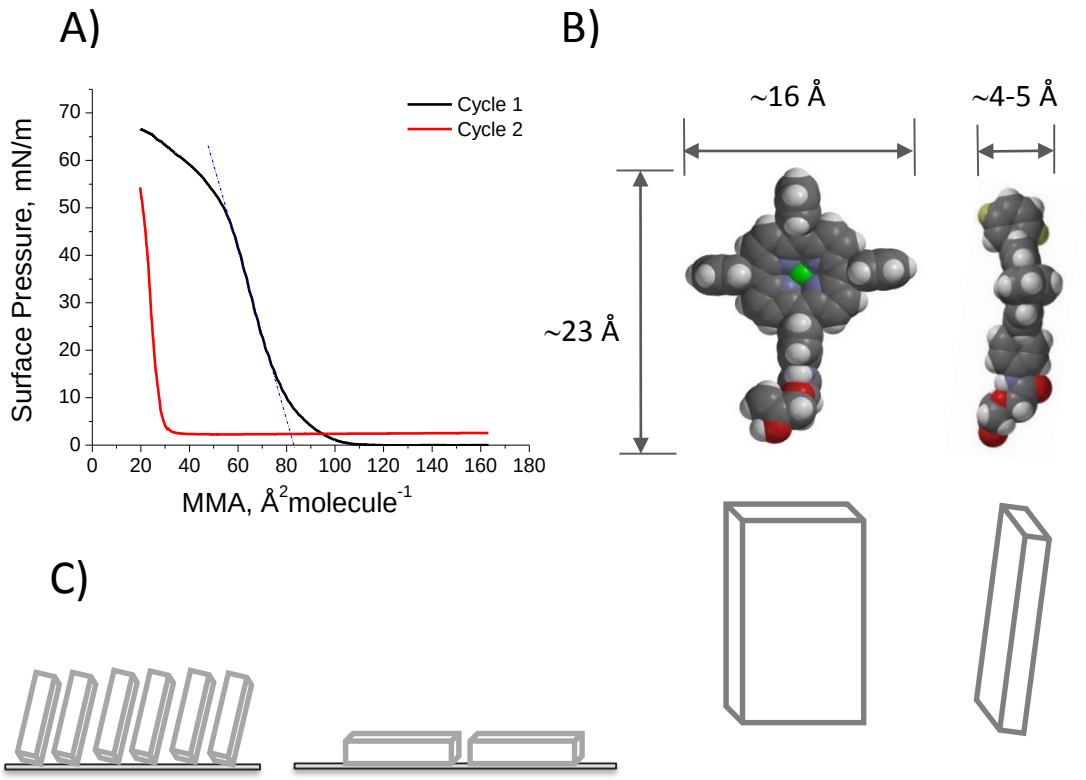

Figure 5.4: A) Surface pressure-area compression isotherms for ZnDATPP on a pure water subphase measured at 21.5°C. The black isotherm is for the initial compression experiment, while the red isotherm is for a second compression of the same film. B) Dimensions of ZnDATPP based on its equilibrium geometry and approximating it as a rectangular block. C) Cartoon diagram of ZnDATPP lying with edge-on (left) and flat face (right) orientations on the water surface.

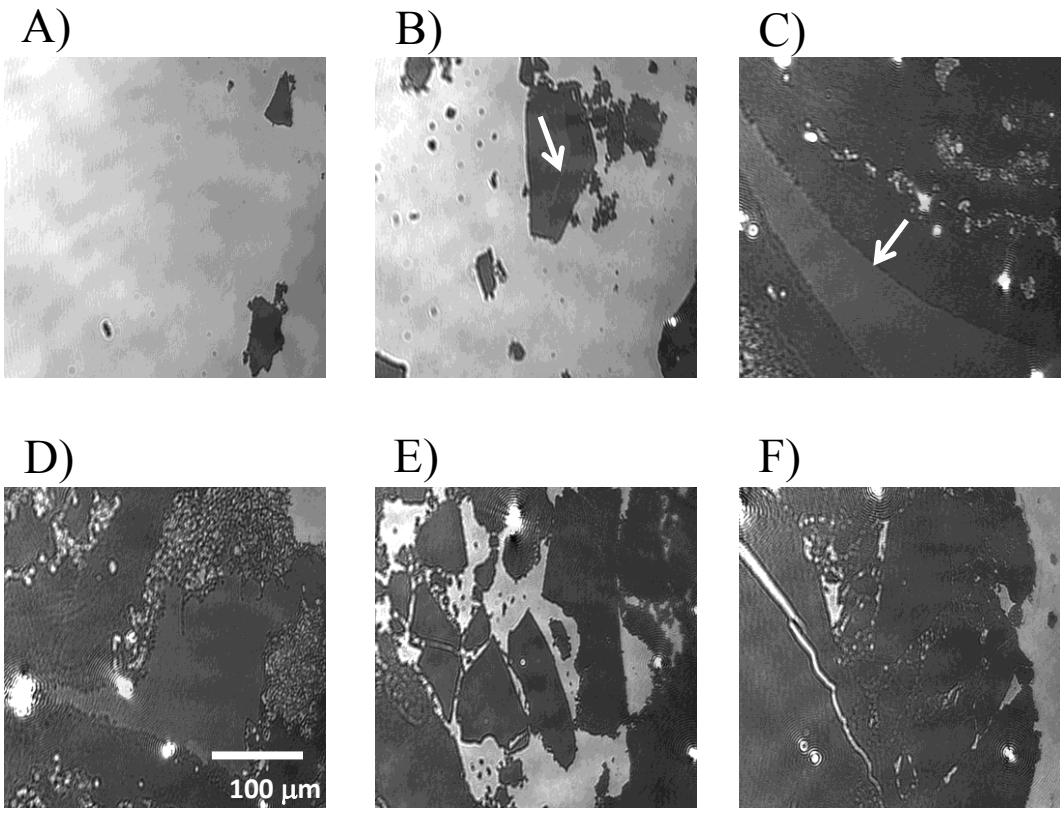

Figure 5.5: Brewster angle microscope images (520 μm × 387 μm) of ZnDATPP film at the air-water interface at 22°C as a function of film compression; A) 0 mN/m; B) 1 mN/m; C) 10 mN/m; D) 20 mN/m; E) 30 mN/m; F) 40 mN/m. Arrows indicate film regions with different reflectivities (gray levels). Scale bar is the same for all images.

BAM allows detection of changes in gross film morphology at the air-water interface but does not provide quantitative measurements at the molecular-scale, so AFM imaging of the resulting LB films was performed to provide this information (Figure 5.6). The LB monolayer films were molecularly flat with RMS roughness of *ca.* 1.6 nm and a skewness > 0 measured for a 400 μm^2 micrograph; films appear colored when viewed against a white background (Figure A5.8 in the Appendix). These data indicate the presence of ZnDATPP

molecules on quartz and led us to conclude that large domains seen with BAM at the air water interface can be transferred to quartz substrates with good efficiency; this is consistent with the unity transfer ratios. The AFM image shown in Figure 5.6 was chosen since it features non-uniformity of the surface, a situation that can arise when brittle films are deposited with gaps between domains. These gaps correspond to the underlying bare quartz substrate and allow determination of the height of tall features in the film without the need for lithography. The average step height from the selected region in the AFM of monolayer films is *ca.* 1.7 nm. The expected height of ZnDATPP molecule oriented vertically on the surface is *ca.* 2.3 nm and *ca.* 0.4 to 0.5 nm if oriented parallel to the surface (Figure 5.4, *vide supra*). The measured average height of *ca.* 1.7 nm implies an average ZnDATPP molecular tilt of *ca.* 44° from the surface normal. This is consistent with those observed for a structurally related thiol-tethered zinc porphyrin whose height on gold surfaces was measured with AFM to be 2.1 nm with a 30-45° tilt.[141] A tilted orientation has also been reported in crystal structures of self-assembling zinc porphyrin derivatives that mimic the natural chlorosomal bacteriochlorophylls.[142] The measured AFM height of ZnDATPP does not eliminate the possibility of more than one molecule thick layers transferred onto the substrate. However, the reproducible limiting MMA values of *ca.* 82 $Å^2 \cdot molecule^{-1}$ discussed above suggests that the grayness variations seen in the BAM domains are ZnDATPP monolayers tilted in different directions. If the domains were more than one molecule thick, the MMA values would be much less than 80 $Å^2 \cdot molecule^{-1}$ as reported in floating films of non-amphiphilic porphyrazines,[143] and of meso-tetraphenyl porphyrins substituted with polar substituents on the phenyl rings.[134, 138, 144]

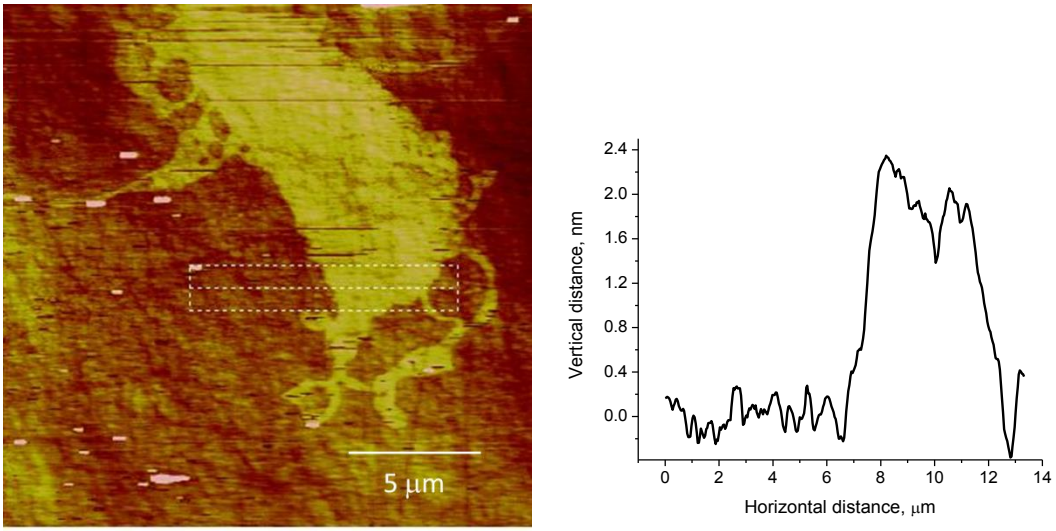

Figure 5.6. Atomic force microscope height images of a ZnDATPP monolayer film and the corresponding average step height of the selected rectangular region. Average step height measured is *ca.* 1.7 nm.

To further confirm that ZnDATPP molecules are organized edge-on at the air-water and air-solid interface with a tilted orientation, we collected emission of ZnDATPP monolayer films excited with a vertically polarized (parallel to the dipping direction) and horizontally polarized (perpendicular to the dipping direction) 532 nm cw diode laser. Figure 5.7 shows the LB films excited with vertically polarized and horizontally polarized light. The peak positions in both spectra are found at 606 and 657 nm. Vertically polarized excitation resulted to a slightly higher peak emission intensity than with horizontally polarized excitation (a difference of 836 cps), qualitatively indicating a small preferential orientation of the transition dipole of the chromophore along the dipping direction. Meso-substituted porphyrins have degenerate transition dipoles, B_x and B_y, set on the lines connecting opposite meso–meso positions, as shown in Figure 5.7.[145] The small variation in the emission intensity with vertically- and horizontally polarized excitation indicates that

the ZnDATPP molecules are neither completely flat nor completely vertical on the substrate, in agreement with the estimated tilt angle of the ZnDATPP molecule on the substrate.

Results of the structural analysis of ZnDATPP at the air-water and air-solid interface point strongly to a tilted edge-on organization. This assembly might reasonably be expected to give the signature absorption spectra of edge to edge stacking (J-aggregates) of MPs. The absorption spectra of the ZnDATPP monolayers transferred to quartz substrates are shown in Figure 5.8. For comparison, the spectrum of ZnDATPP in chloroform is also shown. The spectra of the LB films are significantly broadened and red-shifted 15-22 nm relative to the solution phase. Desorption of the monolayers from the substrate by sonicating in methanol and collecting the absorption spectrum gives the absorption profile of the solution phase. This indicates the changes observed in the absorption spectra are due to specific interactions favouring J-type aggregation and not a consequence of degradation or damage induced by the deposition process.

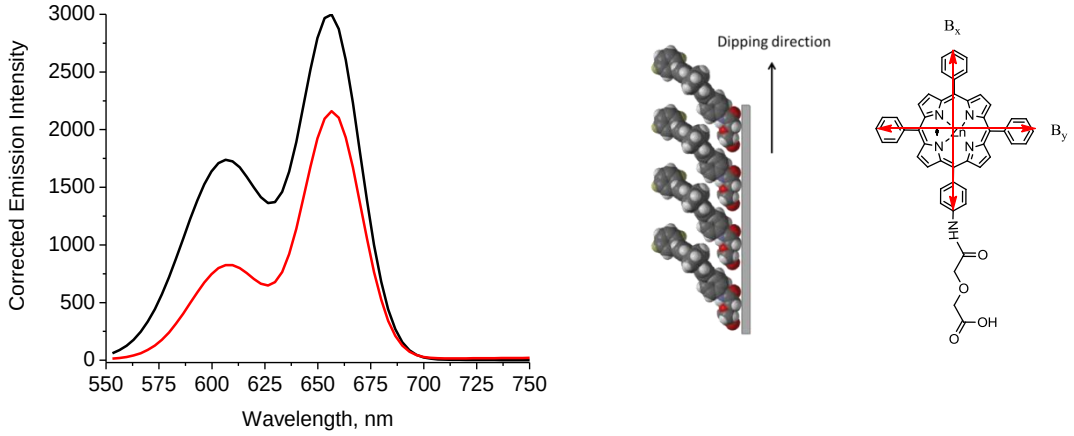

Figure 5.7: Fluorescence anisotropy experiment for ZnDATPP monolayer film on a solid glass substrate; the excitation wavelength was 532 nm; the black curve corresponds to vertically polarized (parallel to the dipping direction) excitation while the red curve corresponds to horizontally polarized excitation (perpendicular to the dipping direction). A schematic illustration of the proposed molecular orientation of ZnDATPP relative to the dipping direction and the transition dipoles (B_x and B_y) is shown to the right.

These observations of a J-aggregate UV-VIS absorption signature and unquenched S_1 emission of ZnDATPP in LB films are encouraging as they suggest that ZnDATPP molecules are arranged in an orderly manner in the films[142, 146] corroborating the earlier interpretation that the floating surface structures are crystalline. Based on published crystal structures of a closely-related porphyrin, the interplanar distance of the porphyrin rings in the solid film are *ca.* 4Å with offset metal centers.[142] The interplanar distance for self-assembled monolayers of thiol-tethered ZnTPP on gold substrate is longer at *ca.* 6Å but is still within a favourable distance for short range energy transfer (1-10Å).[147, 148] Given that ZnDATPP formed well-ordered structures on solid substrates and the intermolecular

distances are at a length-scale that is favourable for short range energy transfer, NCPU-TTA measurements were carried out on ZnDATPP LB films. When the LB film deposition surface pressure was varied (which varied the MMA and consequently the intermolecular distance of the tethered porphyrin on quartz slides), J-aggregate UV-Vis absorption spectra and fluorescence emission anisotropy were observed (Figure S9 in ESI). These spectroscopic characteristics of well-ordered aggregates were also observed when the concentration of the tethered porphyrin deposited on the quartz substrate was increased.

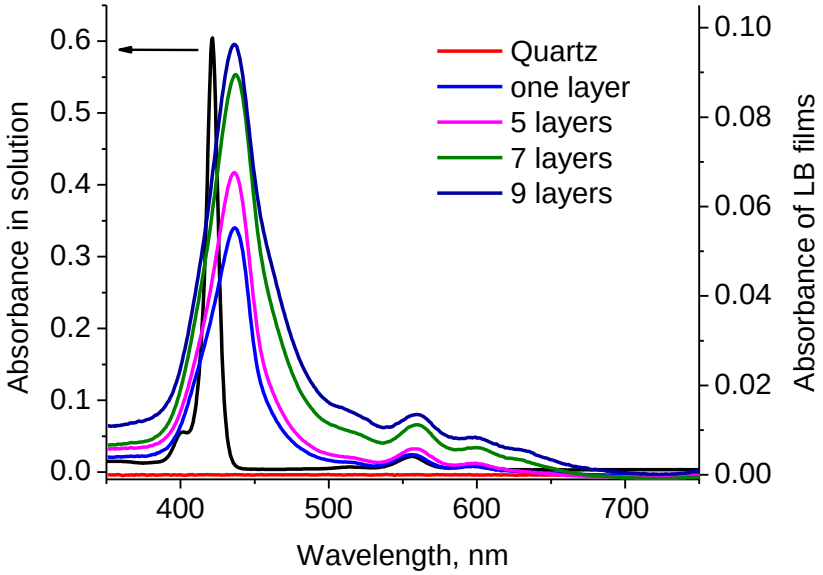

Figure 5.8. Absorption spectra of ZnDATPP monolayers transferred to both sides of a quartz substrate at 20 mN/m. The solution phase spectrum (black curve) is also shown for comparison.

Surprisingly, however, *homo*-NCPU-TTA was not observed in these films. *Homo*-NCPU-TTA in rigid matrices requires pre-aggregation of the active molecules to allow exciton migration through the aggregates and at the same time provide molecular orbital overlap distances for TTA to occur.[17, 59] Previous results on *homo*-NCPU-TTA in the solid state using ZnTPP or its derivatives as dual S-Es show that the molecules must be pre-aggregated and their close proximity is crucial.[17] The results presented in our study show the formation of well-ordered aggregates that should satisfy the aggregation requirement of NCPU-TTA and begs the question “Why was NCPU-TTA not observed?”. Insufficient exciton density in the multi-layered LB films ($n \geq 10$) can be ruled out as the cause. Calculations based on simple absorbing disk/cylinder models (details given in ESI) show that the numbers of initially excited molecules for a particular incident photon power density are comparable for both multi-layer LB films and a solution of $5x10^{-6}$ M concentration in which TTA would be observed. Thus, the non-occurrence of NCPU-TTA in ZnDATPP well-ordered aggregates indicates that aggregation alone is insufficient to support NCPU-TTA.

It is acknowledged that several additional possible effects that might contribute to the lack of observed NCPU that are experimentally very difficult to rule out. Should the triplet lifetime of photoexcited ZnDATPP be significantly shortened in the solid-state films in comparison with the fluid solution systems, then there would be insufficient time for triplet-triplet encounter pairs to form and annihilate, with the end result being negligible up-conversion signal. A second possibility is the formation of triplet excimers, which might have a similar effect. However, measurements of triplet decay dynamics in thin films at room temperature are extraordinarily difficult; we were unable to measure appreciable

triplet decay signals using an appropriate laser flash photolysis instrument, and beam-induced damage in the samples was substantial. Further, the (phosphorescence) emission resulting from excimer formation would be observed in the near-infrared for these compounds, and the low quantum efficiency of most photomultiplier tubes in this spectral region make detection of this effect extremely challenging. At this point, we cannot entirely rule-out these possibilities because of the experimental difficulties involved, though we will continue to pursue these measurements in the future.

Following these results, it is believed that specific distance and orientation of ZnDATPP molecules with respect to each other are both important and influence the TTA process. Orientation effects on singlet energy transfer in porphyrinic artificial light harvesting systems have been reported but orientation effects on triplet-triplet energy transfer (TTET) and particularly TTA are less well-explored.[62] Scholes reviewed key concepts underlying resonance energy transfer (RET) including TTET and summarized that the efficiency of TTET depends on the degree of orbital overlap between S-E and that TT coupling is highly sensitive to molecular shape, size and orientation.[41] Scholes has further demonstrated that such energy transfers in aggregates can behave very differently from those in individual S-E pairs. The S-E molecular architectures presented in the literature are diverse and the orientations that gave rise to ET are equally varied. For example, an anthracene-porphyrin system, where anthracenes are bound to the porphyrin both in the axial and peripheral positions, only the peripheral anthracene exhibited ET to the porphyrin.[60] In another study employing an Fe(III)TPP sharing a phenyl group with its free base analogue, minimum energy transfer rates occur when the porphyrin rings are tilted 45° relative to each other.[62] Further, cofacial bisporphyrins held

by a carbazoyl spacer exhibited slower ET rates when the porphyrin planes are slipped.[61] Considering that the ZnDATPP molecules also exhibit slipped-edge J-aggregation, this may account for the non-occurrence of NCPU-TTA in these LB films. Recall that in randomly-aggregated ZnTPP on metal oxide surfaces, low efficiency NCPU-TTA was observed.[59] From this, it can be inferred that only a fraction of those random aggregates were in the specific orientation necessary for NCPU-TTA to occur. In light of the importance of understanding specific orientation(s) of S-E required for *homo*-NCPU-TTA, developing or adopting strategies that control precisely the mutual orientation of S-E molecules will be useful. While we are not yet at the point of being able to identify precisely what orientations and separations are required for successful NCPU-TTA, their importance is clear and further research efforts on this topic, both experimental and theoretical, are necessary and will continue in the future.

5.5 Conclusions

We have demonstrated that the surface active metalloporphyrin ZnDATPP forms rigid, close-packed films at the air-water interface and exhibits mean molecular areas consistent with nearly vertically-oriented molecules under appropriate film compression. ZnDATPP LB films exhibited red shifted Soret and Q absorption bands as well as unquenched fluorescence emission which characterize formation of well-ordered J-aggregates and satisfy the S-E close proximity requirement of NCPU-TTA. The non-occurrence of NCPU-TTA in well-ordered ZnDATPP aggregates suggests that both appropriate spatial separation and orientation of chromophores are necessary requirements for efficient *homo*-NCPU-TTA, though the exact separation and orientation needed currently remains unclear. Controlled aggregation and intermolecular orientation

are important and developing strategies that control precisely the mutual orientation of S-E molecules will be useful to optimize of NCPU-TTA based energy harvesting schemes.

CHAPTER 6. METAL-METALLOPORPHYRIN FRAMEWORKS AS POTENTIAL MATERIALS FOR NONCOHERENT PHOTON UP-CONVERSION BY TRIPLET-TRIPLET ANNIHILATION

Following the conclusions of Chapter 5, it is recognized that appropriate molecular separation and orientation are necessary for efficient *homo*-NCPU-TTA. This chapter is an unpublished work that describes the use of reticular synthesis to precisely control the intermolecular distance and mutual orientation of metalloporphyrins (MPs) in the solid state. Reticular synthesis refers to the process of judiciously building ordered networks from molecules that are held together by strong bonds. This has been successfully applied by Mahato *et al*. [42] in preparing well-ordered networks of a benchmark heteromolecular NCPU-TTA emitter molecule. Thus, the strategy is adapted to prepare well-ordered networks of a model dual sensitizer-emitter dye.

The author's contribution in this work include: synthesis of powders of metal-metalloporphyrin frameworks (MMPFs) labeled as ZMPB and ZMP; preparation of ZMPB films using the layer-by-layer deposition; collection and interpretation of the majority of the data; and writing the text. In particular, the author was mainly responsible for collecting the steady state absorption and emission as well as upconverted emission spectra of ZMPB and ZMP. Dr. Neeraj K. Joshi assisted in the steady state absorption and emission as well as upconverted emission measurements for ZMP. The assistance of John Hayes and Cheng Lu (University of Toronto) for pXRD data collection is also acknowledged. Dr. Matthew F. Paige and Dr. Ron P. Steer, as always, provided extensive guidance in planning the experimental work, interpreting results and editing the text prior to submission of this thesis.

6.1 Abstract

The efficiency of Dexter electron transfer (ET) in *homo*-NCPU-TTA is affected by molecular separation and orientation. In searching for the appropriate distance and orientation for efficient *homo*-NCPU-TTA, the reticular synthesis strategy was used. This involves judicious building of ordered networks from molecular building blocks that are held together by strong bonds and has been employed successfully in building metal organic frameworks (MOFs) containing emitter molecules commonly used in heteromolecular NCPU-TTA. In this work, tetrakis-(4-carboxyphenyl)porphyrin zinc (II) (ZnTCPP) was used as the MP ligand because it is known to exhibit *homo*-NCPU-TTA and carboxyl-functionalized porphyrins are well studied ligands in porphyrin-based MOFs (MMPFs). Preliminary results showed upconverted emission from one of the MMPFs even in aerated conditions.

6.2 Introduction

One of the major parasitic losses affecting efficiencies of all solar photovoltaics (PVs) is called sub-bandgap loss, which depends on the absorption threshold of the PV. Photons with energies below the PV's absorption threshold do not provide sufficient energy for the generation of electron–hole pairs or excitation of sensitizer dyes. Approaches such as exciton splitting[84] and non-coherent photon up-conversion (NCPU),[25, 85] hold promise of circumventing the theoretical power conversion efficiency limit (*ca*. 34% for single threshold devices such as those based on silicon semiconductors). NCPU recovers transmission losses by converting low-energy photons that are not absorbed into usable high-energy photons.

The more frequently employed NCPU scheme is based on a sensitized process involving two organic components (heteromolecular) – the sensitizer and emitter (S-E).[14] The sensitizer dye strongly absorbs red and near infrared solar photons and produces triplet states in high yield. Triplet-triplet energy transfer (TTET) from the sensitizer dye to the emitter can then occur with high efficiency if the concentration of the emitter is sufficiently large. When two triplet state emitter molecules are in close proximity, either by initial aggregation or by diffusion, they can undergo triplet-triplet annihilation (TTA). This yields a higher energy excited singlet state and one ground singlet state. The upconverted fluorescence from the emitter excited singlet state can then be used to augment the incident photon flux of a conventional PV, thus, improving the overall power conversion efficiency.[86-88]

One important aspect of TTET is that it is forbidden by the dipole-dipole mechanism and can only occur via electron exchange mechanism, which is a short-range energy transfer (Dexter ET). For this reason, control of S-E distances is crucial in NCPU-TTA studies especially in solids where diffusional collision is limited or entirely absent.[42, 128, 149] Mixing the sensitizer with a large amount of emitter molecules in polymers ensured S-E molecules were within Dexter ET distances.[17, 150] However, the random aggregation of chromophores limited the UC efficiency in these systems.

The importance of a high level of assembly of emitter molecules as well as appropriate proximity of S-E pairs for achieving efficient NCPU-TTA has been highlighted in recent studies. Ogawa *et al*. demonstrated highly efficient NCPU-TTA by using a supramolecular assembly of closely-packed arrays of emitters (specifically, functionalized diphenylanthracene, DPA) molecules.[128] However, this approach required an elaborate

functionalization of the emitter molecules with lipophilic groups in order to promote supramolecular assembly. Mahato *et al*. have demonstrated a simpler "reticular synthesis" approach[150] to control the intermolecular distance and mutual orientation of DPA molecules.[42, 151] Reticular synthesis is described as the process of judicious building of ordered networks from molecular building blocks that are held together by strong bonds.[151] This approach has been used to synthesize metal-organic frameworks (MOFs) that incorporate a number of light harvesting and energy transfer molecules.[152-154] Incorporation of porphyrins and their metallated derivatives in MOFs have gained special interest because of their structural similarity to natural light harvesting systems. Despite the field being in its infancy, a number of porphyrin based MOFs have been prepared and studied as reported in a recent review by Gao *et al.*[155]

The first report on employing reticular synthesis for incorporating NCPU-TTA chromophores in MOFs has been presented by Mahato *et al.*[42] The up-converting (MOFs) were built using zinc ions as nodes, 9,10-dibenzoic acid-functionalized DPA (called ADB in Ref. 44) as ligands, and 4,4'-bipyridine (bpy) or 1,4-diazabicyclo[2,2,2]-octane (dabco) as pillars.[42] The result was precise control of intermolecular distance and mutual orientation of up-converting ADB molecules within the MOF. It is worth noting that while all three MOFs prepared contained ADB units with intermolecular distances that were appropriate for Dexter ET, only one arrangement led to high UC efficiency. This arrangement (labeled MOF 3 in Ref. 44) is formed by one dimensional chains of Zn(II)-ADB that are not interpenetrated and where ADB are aligned almost co-facially in the layered structure (see Figure 6.1 for ADB layer arrangements as approximated from

descriptions in Ref. 44).[42] This observation highlights the importance of understanding the molecular orientation required for efficient NCPU-TTA.

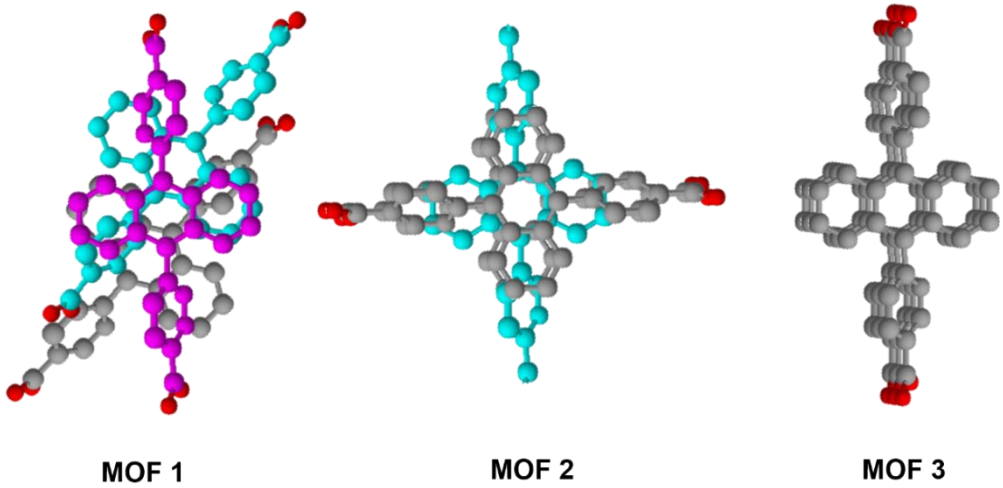

Figure 6.1. Approximate arrangements of the ADB ligand in MOFs 1, 2 and 3 based on descriptions and crystal structures in Ref. 44. The scheme of representing interpenetrated networks with different colors is adapted here.[42] Only the relative positions of the ADB ligand in layers are shown.

Determining the molecular orientation required for efficient NCPU-TTA is also crucial for the homo-molecular scheme where one organic component acts as both sensitizer and emitter. [17, 18, 149] For this scheme, closed-shell metalloporphyrins (MPs) are used as model systems as they are known to exhibit the properties required for such a dual sensitization/upconverted emission function.[17, 18, 48] It has been shown in Chapter 5 that the slipped-edge arrangement of zinc porphyrins in solid state did not result to NCPU-TTA. This led to the hypothesis that NCPU-TTA from ZnTPP as dual S-E required not just an ordered assembly but a specific orientation of the molecules with respect to each other.

To create MPs that adapt other orientations other than slipped-edged, we have adapted the reticular synthesis strategy to synthesize metal-metalloporphyrin frameworks (MMPFs) that are then tested as potential *homo*-NCPU-TTA dual S-E. We choose tetrakis-(4-carboxyphenyl)porphyrin zinc (II) as the MP ligand for the following reasons: 1) fluid solutions of this compound are known to exhibit *homo*-NCPU-TTA[156]; 2) carboxyl-functionalized porphyrins are well studied ligands in porphyrin based MOFs (see review by Gao *et al*.).[155] Zinc metal ions are chosen as nodes to eliminate MLCT or LMCT complications in studying the photophysics of the resulting MMPFs. Bipyridine molecules are chosen as pillaring ligands since they are known to strongly coordinate with both zinc metal nodes and zinc porphyrin centers. This was shown to create an ABBA structural pattern where 2D porphyrin layers are connected by alternating zinc porphyrin center to zinc porphyrin center plus a zinc node to zinc node pillaring (AB) and zinc node to zinc node pillaring (BB) as represented in the schematic diagram in Figure 6.2A.[157] The BB pillaring pattern is commonly observed when a BPY pillar connects two $M_2(COO)_4$, where M is a four-coordinate metal, secondary building units (SBUs) in MOFs. Molecular pillars in MOFs or MMPFs were used to control distances between layers in the 2-dimensional structure of crystals. MMPFs from zinc metal ions and ZnTCPP were also prepared to see the effect of this pillaring on the photophysics of the prepared MMPFs. The absence of the bipyridine pillar in ZMP is expected to produce crystals with smaller interlayer distances.

To incorporate MMPFs into the solid state, two approaches have been taken in this thesis. The first approach is to prepare thin films of MMPFs using layer-by-layer (LBL) growth. This is potentially useful from the point of view of practical applications as thin

solid films can potentially be incorporated into PV devices. Second, bulk powder MMPFs were also prepared. While easier to characterize than thin films, bulk powders are more challenging to incorporate into PV devices. However, this might reasonably be accomplished by dispersing MMPF powders in a thin polymer matrix. It was deemed worthwhile to attempt both approaches.

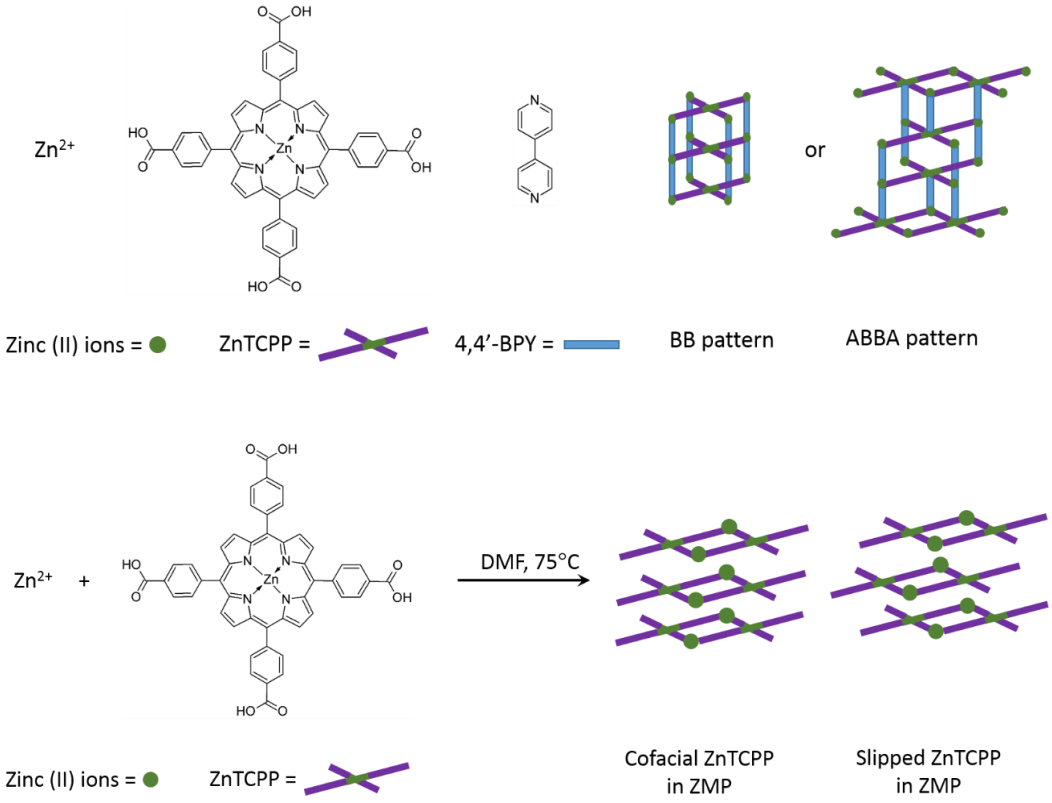

Figure 6.2 A). Chemical structures of the building blocks used and a schematic illustration of the possible arrangements of the units in ZMPB frameworks. B) Possible arrangement of SBUs in ZMP crystals.

The LBL approach is based on the sequential immersion of functionalized surfaces into solutions of MMPF building blocks, i.e., the metal ion nodes and the organic ligands. LBL was first reported for the deposition of multilayers of polyelectrolytes.[158] It's use in

growing MOFs on surfaces was first demonstrated for HKUST-1 ($[Cu_3(btc)_2 \cdot (H_2O)_x]$; btc=benzenetricarboxylate) grown on self-assembled monolayers/gold substrates.[159] Recently, it was used to grow light harvesting MOFs on TiO_2 surfaces[160] and amine-functionalized indium-tin oxide (ITO)[161] substrates. LBL offers the advantage of direct functionalization of substrates and of forming MMPF films with oriented growth and adjustable thickness.[161] A potential disadvantage of LBL approach in growing dual S-E MMPFs is the requirement of growing a large number of MMPF layers on the substrates in order to achieve the required exciton concentration for efficient NCPU-TTA. Nonetheless, this approach was seen as potentially useful for preparing up-converting, solid-state films and thus, the method was attempted.

6.3 Experimental

6.3.1 Synthesis of Metal-Metalloporphyrin Frameworks with and without pillars

All chemical reagents were purchased commercially and used as received without further purification. N,N-dimethylformamide (DMF) was stored over dried molecular sieves (4Å).

The synthesis of a bipyridine-pillared Zn-ZnTCPP (ZMPB) framework followed established solvothermal methods described in literature but using Zn^{2+} ions as the metal nodes, 5,10,15,20-(4-carboxyphenyl) porphyrin zinc (II) (ZnTCPP, Frontier Scientific) as ligands and 4,4-bypiridine (Alfa Aesar) as pillars.[151, 153] ZnTCPP (30 mg) was dissolved in 1 mL DMF (Fisher) and then mixed with 70 mg of $Zn(NO_3)_2 \cdot 6H_2O$ (Alfa-Aesar). The vial was sonicated for 5 min, capped and placed in a 75°C-oven for 2 h. The ZMPB pillar, 4'4-bipyridine (22 mg), was added while the solution was still warm. The sample was then

sonicated for a minute and mixed with 1 mL of a 0.03 M solution of HNO_3 in EtOH. The sample vial was capped and returned to a 75°C-oven. The ZMPB crystals were allowed to grow at this temperature for at least 24 hours. The samples were then cooled to room temperature and the crystals separated by centrifugation. The solvent was decanted and the crystals re-dispersed in *ca.* 1 mL fresh DMF. This process was repeated until the DMF was colorless. The purple crystals were then dried in a 75 °C oven for 24 h. A similar synthesis was carried out but without adding the 4'4-bipyridine pillar to get Zn-ZnTCPP (ZMP) framework.

6.3.2 Layer by Layer (LBL) Assembly of ZMPB Framework

ZMPB frameworks were directly deposited on glass substrates using LBL growth following a slightly modified procedure outlined by So *et al.*[161] First, glass (VWR) substrates were cleaned using a sequence of sonicating the substrates in 1:1 methanol-acetone mixture, drying with N_2 gas, soaking in boiling piranha solution for at least 30 minutes (caution: *corrosive and reacts violently with organic materials*), rinsing with copious amount of distilled and deionized water, drying in N_2 gas and finally plasma-cleaning for at least thirty minutes immediately before use. The substrates were then functionalized with 3-aminopropyltrimethoxysilane (3-APTMS) by refluxing in a 1:100 (v:v) solution of 3-APTMS in octanol for 30 minutes, followed by rinsing with hexanes, rinsing with water, and oven drying (60°C) overnight. The APTMS functionalized substrates were sequentially immersed in ethanolic solutions of zinc (II) acetate (0.1 mM), ZnTCPP (10 μM), 4,4'-bipyridine (10 μM) for 10 minutes. The substrates were rinsed in ethanol in between dipping solutions to remove loosely bound material.

6.3.3. Optical Spectroscopy

Absorption spectra were recorded with a Varian Cary 6000i UV-Vis spectrometer and steady state fluorescence measurements were made using a PTI Quantamaster spectrofluorometer. NCPU-TTA was monitored using a modified Jobin-Yvon Spex Fluorolog spectrofluorometer equipped with a double grating monochromator and a cooled single-photon-counting detector on the emission side. The emission measurements were made in the front face geometry with the excitation beam intercepting the sample at ~32°, which is less than the critical angle of incidence. Residual excitation light was removed by adding an NF533-17 (Thorlabs) notch filter before the emission monochromator.[17] LBL films on glass substrates or ZMPB in PMMA polymer films were mounted as the front window on a triangular brass cell, with the sample facing the inner, evacuable side of the cell when connected to a grease-free high-vacuum line. These film samples were degassed under vacuum for at least 30 minutes, down to a pressure < 5 milliTorr, prior to measurements.

6.4 Results and Discussion

ZMPB was grown on glass substrates using sequential immersion in ethanolic solutions of $Zn(NO_3)_2$, ZnTCPP and 4,4-bipyridine to form ZMPB LBL films. Growth of ZMPB films on glass was monitored by taking UV-Vis absorption spectra after 3, 5, 10, 18 and 30 dipping cycles (layer deposition). As shown in Figure 6.3, the absorption intensity increased as the number of dipping cycles (layers) was increased. Plotting absorption intensity at λ_{max} = 412 nm against the number of layers yielded a straight line with an R^2 value of 0.99. This demonstrates that each dipping cycle deposited approximately equal amounts of ZnTCPP on the substrate. As noted in section 6.2, these

films are believed to form BB or ABBA patterns (Figure 6.2A). The BB stacking pattern results in co-facially stacked (H-aggregated) ZnTCPP in the MOF interlayers. Porphyrin H-aggregates have characteristic UV-absorption features and can be used as an indirect assessment of the manner of MP aggregation in solid thin films. The UV-Vis spectra of LBL assembled ZMPB films is shown in Figure 6.3. The center of the Soret band is at 412 nm, which is blue-shifted by 14 nm relative to that of the solution (centered at 426 nm). Moreover, the Q(1,0) and Q(0,0) bands are red-shifted by *ca.* 10 nm, from 555 nm to 565 nm and 595 nm to 605 nm, respectively. All these spectral shifts relative to the solution absorption spectra are signatures of face-to-face stacking in porphyrins, thus, it can be inferred that the building blocks in ZMPB LBL films formed BB pattern and that ZnTCPP struts are co-facially stacked.[53]

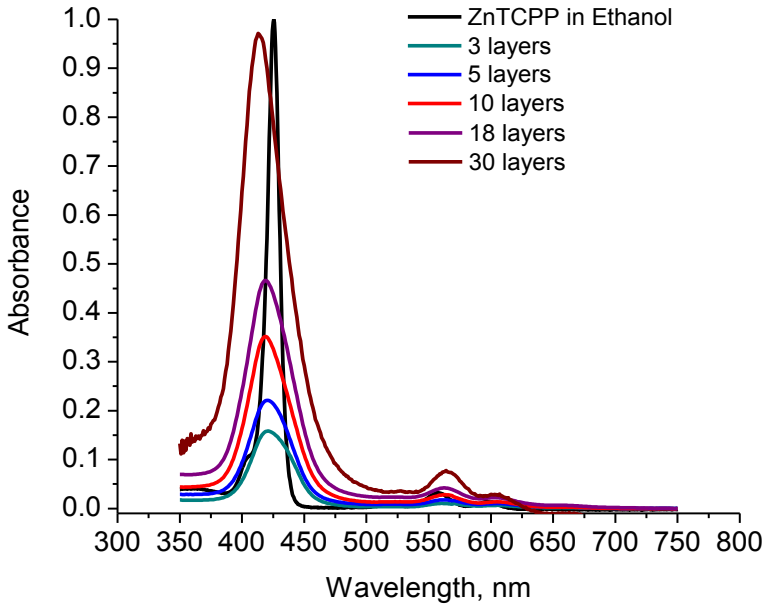

Figure 6.3. LBL assembly of ZMPB thin films monitored by UV-Vis absorption.

Figure 6.4 shows the corrected prompt emission spectra of ZMPB LBL films when excited with a 405 nm laser diode. The APTMS-treated substrate showed interfering emission peaks at the regions of interest, which substantially obscured the emission from ZMPB (see Figure A6.2). To correct for this effect, the APTMS emission spectrum was modeled as a sum of multiple Gaussian peaks and the ZMPB emission spectrum was extracted from the deconvoluted data.

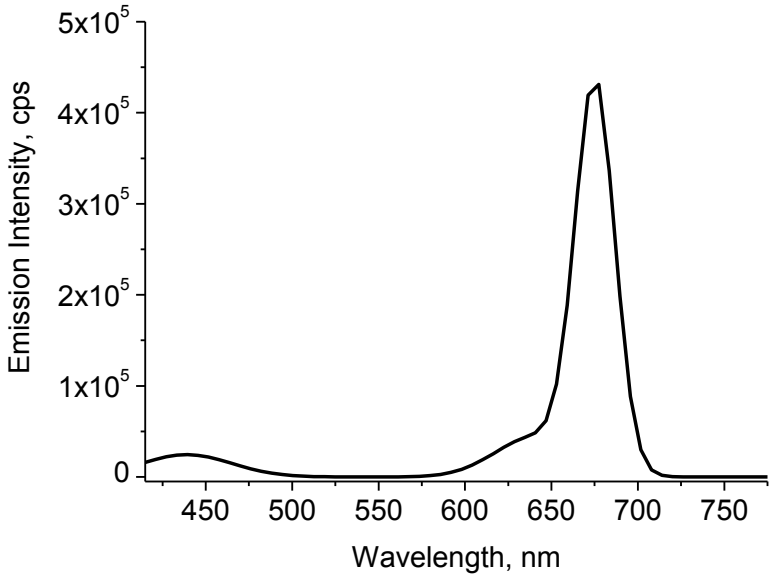

Figure 6.4. Emission spectrum of 35 layers of ZMPB excited at 405 nm. The spectrum was corrected for emission of APTMS by fitting the curve with multiple Gaussians and subtracting the peaks ascribed to APTMS. (See Appendix A6.2 for the raw data).

The resulting corrected emission spectrum (Figure 6.4) showed the following spectral features: 1) a weak and broadened peak at 440 nm; 2) a weak shoulder peak at 620 nm; and 3) a strong emission peak at 675 nm. Emission peaks at 430-450 nm are often attributed to MPs' Soret emission bands.[48, 77, 97] However, because of the

deconvolution process performed to recover the emission spectra of ZMPB, results presented in this study are not definitive. Nevertheless, it is worth noting that a peak at 433 nm in the uncorrected ZMPB emission spectra (indicated by an arrow in Figure A6.2) appears distinct from that of APTMS glass emission and can definitively be assigned to the ZnTCPP struts of ZMPB. Exciting ZMPB on APTMS glass with a 532 nm diode laser showed similar Q band spectral characteristics as with 405 nm excitation – a weak 620 nm shoulder and intense 675 nm peak. The Q band emission peaks of ZnTCPP in methanol solution are centered at *ca.* 605 nm and 655 nm with the 605 nm band slightly lower in intensity than the 655 nm band.[156] The observed values of 620 nm and 675 nm are 15-20 nm red-shifted relative to the solution spectra. Moreover, the 675 nm peak is *ca.* 13 times more intense than the 620 nm peak. The red-shift from 655 nm to 675 nm in emission peak is similar to a reported spectral shift (650 nm to 670 nm) for H-aggregate formation of H_2TCPP^{4-} in surfactant solutions.[52]

Attempts to measure upconverted S_2 emission from a 532-nm excited ZMPB thin film (35 layers) were unsuccessful, with spectra showing only background. This is likely because of an insufficient number of absorbers in the excitation region. Previous measurements of NCPU-TTA from ZnTPP and its derivatives in solution requires *ca.* 5 x 10^{-6} M solution or roughly 1 x 10^{13} molecules in a cylindrical excitation path of 0.1 cm radius and 0.5 cm length. Keeping the same number of molecules and radius of the excitation path and approximating the size of ZMPB molecule as 1.6 nm x 1.6 nm x 1.2 nm, indicates that to achieve a measurable signal, a film thickness of *ca.* 58 nm is required. So *et al.* measured the film thickness of 120 layers of a related MMPF film and gave the value of 50 nm. Thus, *ca.* 120 dipping cycles would be required for ZMPB films

to have the necessary chromophore concentration for NCPU-TTA. Given the amount of time needed to deposit this number of layers, LBL assembly was deemed impractical for real device applications, and the remainder of our efforts focused on preparation of powder-based MMPFs.

ZMPB and ZMP (which has no bipyridine pillars) MMPFs were synthesized using the solvothermal approach and the resulting materials were embedded in a polymer film matrix (see Figure 6.2 for the schematic diagram of ZMP in comparison to ZMPB). The solvothermal synthesis formed crystalline ZMPB and ZMP powders as indicated by sharp and distinct peaks in the pXRD profile shown in Figure 6.5 below. Peaks and the corresponding d-spacing values (d, in Å) extracted from the ZMPB and ZMP pXRD profile as shown, respectively, in Figure A6.5 and A6.6 are listed in Table A6.2 and A6.3 in the Appendix. The pXRD pattern for ZMPB agrees well with published pXRD results of a pillared MMPF formed from the same building blocks but synthesized using a different solvent (the authors used a mixed DMF-ethanol solvent instead of pure DMF used in this work).[157] The pXRD patterns show peaks at 2θ = 5.33°-5.39° in both powders, which corresponds to a distance of 1.67 nm. This agrees well with the 1.65 nm size of ZnTCPP. The intense peak in the ZMP powder pattern at 2θ = 18.2° corresponding to a distance of 0.486 nm is consistent with the interlayer distance of 0.451 nm in non-pillared H_2TCPP nanosheets as reported in literature.[162, 163] The peaks at 2θ values ranging from 9.37°-11.1° corresponding to distances 7.94 to 9.43 Å appearing in ZMPB but not in ZMP are consistent with BPY pillaring (N to N distance of BPY is 7.5 Å and Zn-N distance is *ca.* 2 Å). The presence of unaccounted peaks in both crystals is likely due to unreacted starting material and solvent impurities. Nevertheless, the patterns contain the peaks expected

for the corresponding MMPF structure and clearly indicate formation of the desired product. To further purify the products, the difference in solubility of MMPFs (insoluble) and starting materials (soluble) in most solvents was exploited by repeatedly washing the powders in fresh DMF.

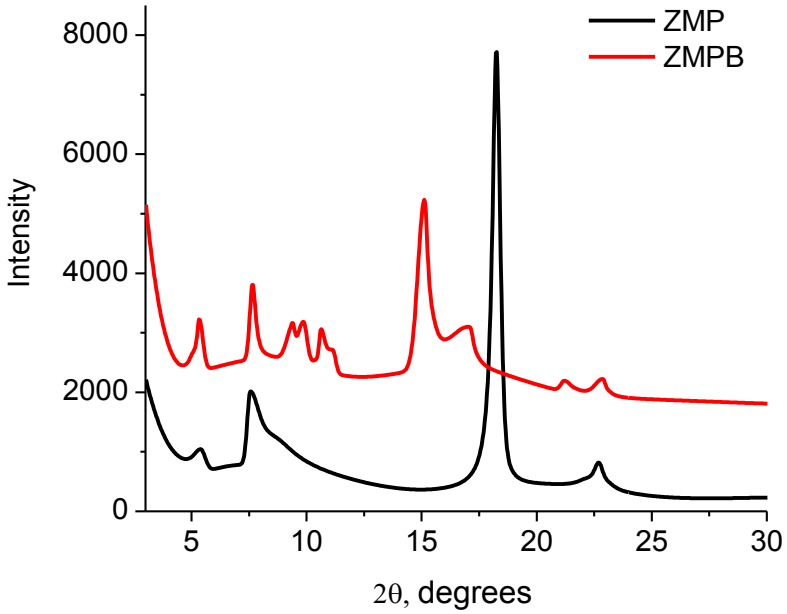

Figure 6.5 Powder XRD profiles (Cu Ka radiation, k = 1.54056 Å) of ZMPB and ZMP MMPF powders. The y-axis of ZMPB has been shifted by *ca.* 2500 counts to enable comparison of the patterns.

As noted above, ZMPB and ZMP crystals are not soluble in polar solvents such as water, ethanol, and DMF or in nonpolar solvents such as benzene and toluene, making optical spectroscopic characterization of the materials challenging. To get around this issue, samples were dispersed in various polymer matrices to achieve the most homogeneous sample possible for spectroscopy measurements. The most convenient polymer matrix to use was a 4 wt% solution of poly(vinyl alcohol) (PVA) in water. To

prepare the dispersion, a sample vial containing a mixture of PVA solution and solid ZMPB or ZMP was sonicated for at least 10 minutes before pouring the dispersions in 35-mm petri dishes to set the films.

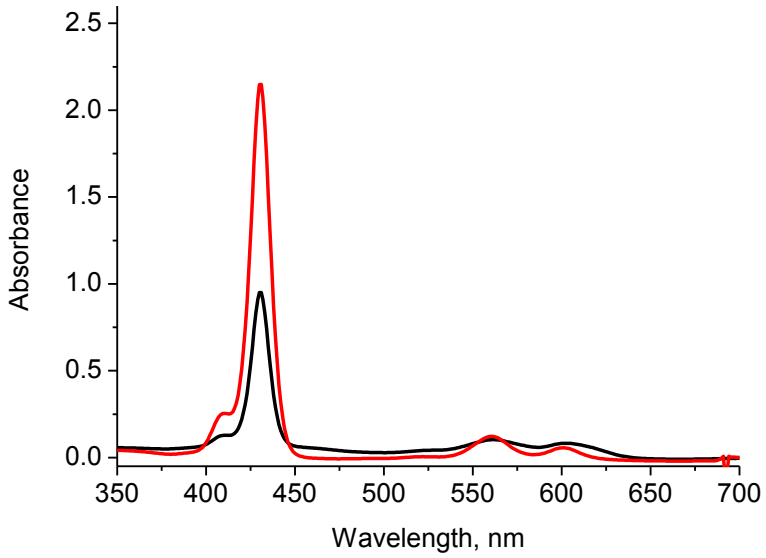

Figure 6.6. UV-Vis absorption spectra of 2mg ZMPB (black) and ZMP (red) crystals dispersed in 2mL of 4% aqueous PVA and subsequently dried into thin films.

The steady state absorption spectra of ZMPB and ZMP in PVA films are shown in Figure 6.6. In contrast to the blue-shift of the Soret band and the red-shift of the Q bands observed in LBL films, ZMPB and ZMP in PVA films showed typical absorption and emission spectra of MPs. The Soret absorption band is centered at 430 nm and the Q bands at 560 nm and 600 nm. The emission Q-bands are centered at 604 nm and 660 nm when excited at 430 nm or 532 nm (Figure A6.3). The emission peak positions remain unchanged with varying excitation wavelengths. ZMPB exhibits negligible prompt S_2 emission when excited at 405 nm (Figure 6.7, black curve). The significance of this observation is discussed in connection with other spectroscopic properties of ZMPB and

presented in the next paragraph. The steady state absorption and emission profiles of ZMPB and ZMP in PVA were *ca.* 2-5 nm red-shifted relative to ZnTCPP solution spectra (See Table A6.1 for a comparison of peak positions of ZnTCPP in ethanol solution, ZMPB and ZMP in PVA matrix with literature values). No significant broadening and "B-Q band intensity borrowing" is observed. B-Q band intensity borrowing is used to describe a decrease in intensity ratio between the Soret band and the Q band and is attributed to B-Q coupling.[55] The observed red shift with no corresponding broadening in the spectra is similar to what was observed with the ZnTMPyP system in Chapter 3. Replacement of the chloride counter ions with heavier iodide ions resulted in 1-3 nm red-shift in the ZnTMPyP absorption spectra. ZnTCPP molecules in ZMPB and ZMP crystals are bound to zinc nodes. The heavy zinc ions caused a slight bathochromic shift in ZMPB and ZMP absorption spectra as often observed when lighter atoms in peripheral positions of a chromophore are replaced by heavier atoms.[75] Excitation scans of the emission peaks at 433 nm, 604 nm and 660 nm show excitation peaks at 430 nm with a weak shoulder at 408 nm and 560 nm (See Figure A6.4). This overlaps well with the absorption spectrum of ZMPB described above and shown in Figure 6.6. This indicated that other components such as zinc nodes, coordinated solvent and bipyridine pillar (in ZMPB only) in the MMPF crystals did not interfere in the spectral region of interest and the observed emission peaks were due only to ZnTCPP in the framework.

As a preliminary investigation, the films were tested for their potential as dual S-E in *homo*-NCPU-TTA by exciting at 560 nm and collecting the emission signal from 390 nm – 470 nm. The UC emission spectrum of ZMPB in PVA films is presented in Figure 6.8A. A very weak signal can be seen at *ca.* 440 nm. Exposing the sample to air and

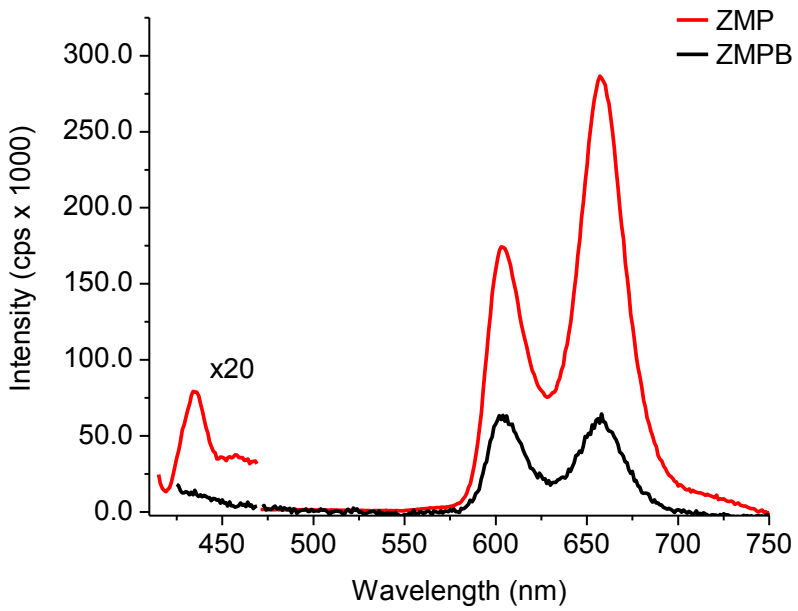

Figure 6.7. Emission spectra of ZMPB (black) and ZMP (red) excited at 405 nm. The Soret band intensity is multiplied by 20 for easy viewing.±

collecting the spectrum after a minute of air exposure resulted in a decrease in intensity of the 440 nm signal. Dispersing ZMPB in degassed toluene (data not shown) resulted in a similar weak signal at 440 nm. This signal is absent when ZMPB is dispersed in aerated toluene, indicating sensitivity to atmospheric oxygen. The peak at 460 nm is likely caused by an instrumental artifact that currently remains unidentified; this peak had been observed when collecting upconverted emission of MP solutions in toluene and also of bare glass as reference. The sensitivity of the 440 nm signal to oxygen supports that the very weak signal is due to NCPU-TTA. A second typical diagnostic test for NCPU-TTA is to measure the power dependence of the UC signal as done in Chapters 4 and 5. However, this experiment could not be performed with any real confidence given the very low signal even at the maximum power (41 mW) of the laser diode used. The results are

inconclusive given the limited data collected. The optical density of the ZMPB in PVA films was sufficient to see up-conversion but the 440 nm signal, if it is indeed NCPU-TTA, was very weak. This result suggests one of two possibilities: 1) the BPY pillar acts as electron accepting quenchers of the S_2 state; [164] 2) the MP orientation (face-to-face-stacked) in ZMPB is not an appropriate orientation for efficient NCPU-TTA. Taking into account the absence of prompt S_2 emission (Figure 6.7, black curve) and very weak upconverted emission in ZMPB (Figure 6.8A) supports the scenario of BPY quenching action. This fluorescence quenching effect by nitrogen containing ligands has been reported previously and are believed to be a consequence of the complexation-induced alteration of the S_2 excited state dynamics. [164] To further verify that BPY acted as quencher, the spectroscopic properties of ZMP crystals (which do not contain BPY pillars) were collected. Figure 6.7, red curve shows weak but distinct prompt S_2 emission while Figure 6.8B shows the UC emission spectra of ZMP dispersed in PVA films at different power excitations from a 560 nm diode laser. Since the only difference in ZMP and ZMPB components is the presence of BPY pillars in ZMPB, it is reasonable to conclude that BPY indeed acted as a prompt S_2 emission quencher. The ZMP UC peak center is at *ca.* 436 nm and the emission intensities showed power dependence. These are consistent with UC emission spectra of ZnTCPP previously measured on TiO_2 surfaces.[156] The inset of Figure 6.8 B shows the double logarithmic plot of upconverted emission as a function of varying laser power. The plot is linear with a slope of 1.1. For a laser spot size approximately equal to 0.031 cm^2, this indicates that the power densities used in this work ranged from 300-1300 $mW \cdot cm^{-2}$. These values are significantly greater than those used to achieve up-conversion for hetero-NCPU-TTA S-E pairs dispersed in polymer (< 20

mW·cm^{-2}) or for S-Es incorporated in MOFs (< 2 mW·cm^{-2}). [42, 46, 119] Therefore, the linear dependence observed is reasonable as it falls in the strong annihilation regime where TTA is the dominant decay pathway for the triplet states, and the upconverted emission intensity varies linearly with the excitation power density.

Unlike solution phase samples, UC emission of ZMP in PVA persisted even under aerated conditions. This can be rationally attributed to the use of PVA, which is a known oxygen barrier[165] and the incorporation of the ZnTCPP sensitizer within the MMPF network. It is unlikely that a large amount of oxygen was dissolved in the PVA solution or trapped in the MMPF structure during sample preparation. This is due to the inherent low solubility of oxygen gas at elevated temperatures in liquid solutions or in porous solids. Thus, the most likely source of oxygen is from diffusion of oxygen through the PVA barrier followed by diffusion within the MMPF network. The triplet state quenching effect of oxygen, then, is determined by the relative rates of two processes – the rate of diffusion of oxygen in the ZMP/PVA film and the rate of TTA. Given that the ZnTCPP molecules are close to each other in the MMPFs, it is reasonable to infer that the rate of oxygen diffusion is slow compared to the rate of proximal TTA.

The observation of TTA in ZMP/PVA is promising as it points to the possibility of *homo*-NCPU-TTA in practical operating conditions (i.e. open to the atmosphere). Although it cannot be completely ruled out at this point that there is a possibility of getting TTA from unreacted ZnTCPP, it is likely minimal for reasons that will be elucidated in the following discussions. It has been reported that NCPU-TTA can be observed in ZnTPP dispersed in PMMA, a rigid polymer that rules out diffusional TTA, when ZnTPP were pre-aggregated in the films.[17] Boutin *et al.* reported that at low dye loading, presumably below

their lower limit data point of 0.70 %, NCPU-TTA was not observed in ZnTPP/PMMA film as a result of large intermolecular separation.[45] Here, the ZMP dye loading in PVA was 0.10 %, significantly lower than 0.77 %. It can be argued that observation of TTA from unreacted ZnTCPP will require a large number of ZnTCPP molecules and it is unlikely that there is much unreacted material present in the sample. Further, because of the PVA matrix, it is unlikely that any unreacted ZnTCPP could result in TTA through diffusional encounters. Diffusional TTA might reasonably be expected to occur in a PVA matrix at temperatures near or equal to its glass transition temperature, T_g. However, the conditions used in this experiment (room temperature = 25°C) is well below the 85°C glass transition temperature of the PVA used here. Hence, the observed higher efficiencies of NCPU-TTA in this system is not likely to be due to diffusional TTA caused by unreacted impurities. Therefore, the lower concentration required to observed TTA in ZMP/PVA can be qualitatively interpreted as MPs incorporated in MMPFs show better NCPU-TTA efficiencies.

The UC signals observed from ZMP/PVA films, while measurable, are relatively weak. While this is a disadvantage in terms of practical applications, this is still an important result in terms of advancing our fundamental understanding of TTA in the solid state. This is the first observation of *homo*-NCPU-TTA in the solid state where diffusion is negligible and deoxygenation is not performed. Further research efforts, both experimental and theoretical, to better understand this effect will continue in the future.

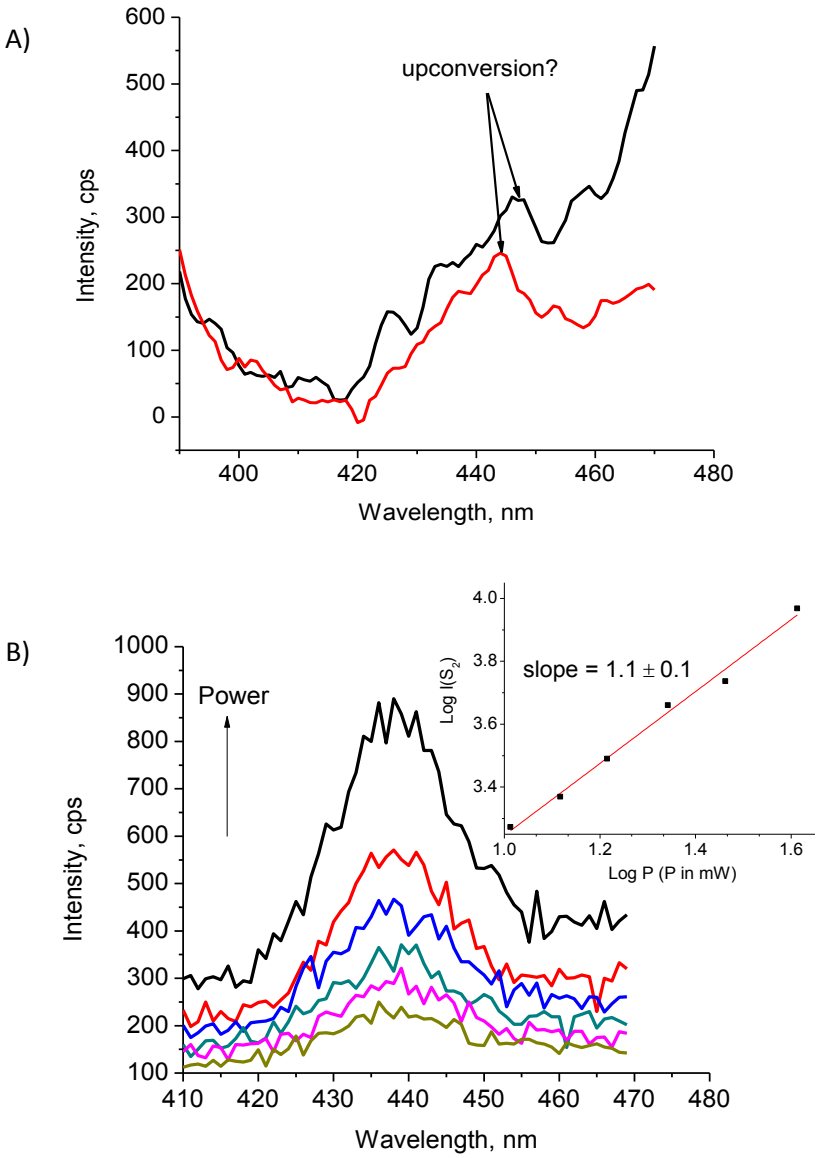

Figure 6.8. A) UC emission of 0.2 % (w/w) ZMPB/PVA thin films excited with 42 mW, 560 nm diode laser under vacuum (black curve) and after re-introducing air (red curve) B) UC emission of 0.10% (w/w) ZMP in PVA thin films at different power Inset: Plot of $\log_{10}$ of S_2 fluorescence intensity versus $\log_{10}$ of laser power using a 560 nm cw laser and back-face excitation.

6.5 Conclusions

This chapter demonstrated the results of a preliminary study on the potential of MMPFs as dual S-E in *homo*-NCPU-TTA. Steady state absorption and emission spectra of LBL assembled ZMPB show signature spectral profiles of H-aggregates. ZMPB contains ZnTCPP, which is known as a dual S-E in solution phase NCPU-TTA. However, 35 layers of ZMPB LBL film did not show upconverted S_2 emission when excited at lower wavelengths due to insufficient exciton concentration for efficient NCPU-TTA. Dispersing ZMPB in PVA films show typical absorption and emission spectral profile of MPs. Testing its potential for NCPU-TTA showed a very weak signal at 440 nm reasonably due to S_2 quenching by the BPY pillar. However, ZMP showed measurable upconverted emission that scaled linearly with excitation power, even under aerated conditions. This is an important observation as this is the first report of *homo*-NCPU-TTA in aerated conditions.

CHAPTER 7. OVERALL CONCLUSIONS AND FUTURE WORK

This thesis presented works associated with the effects of photo-related processes on NCPU-TTA efficiency. The processes studied were iodide quenching of S_1 and S_2 states of MPs; TiO_2 photoanode band gap tuning such that it falls between MP's S_1 and S_2 states; control of the aggregation of MPs; and control of both distance and spatial orientation of MPs. These studies were carried out to help determine how *homo*-NCPU-TTA can be incorporated within the DSSC sandwich design.

In Chapter 3, it was demonstrated that redox shuttles containing iodide can be used in MP-based *homo*-NCPU-TTA. This conclusion was based on the observed minimal quenching of the model MP's S_2 state. This is a significant result in view of the utility of MPs as up-converter dyes in DSSCs. However, the MPs used in this study are model systems – chosen for their well-known excited state dynamics. The MPs have low absorptivity in the NIR and IR region which makes them impractical for implementation in real NCPU-TTA devices. It is important to identify more suitable MP systems to study quenching interactions between redox shuttle components and excited states of the dual S-E dye. Ideally, these systems should absorb strongly throughout the near UV to IR region and satisfy all the other requirements of a good dual S-E dye as was outlined in Chapter 4. Significant work has been done by several groups to increase the photon harvesting ability of MPs. Extending porphyrins' π-conjugation either by synthetic addition of chromophores bridged by acetylenic spacers, or by peripheral fusion of aromatic chromophores to porphyrins was shown to improve their optical absorption in the visible and infrared region (see review by Higashino and Imahori).[166] It is reasonable that the closed-shell metallated derivatives of these dyes, when used as up-converters, can serve

to capture a larger fraction of the solar spectrum and exhibit better *homo*-NCPU-TTA potential than MPs featured in this work.

This thesis also investigated conditions that would minimize NCPU-TTA losses due to electron injection from the S_1 state of the dual S-E dye to the photoanode. The approach of mixing TiO_2 and ZrO_2 to tune the bandgap of TiO_2, such that it falls above the S_1 state and matches the S_2 state of ZnTPP was, in principle, theoretically and experimentally sound. It was hoped that this band gap and S_2 energy level matching will lead to minimum energy loss upon electron injection from the TTA generated S_2 state to the photoanode. However, variations in film morphology and random dye aggregation in film defects facilitated NCPU-TTA, regardless of the relative energy levels of the photoanode. A few changes in the approach used here can be performed in the future to address this issue. For example, improvements can be made in the photoanode morphology through advancements in photoanode fabrication. One such technique involves the use of atomic layer deposition (ALD) in conjunction with anodic alumina oxide (AAO) templates to deposit diverse pinhole-free metal oxides coatings with Angstrom level control over thickness, thus minimal film morphology variations.[167] ALD offers the possibility of depositing high-surface-area mixed metal oxide photoanodes. This is of importance in future studies related to tuning the band gap of mixed metal oxides in order to match the energy of the TTA generated higher excited states. When advancements in film morphology control are made, they are best used in conjunction with new dyes and redox couples in order to achieve significant improvements in overall DSSC efficiency. [167]

Since controlling dye aggregation on metal oxide surfaces was deemed crucial in order to achieve overall research goals, approaches for creating well-ordered MP

assemblies on solid substrates were explored. Langmuir Blodgett (LB) deposition to form slipped-edged MP aggregates; layer-by-layer (LBL) assembly to grow face-to-face stacked MP networks; and dispersion of metal-metalloporphyrin frameworks (MMPFs) in polymer films were among the approaches employed in this work. Results from the various techniques used highlighted the importance of both molecular separation and orientation for efficient *homo*-NCPU-TTA. This was evident when well-ordered, slipped-edged MPs in LB films did not exhibit NCPU-TTA despite satisfying Dexter ET distances. This was further supported by preliminary observation of UC emission on only one of the MMPFs (i.e. the ZMP crystals), even though, both MMPFs synthesized in this work have small intermolecular distances and have similar orientation. The complex dependence of ET on distance and orientation is indeed a well-known puzzle that remains a subject of experimental and theoretical research.[168, 169] Scholes *et al.* noted that even though interchromophore centre-to-centre distances need to be close (*ca.* 6 to 25 Å) for optimum energy transfer rates, they cannot be too close to prevent formation of non-fluorescent dimers which can deplete exciton populations.[168] In this regard, reticular synthesis of MMPFs provides a promising direction for future work to precisely control distance and orientation of dual S-E dyes as MMPF struts. Mahato *et al.* have already successfully used reticular synthesis to create well-ordered arrays of the benchmark emitter molecules in *hetero*-NCPU-TTA.[42] This thesis shows that the strategy can be used for ordered arrays of dual S-E chromophores in *homo*-NCPU-TTA. This has opened a wide array of possibilities to create ordered networks of NIR absorbing dual S-E chromophores. With more than 20,000 different MOFs already reported and grouped into established motifs

(see review by Furukawa *et al*.), [170] one can certainly take guidance from these known structures to get the appropriate molecular separation and orientation of S-E pairs.

While ordered networks of MMPFs appear to have enormous potential to boost the efficiency of solid state NCPU-TTA, there are other possible effects that significantly contribute to the relatively weak NCPU observed in aggregated solid state MPs. One of these is the possible presence of other excited electronic states in the vicinity of S_2. Indeed, a number of authors have proposed the existence of an S_2' state [77, 100] and this can provide an alternate relaxation pathway for the TTA-generated S_2. The other possibilities were noted in Chapter 5 and relate to the triplet state dynamics of MP aggregates. As noted, the possibility of a shortened triplet lifetime or the formation of triplet excimers of photoexcited solid-state MPs would lead to insufficient time for triplet-triplet encounter pairs to form and annihilate. The end result of these is negligible up-conversion signal.

The measurements required to study these processes are extremely difficult due to a number of reasons such as low quantum yield of the exciton in question; low photostability of the chromophores; and lack of highly sensitive detectors in the NIR region. Despite experimental difficulties involved, these properties have profound significance in gaining a fundamental understanding of *homo*-NCPU-TTA and overcoming these technical difficulties is a challenging but compelling research in the future.

In addition to further advancements in experimental techniques to study processes involved in NCPU-TTA, exhaustive theoretical studies on how the arrangement of chromophores affect triplet exciton dynamics can significantly augment cognizance of

NCPU-TTA. This is equally challenging as real molecules are intrinsically complex compared with systems considered in theoretical treatments. However, given the vast literature on theoretical studies of energy transfer in natural light harvesting molecules (whose structures are related to MPs), this is certainly not an impossible task.

Clearly, a great deal of work remains, both in theory and in experiment, before *homo*-NCPU-TTA can become technologically viable. However, the results here indicate the approach is extremely promising, and ripe for further development. It is hoped that the insights gained from this thesis will serve as useful guidelines in future studies and optimization of these systems for practical use.

REFERENCES

1. 2014 Key World Statistics. http://www.iea.org/publications/freepublications/publication/KeyWorld2014.pdf (November 06, 2015).

2. World Energy Outlook 2014: Executive Summary. www.iea.org/textbase/npsum/weo2014sum.pdf (November 06, 2015).

3. World Energy Trilemma 2015: Priority Actions on Climate Change and Hot to Balance the Trilemma. https://www.worldenergy.org/publications/2015/world-energy-trilemma-2015-priority-actions-on-climate-change-and-how-to-balance-the-trilemma/ (November 11, 2015).

4. Perlin, J. A History of Photovoltaics. http://www.usc.edu/org/edisonchallenge/2008/ws1/A%20History%20of%20Photovoltaics.pdf (November 11, 2015).

5. Chapin, D. M.; Fuller, C. S.; Pearson, G. L., A New Silicon p-n Junction Photocell for Converting Solar Radiation into Electrical Power. *Journal of Applied Physics* **1954,** 25, (5), 676-677.

6. O'Regan, B.; Grätzel, M., A low-cost, high-efficiency solar cell based on dye-sensitized colloidal TiO_2 films. *Nature* **1991,** 353, (6346), 737-740.

7. Grätzel, M., Recent Advances in Sensitized Mesoscopic Solar Cells. *Accounts of Chemical Research* **2009,** 42, (11), 1788-1798.

8. Best Research-Cell Efficiencies. http://www.nrel.gov/ncpv/images/efficiency_chart.jpg (November 10, 2015).

9. Martinson, A. B. F.; Hamann, T. W.; Pellin, M. J.; Hupp, J. T., New Architectures for Dye-Sensitized Solar Cells. *Chemistry – A European Journal* **2008,** 14, (15), 4458-4467.

10. Nazeeruddin, M. K.; Péchy, P.; Renouard, T.; Zakeeruddin, S. M.; Humphry-Baker, R.; Comte, P.; Liska, P.; Cevey, L.; Costa, E.; Shklover, V.; Spiccia, L.; Deacon, G. B.; Bignozzi, C. A.; Grätzel, M., Engineering of Efficient Panchromatic Sensitizers for Nanocrystalline TiO_2-Based Solar Cells. *Journal of the American Chemical Society* **2001,** 123, (8), 1613-1624.

11. Rochford, J.; Galoppini, E., Zinc(II) Tetraarylporphyrins Anchored to TiO_2, ZnO, and ZrO_2 Nanoparticle Films through Rigid-Rod Linkers. *Langmuir* **2008,** 24, (10), 5366-5374.

12. Wang, H.; Li, H.; Xue, B.; Wang, Z.; Meng, Q.; Chen, L., Solid-State Composite Electrolyte LiI/3-Hydroxypropionitrile/SiO_2 for Dye-Sensitized Solar Cells. *Journal of the American Chemical Society* **2005,** 127, (17), 6394-6401.

13. Wang, P.; Zakeeruddin, S. M.; Moser, J. E.; Nazeeruddin, M. K.; Sekiguchi, T.; Gratzel, M., A stable quasi-solid-state dye-sensitized solar cell with an amphiphilic ruthenium sensitizer and polymer gel electrolyte. *Nat Mater* **2003,** 2, (6), 402-407.

14. Singh-Rachford, T. N.; Castellano, F. N., Photon upconversion based on sensitized triplet-triplet annihilation. *Coordination Chemistry Reviews* **2010,** 254, (21-22), 2560-2573.

15. Trupke, T.; Green, M. A.; Wurfel, P., Improving solar cell efficiencies by up-conversion of sub-band-gap light. *Journal of Applied Physics* **2002,** 92, (7), 4117.

16. Goldschmidt, J. C.; Fischer, S., Upconversion for Photovoltaics – a Review of Materials, Devices and Concepts for Performance Enhancement. *Advanced Optical Materials* **2015,** 3, (4), 510-535.

17. O'Brien, J. A.; Rallabandi, S.; Tripathy, U.; Paige, M. F.; Steer, R. P., Efficient S_2 state production in ZnTPP-PMMA thin films by triplet-triplet annihilation: Evidence of solute aggregation in photon upconversion systems. *Chemical Physics Letters* **2009,** 475, (4-6), 220-222.

18. Sugunan, S. K.; Tripathy, U.; Brunet, S. M. K.; Paige, M. F.; Steer, R. P., Mechanisms of Low-Power Noncoherent Photon Upconversion in Metalloporphyrin-Organic Blue Emitter Systems in Solution. *The Journal of Physical Chemistry A* **2009,** 113, (30), 8548-8556.

19. Grätzel, M., Photoelectrochemical cells. *Nature* **2001,** 414, (6861), 338-344.

20. Shockley, W.; Queisser, H. J., Detailed Balance Limit of Efficiency of p-n Junction Solar Cells. *Journal of Applied Physics* **1961,** 32, (3), 510-519.

21. Janssen, R. A. J.; Nelson, J., Factors Limiting Device Efficiency in Organic Photovoltaics. *Advanced Materials* **2013,** 25, (13), 1847-1858.

22. Kippelen, B.; Bredas, J.-L., Organic photovoltaics. *Energy & Environmental Science* **2009,** 2, (3), 251-261.

23. Trupke, T.; Shalav, A.; Richards, B. S.; Würfel, P.; Green, M. A., Efficiency enhancement of solar cells by luminescent up-conversion of sunlight. *Solar Energy Materials and Solar Cells* **2006,** 90, (18-19), 3327-3338.

24. Shalav, A.; Richards, B. S.; Green, M. A., Luminescent layers for enhanced silicon solar cell performance: Up-conversion. *Solar Energy Materials and Solar Cells* **2007,** 91, (9), 829-842.

25. de Wild, J.; Meijerink, A.; Rath, J. K.; van Sark, W.; Schropp, R. E. I., Upconverter solar cells: materials and applications. *Energy & Environmental Science* **2011,** 4, (12), 4835-4848.

26. Shalav, A.; Richards, B. S.; Trupke, T.; Krämer, K. W.; Güdel, H. U., Application of $NaYF_4:Er^{3+}$ up-converting phosphors for enhanced near-infrared silicon solar cell response. *Applied Physics Letters* **2005,** 86, (1), 013505.

27. Shalav, A.; Richards, B. S.; Trupke, T.; Corkish, R. P.; Kramer, K. W.; Gudel, H. U.; Green, M. A. In *The application of up-converting phosphors for increased solar cell conversion efficiencies*, Proceedings of 3rd World Conference on Photovoltaic Energy Conversion, 18-18 May 2003, 2003; 2003; pp 248-250 Vol.1.

28. Lahoz, F., Ho^{3+}-doped nanophase glass ceramics for efficiency enhancement in silicon solar cells. *Optics Letters* **2008,** 33, (24), 2982-2984.

29. Lahoz, F.; Pérez-Rodríguez, C.; Hernández, S. E.; Martín, I. R.; Lavín, V.; Rodríguez-Mendoza, U. R., Upconversion mechanisms in rare-earth doped glasses to improve the efficiency of silicon solar cells. *Solar Energy Materials and Solar Cells* **2011,** 95, (7), 1671-1677.

30. Shan, G.-B.; Demopoulos, G. P., Near-Infrared Sunlight Harvesting in Dye-Sensitized Solar Cells Via the Insertion of an Upconverter-TiO_2 Nanocomposite Layer. *Advanced Materials* **2010,** 22, (39), 4373-4377.

31. Bhawalkar, J. D.; He, G. S.; Prasad, P. N., Nonlinear multiphoton processes in organic and polymeric materials. *Reports on Progress in Physics* **1996,** 59, (9), 1041.

32. Baluschev, S.; Yu, F.; Miteva, T.; Ahl, S.; Yasuda, A.; Nelles, G.; Knoll, W.; Wegner, G., Metal-Enhanced Up-Conversion Fluorescence: Effective Triplet-Triplet Annihilation near Silver Surface. *Nano Letters* **2005,** 5, (12), 2482-2484.

33. Falk, J. E.; Smith, K. M., *Porphyrins and metalloporphyrins: a new edition based on the original volume by J. E. Falk*. Elsevier Scientific Pub. Co.: 1975.

34. Milgrom, L. R., *The Colours of Life: An Introduction to the Chemistry of Porphyrins and Related Compounds*. Oxford University Press: 1997.

35. Kelley, A. M., *Condensed-Phase Molecular Spectroscopy and Photophysics*. John Wiley and Sons, Inc.: 2013.

36. Lakowicz, J. R., *Principles of Fluorescence Spectroscopy*, 3rd Ed. [e-book] Springer US; 2006 [cited 2015 Nov 11] Available from: MyiLibrary <http://www.myilibrary.com.cyber.usask.ca?ID=133678>.

37. Turro, N. J., *Modern Molecular Photochemistry*. University Science Books: 1991.

38. Gouterman, M.; Wagnière, G. H.; Snyder, L. C., Spectra of porphyrins. *Journal of Molecular Spectroscopy* **1963,** 11, (1), 108-127.

39. Dexter, D. L., A Theory of Sensitized Luminescence in Solids. *The Journal of Chemical Physics* **1953,** 21, (5), 836-850.

40. Förster, T., Zwischenmolekulare Energiewanderung und Fluoreszenz. *Annalen der Physik* **1948,** 437, (1-2), 55-75.

41. Scholes, G. D., Long-range resonance energy transfer in molecular systems. *Annual Review of Physical Chemistry* **2003,** 54, (1), 57-87.

42. Mahato, P.; Monguzzi, A.; Yanai, N.; Yamada, T.; Kimizuka, N., Fast and long-range triplet exciton diffusion in metal-organic frameworks for photon upconversion at ultralow excitation power. *Nat Mater* **2015,** advance online publication.

43. Auckett, J. E.; Chen, Y. Y.; Khoury, T.; Clady, R. G. C. R.; Ekins-Daukes, N. J.; Crossley, M. J.; Schmidt, T. W., Efficient Up-conversion by triplet-triplet annihilation. *J. Phys. Conf. Series* **2009,** 185, 012002.

44. Bachilo, S. M.; Weisman, R. B., Determination of Triplet Quantum Yields from Triplet-Triplet Annihilation Fluorescence. *The Journal of Physical Chemistry A* **2000,** 104, (33), 7711-7714.

45. Boutin, P. C.; Ghiggino, K. P.; Kelly, T. L.; Steer, R. P., Photon Upconversion by Triplet-Triplet Annihilation in $Ru(bpy)_3$- and DPA-Functionalized Polymers. *The Journal of Physical Chemistry Letters* **2013,** 4, (23), 4113-4118.

46. Kim, J.-H.; Deng, F.; Castellano, F. N.; Kim, J.-H., High Efficiency Low-Power Upconverting Soft Materials. *Chemistry of Materials* **2012,** 24, (12), 2250-2252.

47. Lissau, J. S.; Nauroozi, D.; Santoni, M.-P.; Ott, S.; Gardner, J. M.; Morandeira, A., On the efficiency limit of triplet-triplet annihilation for photochemical upconversion. *Physical Chemistry Chemical Physics* **2013,** 12, (1), 66.

48. Stel'makh, G. F.; Tsvirko, M. P., Probability of excited-singlet-state formation in triplet-triplet annihilation. *Journal of Applied Spectroscopy* **1982,** 36, (4), 430-435.

49. Cheng, Y. Y.; Khoury, T.; Clady, R. G. C. R.; Tayebjee, M. J. Y.; Ekins-Daukes, N. J.; Crossley, M. J.; Schmidt, T. W., On the efficiency limit of triplet-triplet annihilation for photochemical upconversion. *Physical Chemistry Chemical Physics* **2010,** 12, (1), 66-71.

50. Hunter, C. A.; Sanders, J. K. M., The nature of .pi.-.pi. interactions. *Journal of the American Chemical Society* **1990,** 112, (14), 5525-5534.

51. Kano, H.; Kobayashi, T., Time-resolved fluorescence and absorption spectroscopies of porphyrin J-aggregates. *Journal of Chemical Physics* **2002,** 116, (1), 184-195.

52. Maiti, N. C.; Mazumdar, S.; Periasamy, N., J- and H-Aggregates of Porphyrin-Surfactant Complexes: Time-Resolved Fluorescence and Other Spectroscopic Studies. *The Journal of Physical Chemistry B* **1998,** 102, (9), 1528-1538.

53. Ogi, S.; Sugiyasu, K.; Manna, S.; Samitsu, S.; Takeuchi, M., Living supramolecular polymerization realized through a biomimetic approach. *Nat Chem* **2014,** 6, (3), 188-195.

54. Ohno, O.; Kaizu, Y.; Kobayashi, H., J-aggregate formation of a water-soluble porphyrin in acidic aqueous media. *The Journal of Chemical Physics* **1993,** 99, (5), 4128-4139.

55. Verma, S.; Ghosh, H. N., Exciton Energy and Charge Transfer in Porphyrin Aggregate/Semiconductor (TiO2) Composites. *The Journal of Physical Chemistry Letters* **2012,** 3, (14), 1877-1884.

56. Würthner, F.; Kaiser, T. E.; Saha-Möller, C. R., J-Aggregates: From Serendipitous Discovery to Supramolecular Engineering of Functional Dye Materials. *Angewandte Chemie International Edition* **2011,** 50, (15), 3376-3410.

57. Lissau, J. S.; Gardner, J. M.; Morandeira, A., Photon Upconversion on Dye-Sensitized Nanostructured ZrO_2 Films. *The Journal of Physical Chemistry C* **2011,** 115, (46), 23226-23232.

58. Lissau, J. S.; Nauroozi, D.; Santoni, M.-P.; Ott, S.; Gardner, J. M.; Morandeira, A., Anchoring Energy Acceptors to Nanostructured ZrO_2 Enhances Photon Upconversion by Sensitized Triplet-Triplet Annihilation Under Simulated Solar Flux. *The Journal of Physical Chemistry C* **2013,** 117, (28), 14493-14501.

59. Giri, N. K.; Ponce, C. P.; Steer, R. P.; Paige, M. F., Homomolecular non-coherent photon upconversion by triplet-triplet annihilation using a zinc porphyrin on wide bandgap semiconductors. *Chemical Physics Letters* **2014,** 598, (0), 17-22.

60. Giribabu, L.; Ashok Kumar, A.; Neeraja, V.; Maiya, B. G., Orientation Dependence of Energy Transfer in an Anthracene–Porphyrin Donor–Acceptor System. *Angewandte Chemie International Edition* **2001,** 40, (19), 3621-3624.

61. Gros, C. P.; Mohammed Aly, S.; El Ojaimi, M.; Barbe, J.-M.; Brisach, F. d. r.; Abd-El-Aziz, A. S.; Guilard, R.; Harvey, P. D., Through space singlet-singlet and triplet-triplet energy transfers in cofacial bisporphyrins held by the carbazoyl spacer. *Journal of Porphyrins and Phthalocyanines* **2007,** 11, (04), 244-257.

62. Wasielewski, M. R., Photoinduced electron transfer in supramolecular systems for artificial photosynthesis. *Chemical Reviews* **1992,** 92, (3), 435-461.

63. Karolczak, J.; Kowalska, D.; Lukaszewicz, A.; Maciejewski, A.; Steer, R. P., Photophysical Studies of Porphyrins and Metalloporphyrins: Accurate Measurements of Fluorescence Spectra and Fluorescence Quantum Yields for Soret Band Excitation of Zinc Tetraphenylporphyrin. *The Journal of Physical Chemistry A* **2004,** 108, (21), 4570-4575.

64. Yao, C.; Kraatz, H.-B.; Steer, R. P., Photophysics of pyrene-labelled compounds of biophysical interest. *Photochemical & Photobiological Sciences* **2005,** 4, (2), 191-199.

65. Ponce, C. P.; Steer, R. P.; Paige, M. F., Photophysics and halide quenching of a cationic metalloporphyrin in water. *Photochemical & Photobiological Sciences* **2013,** 12, (6), 1079-1085.

66. Campbell, W. M.; Burrell, A. K.; Officer, D. L.; Jolley, K., Porphyrins as light harvesters in the dye-sensitized TiO_2 solar cell. *Coordination Chemistry Reviews* **2004,** 248, 1363-1379.

67. Grätzel, M., Recent Advances in Sensitized Mesoscopic Solar Cells. *Accounts of Chemical Research* **2009,** 42, (11), 1788-1798.

68. Lee, M. W.; Lee, D. L.; Yen, W. N.; Yeh, C. Y., Synthesis, Optical and Photovoltaic Properties of Porphyrin Dyes. *Journal of Macromolecular Science, Part A* **2009,** 46, (7), 730-737.

69. Ball, J. M.; Davis, N. K. S.; Wilkinson, J. D.; Kirkpatrick, J.; Teuscher, J.; Gunning, R.; Anderson, H. L.; Snaith, H. J., A panchromatic anthracene-fused porphyrin sensitizer for dye-sensitized solar cells. *RSC Advances* **2012,** 2, (17), 6846-6853.

70. Imahori, H.; Hayashi, S.; Hayashi, H.; Oguro, A.; Eu, S.; Umeyama, T.; Matano, Y., Effects of Porphyrin Substituents and Adsorption Conditions on Photovoltaic Properties of Porphyrin-Sensitized TiO_2 Cells. *The Journal of Physical Chemistry C* **2009,** 113, (42), 18406-18413.

71. Singh-Rachford, T. N.; Castellano, F. N., Pd(II) Phthalocyanine-Sensitized Triplet-Triplet Annihilation from Rubrene. *The Journal of Physical Chemistry A* **2008,** 112, (16), 3550-3556.

72. Singh-Rachford, T. N.; Castellano, F. N., Triplet Sensitized Red-to-Blue Photon Upconversion. *The Journal of Physical Chemistry Letters* **2009,** 1, (1), 195-200.

73. Szmytkowski, J.; Brunet, S. M. K.; Tripathy, U.; O'Brien, J. A.; Paige, M. F.; Steer, R. P., Photophysics and halide quenching of Soret-excited $ZnTPPS^{4-}$ in aqueous media. *Chemical Physics Letters* **2010,** 501, (4-6), 278-282.

74. Hosomizu, K.; Oodoi, M.; Umeyama, T.; Matano, Y.; Yoshida, K.; Isoda, S.; Isosomppi, M.; Tkachenko, N.; Lemmetyinen, H.; Imahori, H., Substituent Effects of

Porphyrins on Structures and Photophysical Properties of Amphiphilic Porphyrin Aggregates. *J. Phys. Chem. B* **2008,** 112, 16517-16524.

75. Serra, A. C.; Pineiro, M.; Rocha Gonsalves, A. M. d.; Abrantes, M.; Laranjo, M.; Santos, A. C.; Botelho, M. F., Halogen atom effect on photophysical and photodynamic characteristics of derivatives of 5,10,15,20-tetrakis(3-hydroxyphenyl)porphyrin. *Journal of Photochemistry and Photobiology B: Biology* **2008,** 92, (1), 59-65.

76. Kalyanasundaram, K., Photochemistry of water-soluble porphyrins: comparative study of isomeric tetrapyridyl- and tetrakis(N-methylpyridiniumyl)porphyrins. *Inorganic Chemistry* **1984,** 23, (16), 2453-2459.

77. Karolczak, J.; Kowalska, D.; Lukaszewicz, A.; Maciejewski, A.; Steer, R. P., Photophysical Studies of Porphyrins and Metalloporphyrins: Accurate Measurements of Fluorescence Spectra and Fluorescence Quantum Yields for Soret Band Excitation of Zinc Tetraphenylporphyrin. *The Journal of Physical Chemistry A* **2004,** 108, (21), 4570-4575.

78. Togashi, D. M.; Costa, S. M. B., Excited state quenching kinetics of zinc meso-tetrakis (N-methylpyridinium-4-yl) porphyrin by methyl viologen in AOT reverse micelles. *Physical Chemistry Chemical Physics* **2002,** 4, (7), 1141-1150.

79. Lebold, T. P.; Yeow, E. K. L.; Steer, R. P., Fluorescence quenching of the S_1 and S_2 states of zinc meso-tetrakis(4-sulfonatophenyl)porphyrin by halide ions. *Photochemical & Photobiological Sciences* **2004,** 3, (2), 160-166.

80. Koops, S. E.; O'Regan, B. C.; Barnes, P. R. F.; Durrant, J. R., Parameters Influencing the Efficiency of Electron Injection in Dye-Sensitized Solar Cells. *Journal of the American Chemical Society* **2009,** 131, (13), 4808-4818.

81. Giri, N. K.; Ponce, C. P.; Steer, R. P.; Paige, M. F., Homomolecular non-coherent photon upconversion by triplet-triplet annihilation using a zinc porphyrin on wide bandgap semiconductors. *Chemical Physics Letters* **2014,** 598, (0), 17-22.

82. Shockley, W.; Queisser, H. J., Detailed Balance Limit of Efficiency of *p-n* Junction Solar Cells. *Journal of Applied Physics* **1961,** 32, (3), 510-&.

83. Li, L. L.; Diau, E. W. G., Porphyrin-sensitized solar cells. *Chemical Society Reviews* **2013,** 42, (1), 291-304.

84. Lee, J.; Jadhav, P.; Reusswig, P. D.; Yost, S. R.; Thompson, N. J.; Congreve, D. N.; Hontz, E.; Van Voorhis, T.; Baldo, M. A., Singlet Exciton Fission Photovoltaics. *Accounts of Chemical Research* 46, (6), 1300-1311.

85. Zou, W. Q.; Visser, C.; Maduro, J. A.; Pshenichnikov, M. S.; Hummelen, J. C., Broadband dye-sensitized upconversion of near-infrared light. *Nature Photonics* **2012,** 6, (8), 560-564.

86. Cheng, Y. Y.; Fuckel, B.; MacQueen, R. W.; Khoury, T.; Clady, R.; Schulze, T. F.; Ekins-Daukes, N. J.; Crossley, M. J.; Stannowski, B.; Lips, K.; Schmidt, T. W., Improving the light-harvesting of amorphous silicon solar cells with photochemical upconversion. *Energy & Environmental Science* **2012,** 5, (5), 6953-6959.

87. Schulze, T. F.; Czolk, J.; Cheng, Y. Y.; Fuckel, B.; MacQueen, R. W.; Khoury, T.; Crossley, M. J.; Stannowski, B.; Lips, K.; Lemmer, U.; Colsmann, A.; Schmidt, T. W., Efficiency Enhancement of Organic and Thin-Film Silicon Solar Cells with Photochemical Upconversion. *Journal of Physical Chemistry C* **2012,** 116, (43), 22794-22801.

88. Schulze, T. F.; Cheng, Y. Y.; Fuckel, B.; MacQueen, R. W.; Danos, A.; Davis, N.; Tayebjee, M. J. Y.; Khoury, T.; Clady, R.; Ekins-Daukes, N. J.; Crossley, M. J.; Stannowski, B.; Lips, K.; Schmidt, T. W., Photochemical Upconversion Enhanced Solar Cells: Effect of a Back Reflector. *Australian Journal of Chemistry* **2012,** 65, (5), 480-485.

89. Ghiggino, K. P.; Giri, N. K.; Hanrieder, J.; Martell, J. D.; Muller, J.; Paige, M. F.; Robotham, B.; Szmytkowski, J.; Steer, R. P., Photophysics of Soret-Excited Tin(IV) Porphyrins in Solution. *Journal of Physical Chemistry A* **2013,** 117, (33), 7833-7840.

90. Maciejewski, A.; Steer, R. P., The Photophysics, Physical Photochemistry and Related Spectroscopy of Thiocarbonyls. *Chemical Reviews* **1993,** 93, (1), 67-98.

91. Itoh, T., Fluorescence and Phosphorescence from Higher Excited States of Organic Molecules. *Chemical Reviews* **2012,** 112, (8), 4541-4568.

92. Burdzinski, G. K., J.; Maciejewski, A.; Steer, R. P.; Velate, S.; Yeow, E. K. L., *Photochemistry and photophysics of highly excited valence states of polyatomic molecules: non-alternant aromatics, thioketones and metalloporphyrins*. Taylor and Francis: New York, 2006; Vol. 14, p 36.

93. Nickel, B., Delayed Fluorescence from Upper Excited Singlet States Sn (n > 1) of the Aromatic Hydrocarbons 1,2-benzanthracene, fluoranthene, pyrene, and chrysene in methylcyclohexane. *Helvetica Chimica Acta* **1978,** 61, (1), 198-222.

94. Yu, H. Z.; Baskin, J. S.; Zewail, A. H., Ultrafast dynamics of porphyrins in the condensed phase: II. Zinc tetraphenylporphyrin. *Journal of Physical Chemistry A* **2002,** 106, (42), 9845-9854.

95. Yeow, E. K. L.; Ziolek, M.; Karolczak, J.; Shevyakov, S. V.; Asato, A. E.; Maciejewski, A.; Steer, R. P., Sequential Forward S_2-S_2 and Back S_1-S_1 (Cyclic) Energy Transfer in a Novel Azulene-Zinc Porphyrin Dyad. *The Journal of Physical Chemistry A* **2004,** 108, (50), 10980-10988.

96. Velate, S.; Liu, X.; Steer, R. P., Does the radiationless relaxation of Soret-excited metalloporphyrins follow the energy gap law? *Chemical Physics Letters* **2006,** 427, (4-6), 295-299.

97. Tripathy, U.; Kowalska, D.; Liu, X.; Velate, S.; Steer, R. P., Photophysics of Soret-Excited Tetrapyrroles in Solution. I. Metalloporphyrins: MgTPP, ZnTPP, and CdTPP. *The Journal of Physical Chemistry A* **2008,** 112, (26), 5824-5833.

98. Sugunan, S. K.; Robotham, B.; Sloan, R. P.; Szmytkowski, J.; Ghiggino, K. P.; Paige, M. F.; Steer, R. P., Photophysics of Untethered ZnTPP-Fullerene Complexes in Solution. *The Journal of Physical Chemistry A* **2011,** 115, (44), 12217-12227.

99. Maiti, M.; Danger, B. R.; Steer, R. P., Photophysics of Soret-Excited Tetrapyrroles in Solution. IV. Radiationless Decay and Triplet-Triplet Annihilation Investigated Using Tetraphenylporphinato Sn(IV). *The Journal of Physical Chemistry A* **2009,** 113, (42), 11318-11326.

100. Lukaszewicz, A.; Karolczak, J.; Kowalska, D.; Maciejewski, A.; Ziolek, M.; Steer, R. P., Photophysical processes in electronic states of zinc tetraphenyl porphyrin accessed on one- and two-photon excitation in the soret region. *Chemical Physics* **2007,** 331, (2-3), 359-372.

101. Liu, X.; Tripathy, U.; Bhosale, S. V.; Langford, S. J.; Steer, R. P., Photophysics of Soret-Excited Tetrapyrroles in Solution. II. Effects of Perdeuteration, Substituent Nature and Position, and Macrocycle Structure and Conformation in Zinc(II) Porphyrins. *The Journal of Physical Chemistry A* **2008,** 112, (38), 8986-8998.

102. Nakai, K.; Kurotobi, K.; Osuka, A.; Uchiyama, M.; Kobayashi, N., Electronic structures of azulene-fused porphyrins as seen by magnetic circular dichroism and TD-DFT calculations. *Journal of Inorganic Biochemistry* **2008,** 102, (3), 466-471.

103. Mataga, N.; Taniguchi, S.; Chosrowjan, H.; Osuka, A.; Yoshida, N., Ultrafast charge transfer and radiationless relaxations from higher excited state (S2) of directly linked Zn-porphyrin (ZP)-acceptor dyads: investigations into fundamental problems of exciplex chemistry. *Chemical Physics* **2003,** 295, (3), 215-228.

104. Deshpande, P. A.; Polisetti, S.; Madras, G., Rapid Synthesis of Ultrahigh Adsorption Capacity Zirconia by a Solution Combustion Technique. *Langmuir* **2011,** 27, (7), 3578-3587.

105. Reddy, B. M.; Reddy, G. K.; Rao, K. N.; Ganesh, I.; Ferreira, J. M. F., Characterization and photocatalytic activity of TiO_2-$M_{(x)}O_{(y)}$ ($M_{(x)}O_{(y)}$ = SiO_2, Al_2O_3, and ZrO_2) mixed oxides synthesized by microwave-induced solution combustion technique. *Journal of Materials Science* **2009,** 44, (18), 4874-4882.

106. Nagaveni, K.; Hegde, M. S.; Ravishankar, N.; Subbanna, G. N.; Madras, G., Synthesis and structure of nanocrystalline TiO_2 with lower band gap showing high photocatalytic activity. *Langmuir* **2004,** 20, (7), 2900-2907.

107. Ito, S.; Chen, P.; Comte, P.; Nazeeruddin, M. K.; Liska, P.; Péchy, P.; Grätzel, M., Fabrication of screen-printing pastes from TiO_2 powders for dye-sensitised solar cells. *Progress in Photovoltaics: Research and Applications* **2007,** 15, (7), 603-612.

108. Tauc, J., Optical properties and electronic structure of amorphous Ge and Si. *Materials Research Bulletin* **1968,** 3, (1), 37-46.

109. Cong, Y.; Li, B.; Yue, S.; Fan, D.; Wang, X.-j., Effect of Oxygen Vacancy on Phase Transition and Photoluminescence Properties of Nanocrystalline Zirconia Synthesized by the One-Pot Reaction. *The Journal of Physical Chemistry C* **2009,** 113, (31), 13974-13978.

110. Lin, C.; Zhang, C.; Lin, J., Phase Transformation and Photoluminescence Properties of Nanocrystalline ZrO_2 Powders Prepared via the Pechini-type Sol-Gel Process. *The Journal of Physical Chemistry C* **2007,** 111, (8), 3300-3307.

111. Gionco, C.; Battiato, A.; Vittone, E.; Paganini, M. C.; Giamello, E., Structural and spectroscopic properties of high temperature prepared ZrO_2-TiO_2 mixed oxides. *Journal of Solid State Chemistry* **2013,** 201, 222-228.

112. Zou, H.; Lin, Y. S., Structural and surface chemical properties of sol-gel derived TiO_2-ZrO_2 oxides. *Applied Catalysis a-General* **2004,** 265, (1), 35-42.

113. Dürr, M.; Rosselli, S.; Yasuda, A.; Nelles, G., Band-Gap Engineering of Metal Oxides for Dye-Sensitized Solar Cells. *The Journal of Physical Chemistry B* **2006,** 110, (43), 21899-21902.

114. Liang, L.; Sheng, Y.; Xu, Y.; Wu, D.; Sun, Y., Optical properties of sol-gel derived ZrO_2-TiO_2 composite films. *Thin Solid Films* **2007,** 515, 7765-7771.

115. Livraghi, S.; Olivero, F.; Paganini, M. C.; Giamello, E., Titanium Ions Dispersed into the ZrO_2 Matrix: Spectroscopic Properties and Photoinduced Electron Transfer. *Journal of Physical Chemistry C* **2010,** 114, (43), 18553-18558.

116. Tokuji, S.; Maeda, C.; Yorimitsu, H.; Osuka, A., New Synthetic Strategy for Diporphyrins: Pinacol Coupling–Rearrangement. *Chemistry – A European Journal* **2011,** 17, (26), 7154-7157.

117. Sugunan, S. K.; Greenwald, C.; Paige, M. F.; Steer, R. P., Efficiency of Noncoherent Photon Upconversion by Triplet-Triplet Annihilation: The C_{60} Plus Anthanthrene System and the Importance of Tuning the Triplet Energies. *The Journal of Physical Chemistry A* **2013,** 117, (26), 5419-5427.

118. Haefele, A.; Blumhoff, J.; Khnayzer, R. S.; Castellano, F. N., Getting to the (Square) Root of the Problem: How to Make Noncoherent Pumped Upconversion Linear. *Journal of Physical Chemistry Letters* **2012,** 3, (3), 299-303.

119. Monguzzi, A.; Mezyk, J.; Scotognella, F.; Tubino, R.; Meinardi, F., Upconversion-induced fluorescence in multicomponent systems: Steady-state excitation power threshold. *Physical Review B* **2008,** 78, (19).

120. Prathapan, S.; Johnson, T. E.; Lindsey, J. S., Building-block synthesis of porphyrin light-harvesting arrays. *Journal of the American Chemical Society* **1993,** 115, (16), 7519-7520.

121. Wasielewski, M. R., Self-Assembly Strategies for Integrating Light Harvesting and Charge Separation in Artificial Photosynthetic Systems. *Accounts of Chemical Research* **2009,** 42, (12), 1910-1921.

122. Auwarter, W.; Ecija, D.; Klappenberger, F.; Barth, J. V., Porphyrins at interfaces. *Nat Chem* **2015,** 7, (2), 105-120.

123. Schulze, T. F.; Schmidt, T. W., Photochemical upconversion: present status and prospects for its application to solar energy conversion. *Energy & Environmental Science* **2015,** 8, (1), 103-125.

124. Gray, V.; Dzebo, D.; Abrahamsson, M.; Albinsson, B.; Moth-Poulsen, K., Triplet-triplet annihilation photon-upconversion: towards solar energy applications. *Physical Chemistry Chemical Physics* **2014,** 16, (22), 10345-10352.

125. Lissau, J. S.; Nauroozi, D.; Santoni, M.-P.; Edvinsson, T.; Ott, S.; Gardner, J. M.; Morandeira, A., What Limits Photon Upconversion on Mesoporous Thin Films Sensitized by Solution-Phase Absorbers? *The Journal of Physical Chemistry C* **2015,** 119, (9), 4550-4564.

126. Goudarzi, H.; Keivanidis, P. E., Triplet-Triplet Annihilation-Induced Up-Converted Delayed Luminescence in Solid-State Organic Composites: Monitoring Low-Energy Photon Up-Conversion at Low Temperatures. *The Journal of Physical Chemistry C* **2015,** 118, (26), 14256-14265.

127. Duan, P.; Yanai, N.; Nagatomi, H.; Kimizuka, N., Photon Upconversion in Supramolecular Gel Matrixes: Spontaneous Accumulation of Light-Harvesting Donor-Acceptor Arrays in Nanofibers and Acquired Air Stability. *Journal of the American Chemical Society* **2015,** 137, (5), 1887-1894.

128. Ogawa, T.; Yanai, N.; Monguzzi, A.; Kimizuka, N., Highly Efficient Photon Upconversion in Self-Assembled Light-Harvesting Molecular Systems. *Scientific Reports* **2015,** 5.

129. Johnson, E.; Aroca, R., Energy transfer between Langmuir-Blodgett monolayers of organic dyes. *Canadian Journal of Chemistry* **1991,** 69, (11), 1728-1731.

130. Paolesse, R.; Bettini, S.; Valli, L.; Giancane, G., Langmuir-Blodgett Films of Porphyrins for Applications in Photovoltaics. In *Applications of Porphyrinoids*, Springer Berlin Heidelberg: 2014; Vol. 34, pp 117-138.

131. Penner, T. L., Energy transfer between J-aggregated dye monolayers. *Thin Solid Films* **1988,** 160, (1-2), 241-250.

132. Yao, M.; Iwamura, Y.; Inoue, H.; Yoshioka, N., Amphiphilic meso-Disubstituted Porphyrins:Synthesis and the Effect of the Hydrophilic Group on Absorption Spectra at the Air-Water Interface. *Langmuir* **2005,** 21, (2), 595-601.

133. Steer, R. P., Concerning correct and incorrect assignments of Soret (S_2-S_0) fluorescence in porphyrinoids: a short critical review. *Photochemical & Photobiological Sciences* **2014,** 13, (8), 1117-1122.

134. Qiu, Y.; Chen, P.; Liu, M., Interfacial Assemblies of Atypical Amphiphilic Porphyrins: Hydrophobicity/Hydrophilicity of Substituents, Annealing Effects, and Supramolecular Chirality. *Langmuir* **2010,** 26, (19), 15272-15277.

135. Liu, L.; Gu, Z.-R.; Liu, S.-Z.; Li, F.-B.; Hu, Q.-Y.; Li, L.; Du, Z.-L., Langmuir-Blodgett films of hexamolybdate and porphyrin prepared by two different approaches: Synthesis, characterization and electrical properties. *Inorganica Chimica Acta* **2014,** 419, (0), 1-6.

136. Rong, Y.; Chen, P.; Wang, D.; Liu, M., Porphyrin Assemblies through the Air/Water Interface: Effect of Hydrogen Bond, Thermal Annealing, and Amplification of Supramolecular Chirality. *Langmuir* **2012,** 28, (15), 6356-6363.

137. Makiura, R.; Konovalov, O., Interfacial growth of large-area single-layer metal-organic framework nanosheets. *Sci. Rep.* **2013,** 3.

138. Qian, D.-J.; Nakamura, C.; Miyake, J., Multiporphyrin Array from Interfacial Metal-Mediated Assembly and Its Langmuir-Blodgett Films. *Langmuir* **2000,** 16, (24), 9615-9619.

139. Bardwell, J.; Bolton, J. R., Monolayer studies of 5-(4-carboxyphenyl)-10,15,20-tritolyl-porphyrin–I. Optical studies of films at the air-water interface and of films transferred onto solid substrates†. *Photochemistry and Photobiology* **1984,** 39, 735-746.

140. Sgobba, V.; Giancane, G.; Conoci, S.; Casilli, S.; Ricciardi, G.; Guldi, D. M.; Prato, M.; Valli, L., Growth and Characterization of Films Containing Fullerenes and Water Soluble Porphyrins for Solar Energy Conversion Applications. *Journal of the American Chemical Society* **2007,** 129, (11), 3148-3156.

141. Schuckman, A. E.; Ewers, B. W.; Yu, L. H.; Tomé, J. P. C.; Pérez, L. M.; Drain, C. M.; Kushmerick, J. G.; Batteas, J. D., Utilizing Nearest-Neighbor Interactions To Alter Charge Transport Mechanisms in Molecular Assemblies of Porphyrins on Surfaces. *The Journal of Physical Chemistry C* **2015,** 119, (24), 13569-13579.

142. Balaban, T. S.; Linke-Schaetzel, M.; Bhise, A. D.; Vanthuyne, N.; Roussel, C.; Anson, C. E.; Buth, G.; Eichhöfer, A.; Foster, K.; Garab, G.; Gliemann, H.; Goddard, R.; Javorfi, T.; Powell, A. K.; Rösner, H.; Schimmel, T., Structural Characterization of Artificial Self-Assembling Porphyrins That Mimic the Natural Chlorosomal

Bacteriochlorophylls c, d, and e. *Chemistry – A European Journal* **2005,** 11, (8), 2267-2275.

143. Ricciardi, G.; Belviso, S.; Giancane, G.; Tafuro, R.; Wagner, T.; Valli, L., Floating Films of a Nonamphiphilic Porphyrazine at the Air-Water Interface and LS Multilayer Construction and Optical Characterization. *The Journal of Physical Chemistry B* **2004,** 108, (23), 7854-7861.

144. Pedrosa, J. M.; Dooling, C. M.; Richardson, T. H.; Hyde, R. K.; Hunter, C. A.; Martín, M. T.; Camacho, L., Influence of Molecular Organization of Asymmetrically Substituted Porphyrins on Their Response to NO_2 Gas. *Langmuir* **2002,** 18, (20), 7594-7601.

145. Satake, A.; Kobuke, Y., Artificial photosynthetic systems: assemblies of slipped cofacial porphyrins and phthalocyanines showing strong electronic coupling. *Organic & Biomolecular Chemistry* **2007,** 5, (11), 1679-1691.

146. Elemans, J. A. A. W.; van Hameren, R.; Nolte, R. J. M.; Rowan, A. E., Molecular Materials by Self-Assembly of Porphyrins, Phthalocyanines, and Perylenes. *Advanced Materials* **2006,** 18, (10), 1251-1266.

147. Lu, X.; Li, M.; Yang, C.; Zhang, L.; Li, Y.; Jiang, L.; Li, H.; Jiang, L.; Liu, C.; Hu, W., Electron Transport through a Self-Assembled Monolayer of Thiol-End-Functionalized Tetraphenylporphines and Metal Tetraphenylporphines. *Langmuir* **2006,** 22, (7), 3035-3039.

148. Menke, S. M.; Holmes, R. J., Exciton diffusion in organic photovoltaic cells. *Energy & Environmental Science* **2014,** 7, (2), 499-512.

149. Ponce, C. P.; Araghi, H. Y.; Joshi, N. K.; Steer, R. P.; Paige, M. F., Spectroscopic and Structural Studies of a Surface Active Porphyrin in Solution and in Langmuir-Blodgett Films. *Langmuir* **2015,** 31, (50), 13590-13599.

150. Lee, S. H.; Thévenaz, D. C.; Weder, C.; Simon, Y. C., Glassy poly(methacrylate) terpolymers with covalently attached emitters and sensitizers for low-power light upconversion. *Journal of Polymer Science Part A: Polymer Chemistry* **2015,** 53, (14), 1629-1639.

151. Yaghi, O. M.; O'Keeffe, M.; Ockwig, N. W.; Chae, H. K.; Eddaoudi, M.; Kim, J., Reticular synthesis and the design of new materials. *Nature* **2003,** 423, (6941), 705-714.

152. Kent, C. A.; Mehl, B. P.; Ma, L.; Papanikolas, J. M.; Meyer, T. J.; Lin, W., Energy Transfer Dynamics in Metal-Organic Frameworks. *Journal of the American Chemical Society* **2010,** 132, (37), 12767-12769.

153. Lee, C. Y.; Farha, O. K.; Hong, B. J.; Sarjeant, A. A.; Nguyen, S. T.; Hupp, J. T., Light-Harvesting Metal-Organic Frameworks (MOFs): Efficient Strut-to-Strut Energy

Transfer in Bodipy and Porphyrin-Based MOFs. *Journal of the American Chemical Society* **2011,** 133, (40), 15858-15861.

154. Zhang, X.; Ballem, M. A.; Hu, Z.-J.; Bergman, P.; Uvdal, K., Nanoscale Light-Harvesting Metal–Organic Frameworks. *Angewandte Chemie International Edition* **2011,** 50, (25), 5729-5733.

155. Gao, W.-Y.; Chrzanowski, M.; Ma, S., Metal-metalloporphyrin frameworks: a resurging class of functional materials. *Chemical Society Reviews* **2014,** 43, (16), 5841-5866.

156. Thunder, T. Characterization of the optical properties of metalloporphyrins in TiO_2 sol-gel films for photon upconversion applications. M.S. Thesis, University of Saskatchewan, Saskatoon, 2013.

157. Choi, E.-Y.; Barron, P. M.; Novotny, R. W.; Son, H.-T.; Hu, C.; Choe, W., Pillared Porphyrin Homologous Series: Intergrowth in Metal-Organic Frameworks. *Inorganic Chemistry* **2009,** 48, (2), 426-428.

158. Decher, G., Fuzzy Nanoassemblies: Toward Layered Polymeric Multicomposites. *Science* **1997,** 277, (5330), 1232-1237.

159. Biemmi, E.; Scherb, C.; Bein, T., Oriented Growth of the Metal Organic Framework $Cu_3(BTC)_2(H_2O)_3 \cdot xH_2O$ Tunable with Functionalized Self-Assembled Monolayers. *Journal of the American Chemical Society* **2007,** 129, (26), 8054-8055.

160. Lee, D. Y.; Shin, C. Y.; Yoon, S. J.; Lee, H. Y.; Lee, W.; Shrestha, N. K.; Lee, J. K.; Han, S.-H., Enhanced photovoltaic performance of Cu-based metal-organic frameworks sensitized solar cell by addition of carbon nanotubes. *Scientific Reports* **2014,** 4, 3930.

161. So, M. C.; Jin, S.; Son, H.-J.; Wiederrecht, G. P.; Farha, O. K.; Hupp, J. T., Layer-by-Layer Fabrication of Oriented Porous Thin Films Based on Porphyrin-Containing Metal-Organic Frameworks. *Journal of the American Chemical Society* **2013,** 135, (42), 15698-15701.

162. Motoyama, S.; Makiura, R.; Sakata, O.; Kitagawa, H., Highly Crystalline Nanofilm by Layering of Porphyrin Metal-Organic Framework Sheets. *Journal of the American Chemical Society* **2011,** 133, (15), 5640-5643.

163. Xu, G.; Yamada, T.; Otsubo, K.; Sakaida, S.; Kitagawa, H., Facile Modular Assembly for Fast Construction of a Highly Oriented Crystalline MOF Nanofilm. *Journal of the American Chemical Society* **2012,** 134, (40), 16524-16527.

164. Danger, B. R.; Bedient, K.; Maiti, M.; Burgess, I. J.; Steer, R. P., Photophysics of Self-Assembled Zinc Porphyrin-Bidentate Diamine Ligand Complexes. *The Journal of Physical Chemistry A* **2010,** 114, (41), 10960-10968.

165. Gaume, J.; Wong-Wah-Chung, P.; Rivaton, A.; Therias, S.; Gardette, J.-L., Photochemical behavior of PVA as an oxygen-barrier polymer for solar cell encapsulation. *RSC Advances* **2011,** 1, (8), 1471-1481.

166. Higashino, T.; Imahori, H., Porphyrins as excellent dyes for dye-sensitized solar cells: recent developments and insights. *Dalton Transactions* **2015,** 44, (2), 448-463.

167. Hamann, T. W.; Jensen, R. A.; Martinson, A. B. F.; Van Ryswyk, H.; Hupp, J. T., Advancing beyond current generation dye-sensitized solar cells. *Energy & Environmental Science* **2008,** 1, (1), 66-78.

168. Scholes, G. D.; Fleming, G. R.; Olaya-Castro, A.; van Grondelle, R., Lessons from nature about solar light harvesting. *Nature Chemistry* **2011,** 3, (10), 763-774.

169. Yuan-Chung, C.; Graham, R. F., Dynamics of Light Harvesting in Photosynthesis. *Annual Review of Physical Chemistry* **2009,** 60, (1), 241-262.

170. Furukawa, H.; Cordova, K. E.; O'Keeffe, M.; Yaghi, O. M., The Chemistry and Applications of Metal-Organic Frameworks. *Science* **2013,** 341, (6149).

171. Gervaldo, M.; Fungo, F.; Durantini, E. N.; Silber, J. J.; Sereno, L.; Otero, L., Carboxyphenyl Metalloporphyrins as Photosensitizers of Semiconductor Film Electrodes. A Study of the Effect of Different Central Metals. *The Journal of Physical Chemistry B* **2005,** 109, (44), 20953-20962.

172. Bonnett, R.; Ioannou, S.; James, A. G.; Pitt, C. W.; Soe, M. M. Z., Synthesis and film-forming properties of metal complexes of octadecyl ethers of 5,10,15,20-tetrakis(4-hydroxyphenyl)porphyrin. *Journal of Materials Chemistry* **1993,** 3, (8), 793-799.

APPENDICES

Supporting Information for Chapter 3

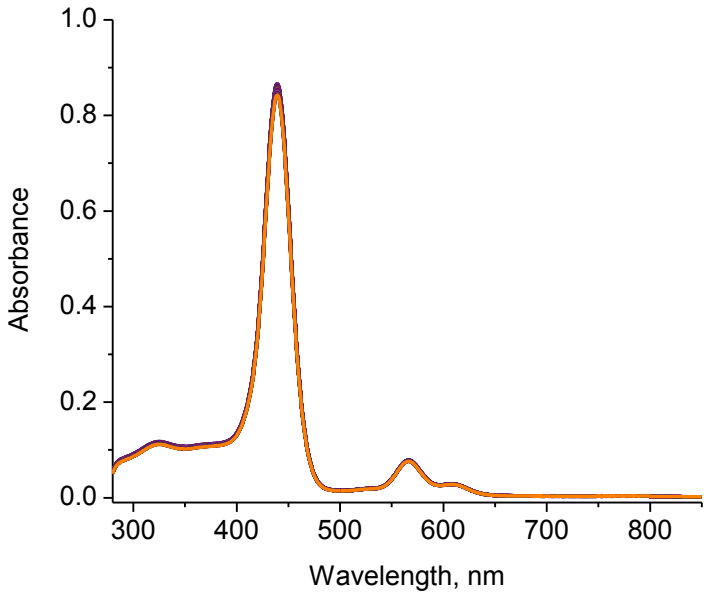

Figure A3.1. Absorption spectra of 5 x 10^{-6} M ZnTMPyP in the presence of 1.0M of NaI in a constant ionic strength of 1.0 M collected forty times at 2 min per cycle.

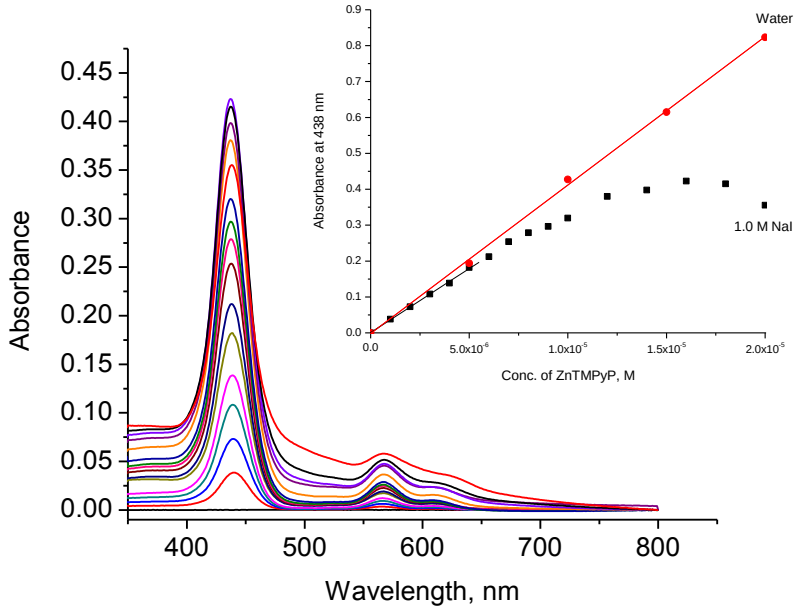

Figure A3.2. Absorption spectra of 0-20 x 10^{-6} M ZnTMPyP in the presence of 1.0M of NaI in a constant ionic strength of 1.0 M. Inset: Beer's law plot of ZnTMPyP in water (circles). Note that ZnTMpyP in aqueous 1.0 M NaI solution (squares) follows Beer's Law at the concentration range of 0-7x10^{-6} M but deviates from it at higher ZnTMPyP concentrations.

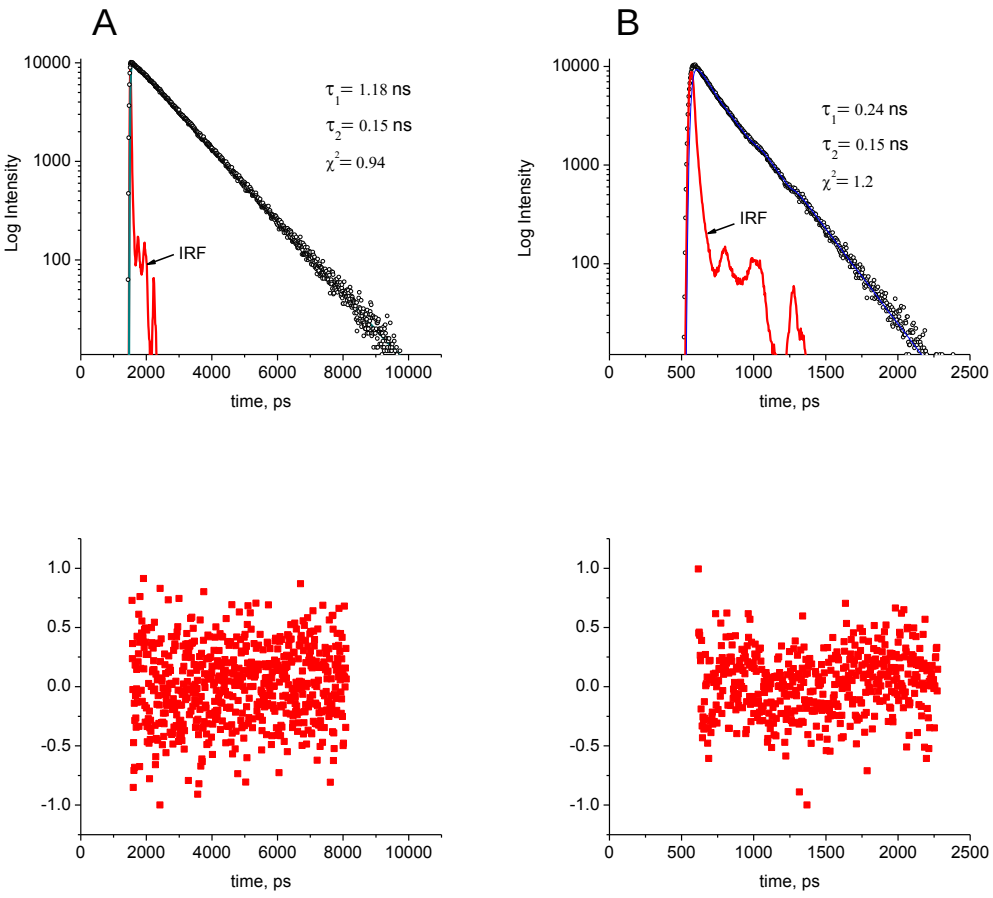

Figure A3.3. Time-correlated single-photon counting data for the S_1 fluorescence decay of ZnTMPyP in A) 1.0 M NaCl and B) 0.5 M NaI at constant ionic strength of 1.0 M collected at room temperature with the excitation wavelength set at 430 nm and the emission observed at 630 nm. The solid line gave the best fit of a convolution of a biexponential decay function with the instrument response function (IRF). Plot below the decay curve is the distribution of residuals for the biexponential fit. Note that the two panels are in different time scales.

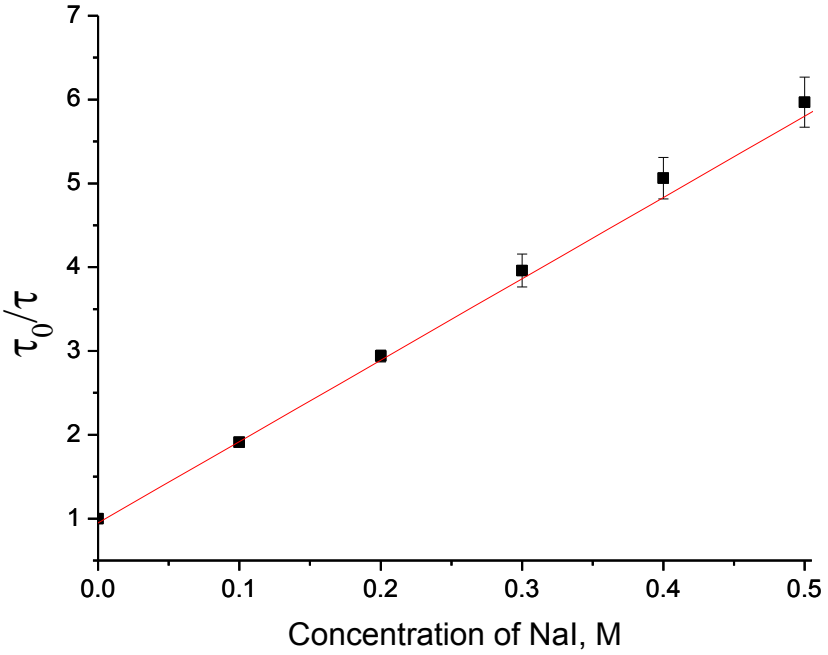

Figure A3.4. Stern-Volmer plots for the iodide quenching of the S_1 state of 5 μM aqueous ZnTMPyP solution, obtained from the ratio of the weighted average of fluorescence lifetimes of the dye without quencher to that with quencher. The K_{SV} from the slope of the line is 10.09 M^{-1}. Error bars are the standard deviation of duplicate measurements.

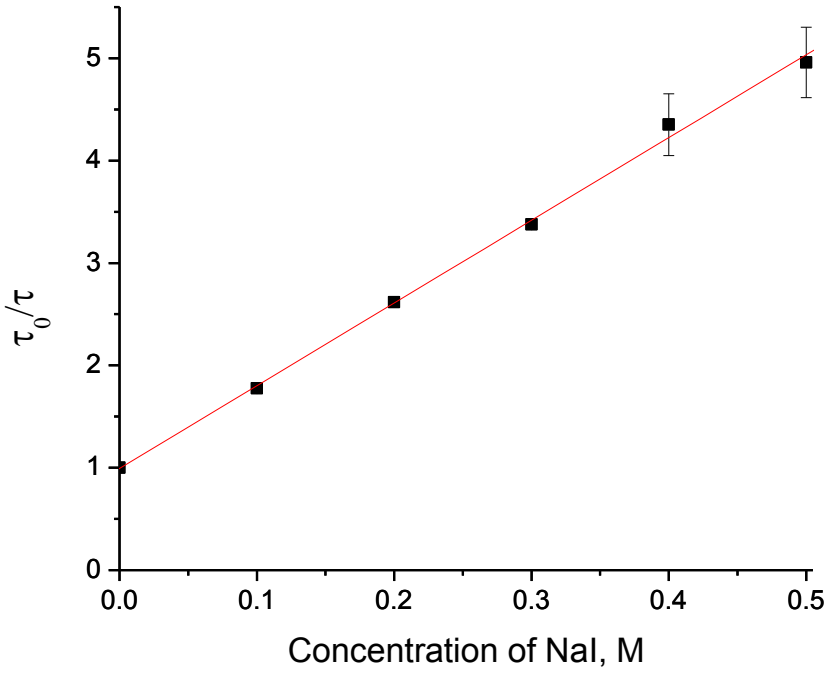

Figure A3.5. Stern-Volmer plots for the iodide quenching of the S_1 state of 5 μM aqueous ZnTMPyP solution, obtained from the ratio of fluorescence lifetimes of the dye without quencher to that with quencher. K_{SV} from the slope of the line is 8.08 M^{-1}. Error bars are the standard deviation of duplicate measurements.

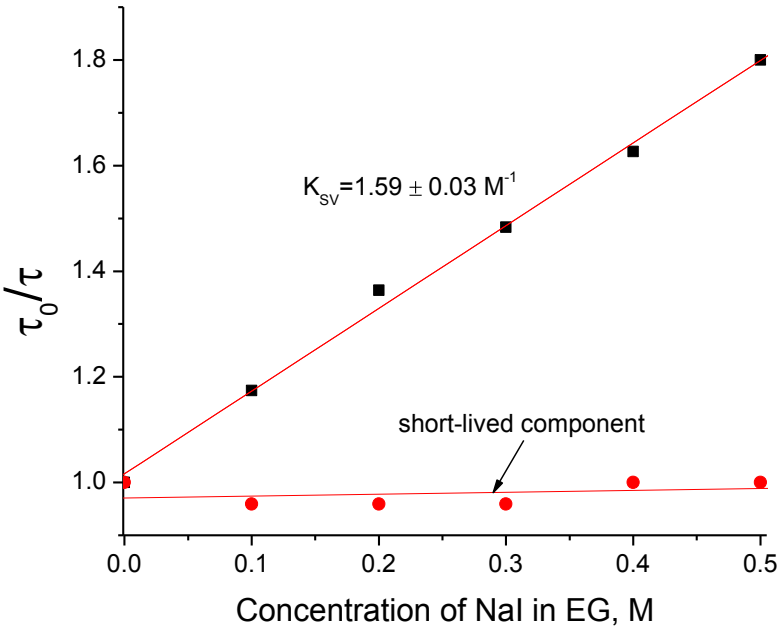

Figure A3.6. Stern-Volmer plots for the iodide quenching of the S_1 state of 5 μM ZnTMPyP in ethylene glycol solution, obtained from the ratio of fluorescence lifetimes of the dye without quencher to that with quencher.

Supporting Information for Chapter 4

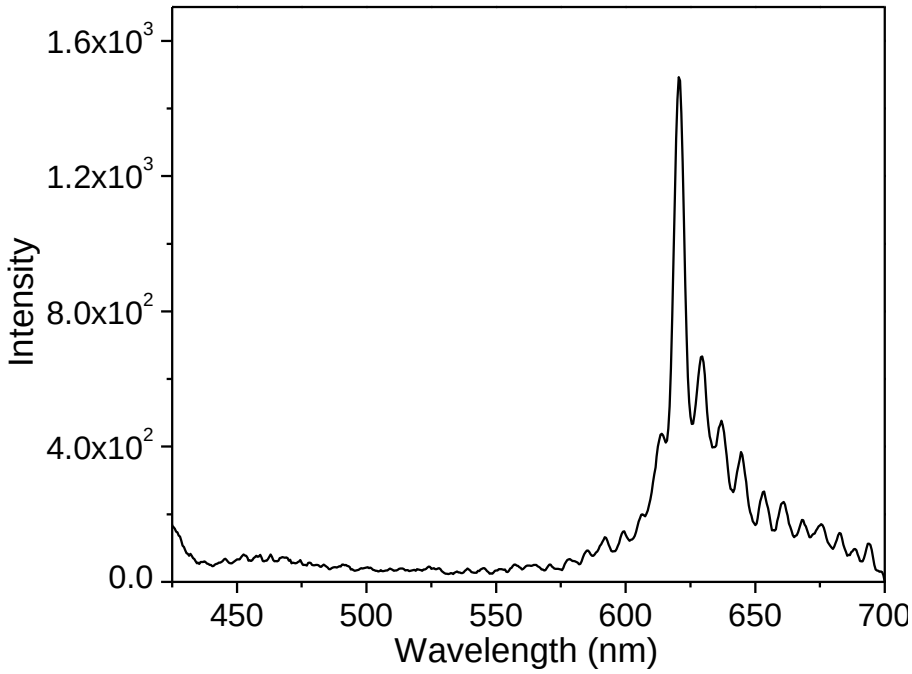

Figure A4.1. Emission spectrum of ZnTPP loaded ZrO_2 film on 405 nm laser excitation (6.83 mW).

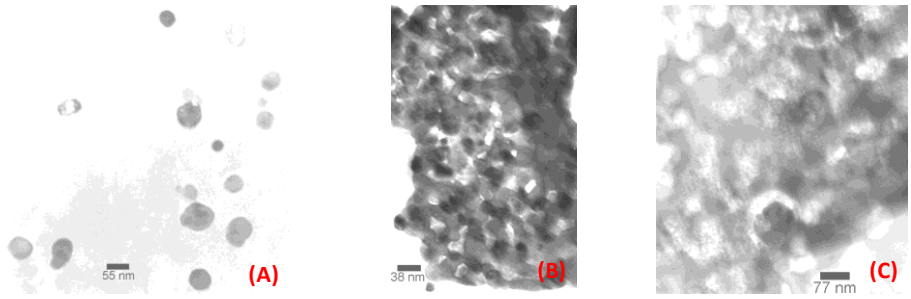

Figure A4.2. Transmission electron micrograph of (A) ZrO_2; mixed oxide (B) ZrO_2/TiO_2 (0.4) and (C) ZrO_2/TiO_2 (0.02). All samples clearly show tiny uneven nanocrystals.

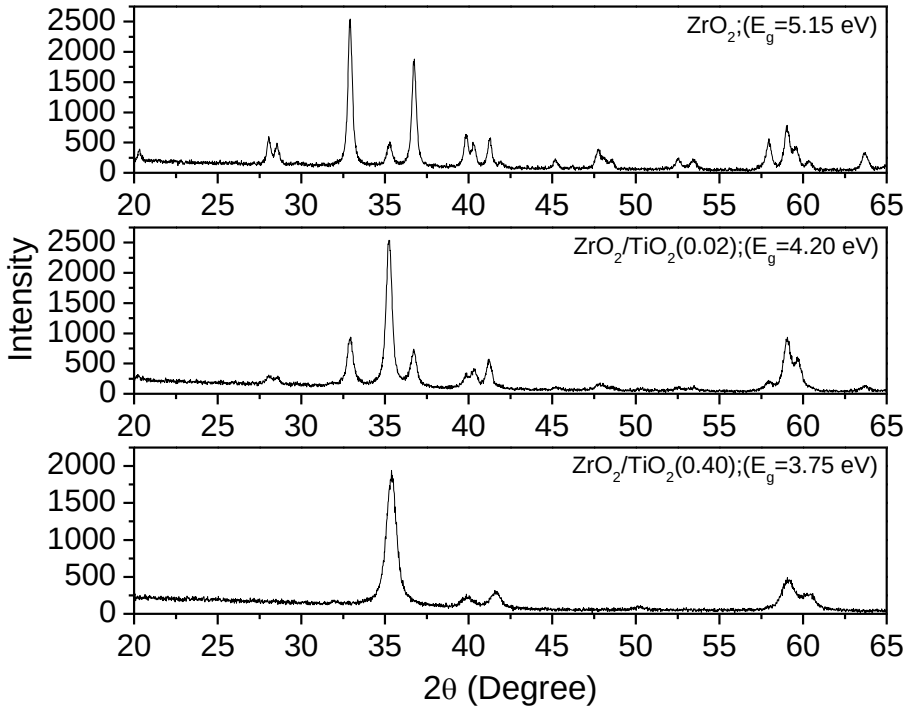

Figure A4.3. X-ray diffraction pattern of ZrO_2, mixed oxide ZrO_2/TiO_2 (0.02) and ZrO_2/TiO_2 (0.4). Sharp and intense diffraction peaks indicate that sample are crystalline in nature.

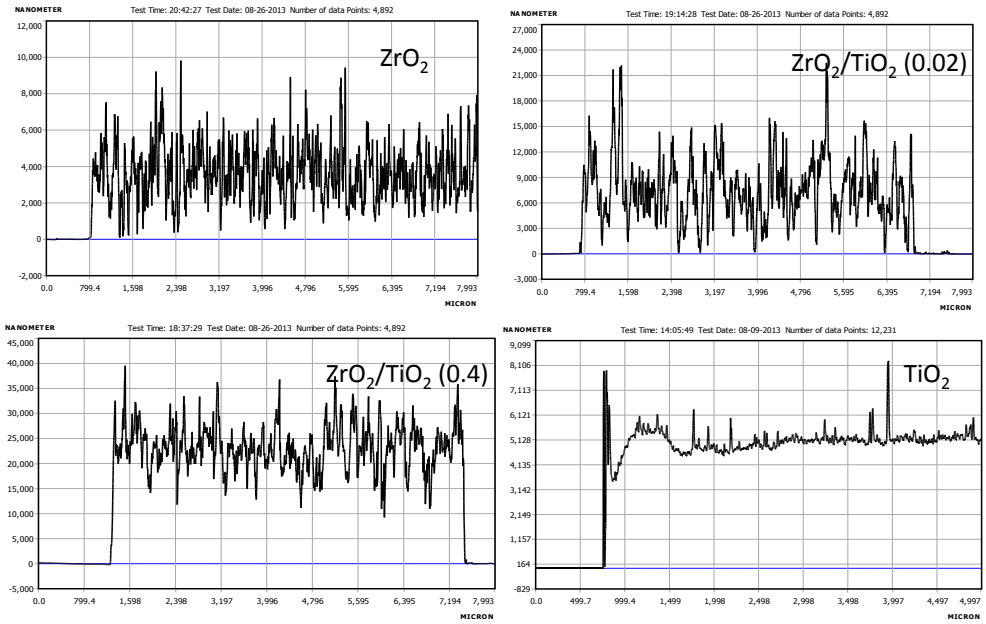

Figure A4.4. Profilometer data for ZrO_2, mixed oxides ZrO_2/TiO_2 (0.02), and ZrO_2/TiO_2 (0.4) and TiO_2 (degussa, P-25). Average thicknesses of the films are 3.56, 6.4, 21.5 and 6.3 microns respectively.

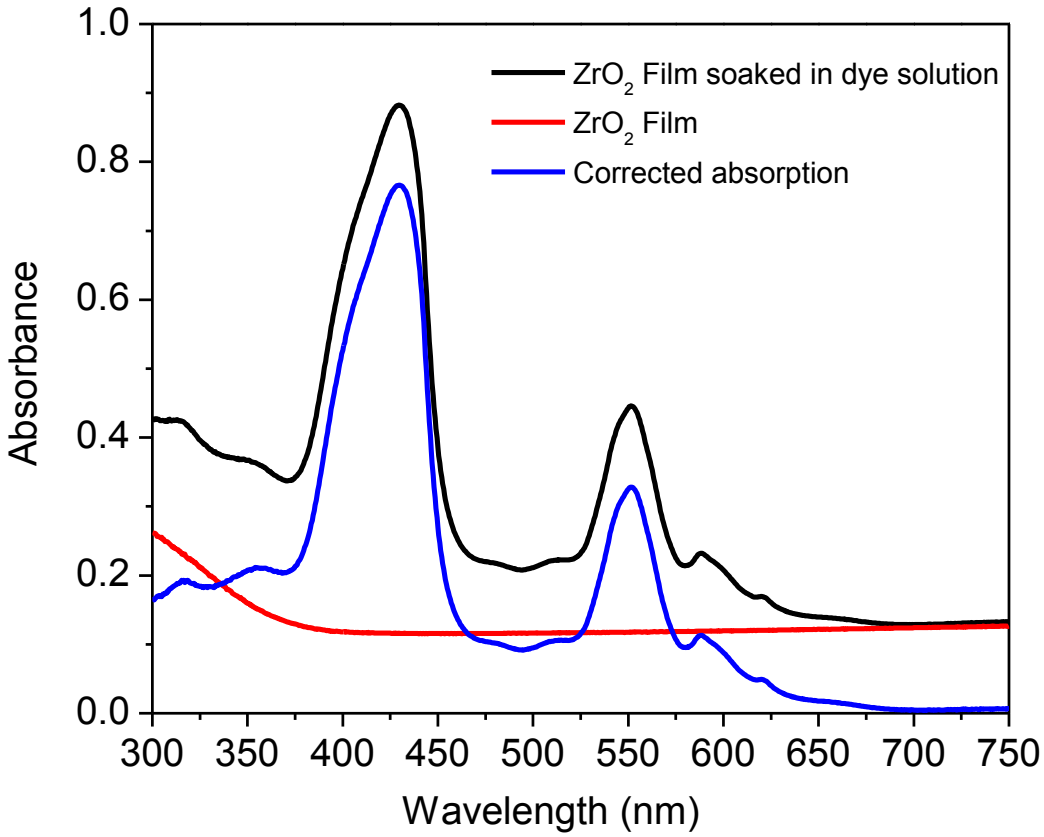

Figure A4.5: Absorption spectra for a ZrO_2 film under various conditions. The red curve shows the absorption spectrum of a ZrO_2 film on a glass slide without ZnTPP (particle size of ZrO_2 was 55 nm, thickness of the film was 1.3 µm). The same film was soaked in ZnTPP solution (2 mM) and the resulting absorption spectrum (black curve) shows the characteristic peaks of ZnTPP. To obtain the corrected absorption spectrum (blue curve), the reference spectrum was subtracted from the original spectrum.

Sample ZrO_2 film_2mM ZnTPP Back face illumination λ_{exc} – 400 nm λ_{ems} – 622 nm	**Fitting Parameters** Scatter Technique Fit: 147-791 IRF Shifted 2 channels Time Base of 19.5 ps/channel Exponential to fit:3 Tolerance on delta chi squared: 0.0001			
Results Iterations #: 352 Chi Squared: 1.27 Z = 4.86 DW = 1.54	Values of a, tau (τ) and F			
	I	**a**	**τ (ps)**	**F**
	1	0.0044	4918.96	0.0729
	2	0.8559	207.00	0.5906
	3	0.1395	722.83	0.3363

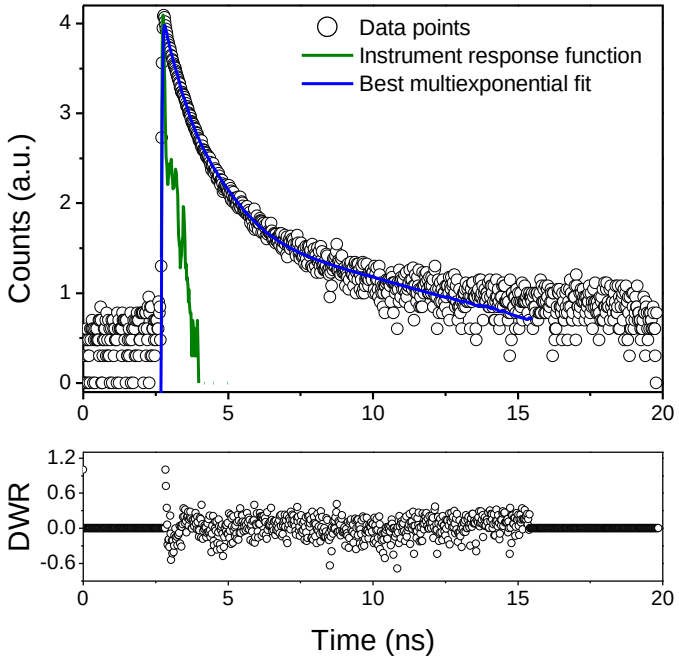

Figure A4.6: S_1-S_0 fluorescence decay of 2.0 μM ZnTPP on ZrO_2 surface, excited at 400 nm and monitored at 622 nm. Open circles are the data points (19.5 ps per channel), and the solid green line is the instrument response function. The solid blue line is the best multiexponential fit to the data determined by the reduced χ^2 value. The lower panel shows the distribution of the weighted residuals. A 550 nm longpass emission filter placed before the detector. Values of a, tau and F are the amplitude, lifetime and fractional intensities, respectively.

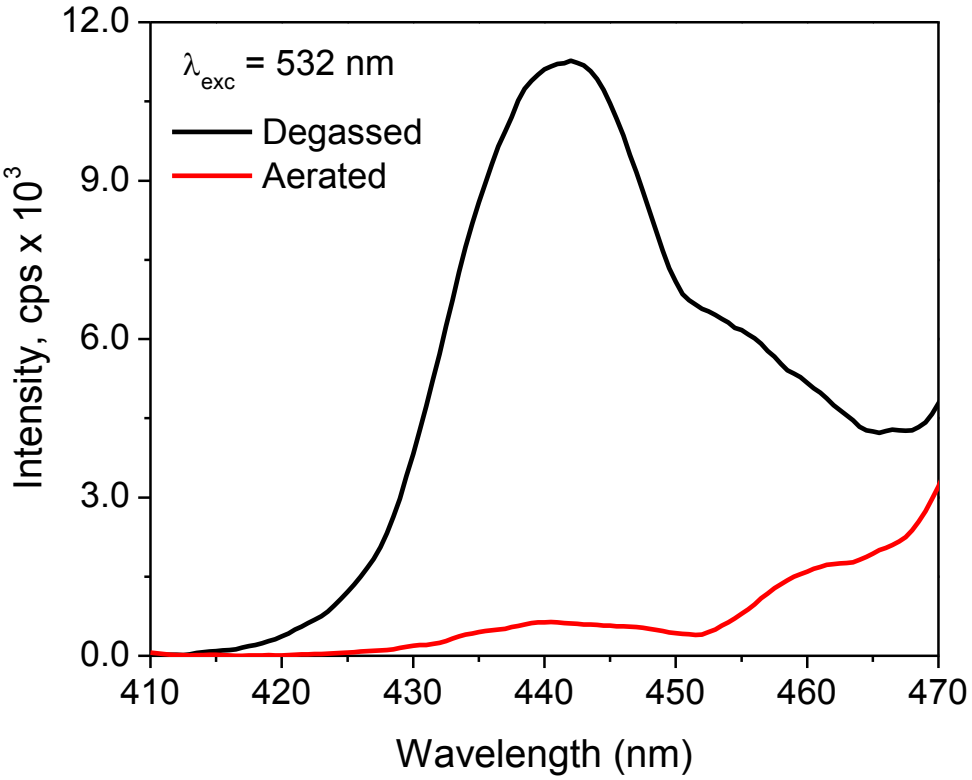

Figure A4.7. Upconverted S_2 emission spectrum of a ZnTPP loaded ZrO_2 film with 532 nm laser excitation (power density 146 $mWcm^{-2}$, integration time 2.4 second) in the absence (black) and presence (red) of oxygen. The quenching effect of oxygen upon the upconverted signal is readily apparent.

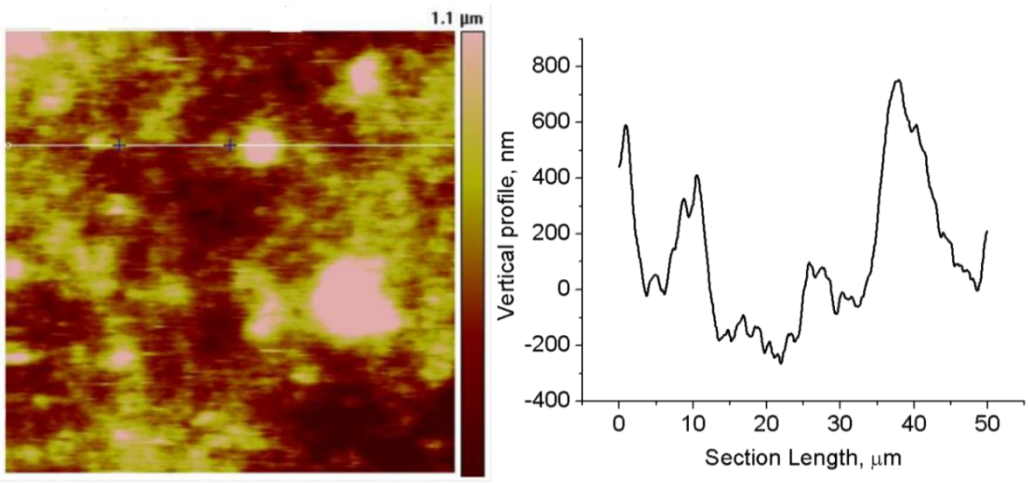

Figure A4.8: Atomic force microscope height image (50µm x 50µm) and corresponding cross-sectional profile of a TiO_2 film.

Supporting Information for Chapter 5

A)

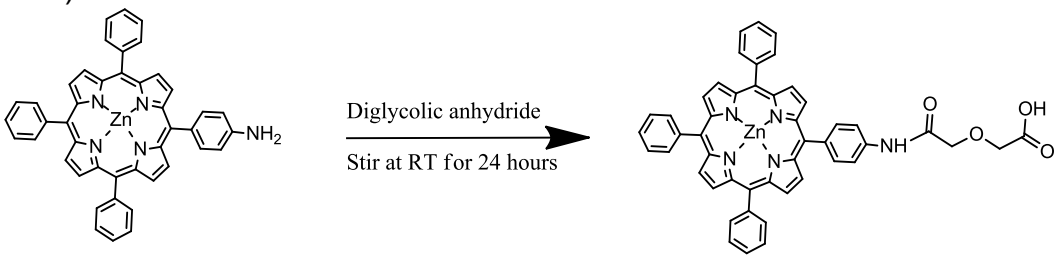

B)

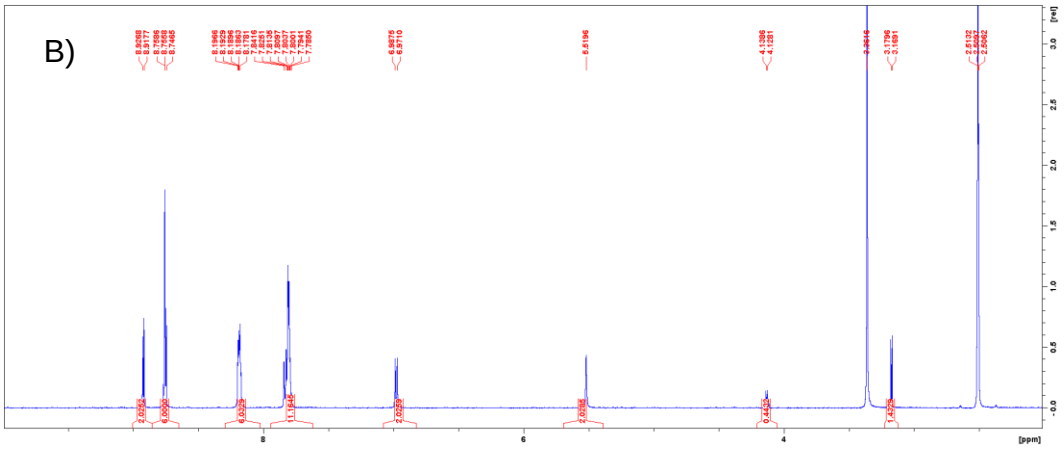

C)

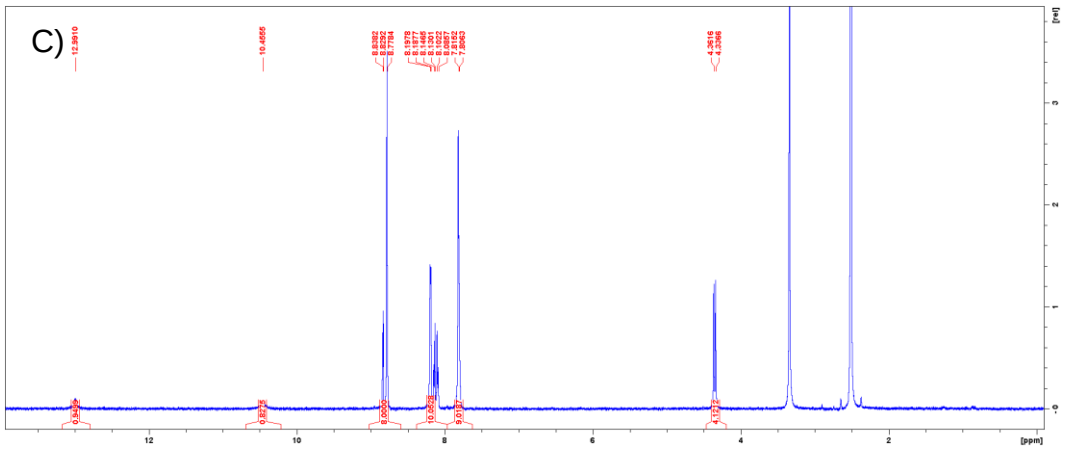

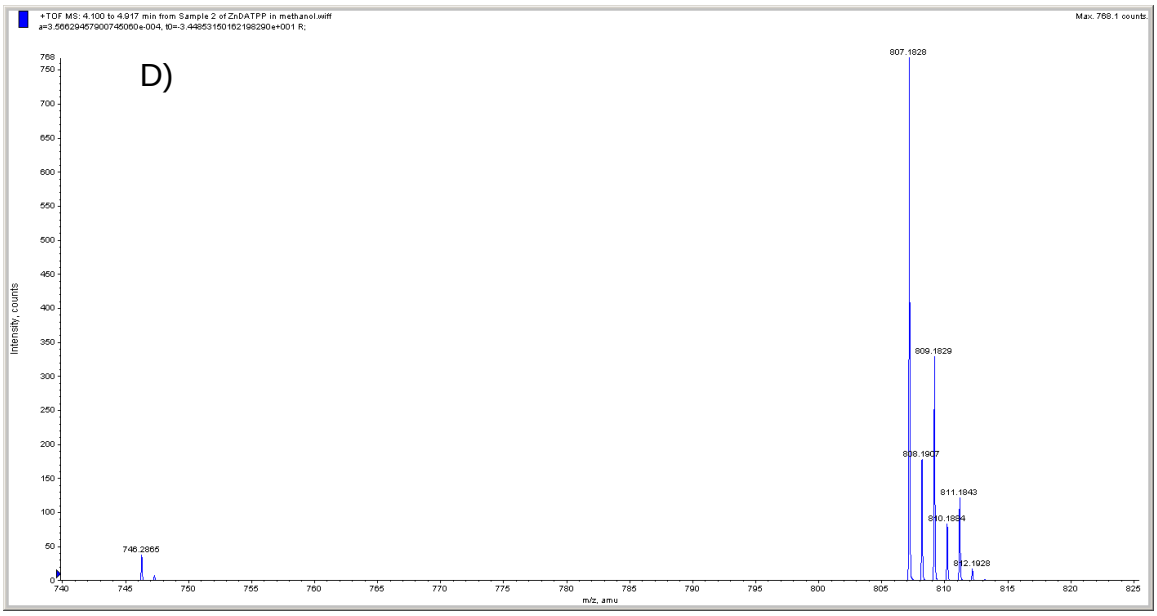

Figure A5.1. A) Synthetic scheme for the preparation of ZnDATPP; B) ^{1}H-NMR spectrum of ZnATPP; C) ^{1}H-NMR spectrum of ZnDATTP; D) Mass spectrum (ESI) of ZnDATTP.

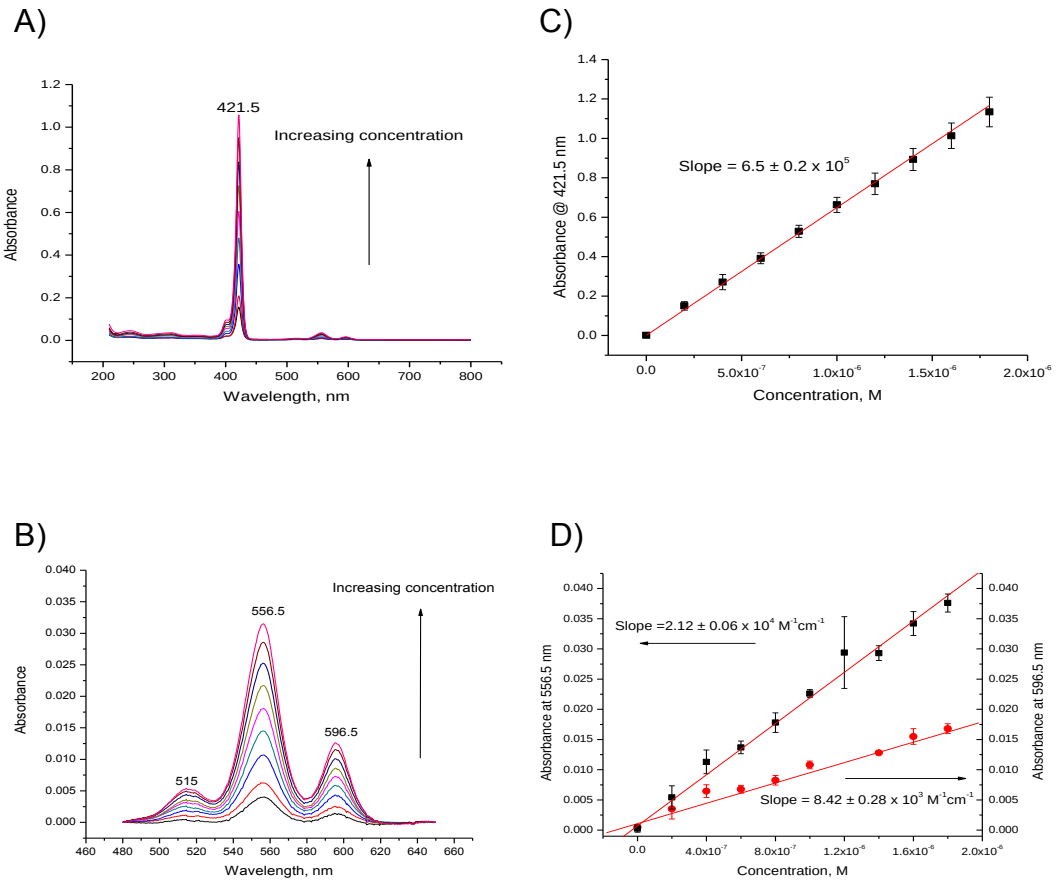

Figure A5.2. Baseline-corrected UV-Vis absorption spectra of 2.0 x 10^{-7} to 1.8 x 10^{-6} M ZnDATPP in methanol showing the typical absorption spectra of metalloporphyrins with the intense feature labeled at 421.5 nm assigned to the B(0,0) or Soret band. B) Enlarged Q-band region of the spectrum in A) showing the Q bands at 556.5 nm and 596.5 nm. Beer's law plots at C) 421.5 nm showing linear behavior with a calculated molar absorptivity equal to 6.5 ± 0.2 x 10^5 $M^{-1}cm^{-1}$ and at D) 556.5 nm and 596.5 nm with absorptivity values equal to 2.1 ± 0.1 x 10^4 $M^{-1}cm^{-1}$ and 8.4 ± 0.3 x 10^3 $M^{-1}cm^{-1}$, respectively.

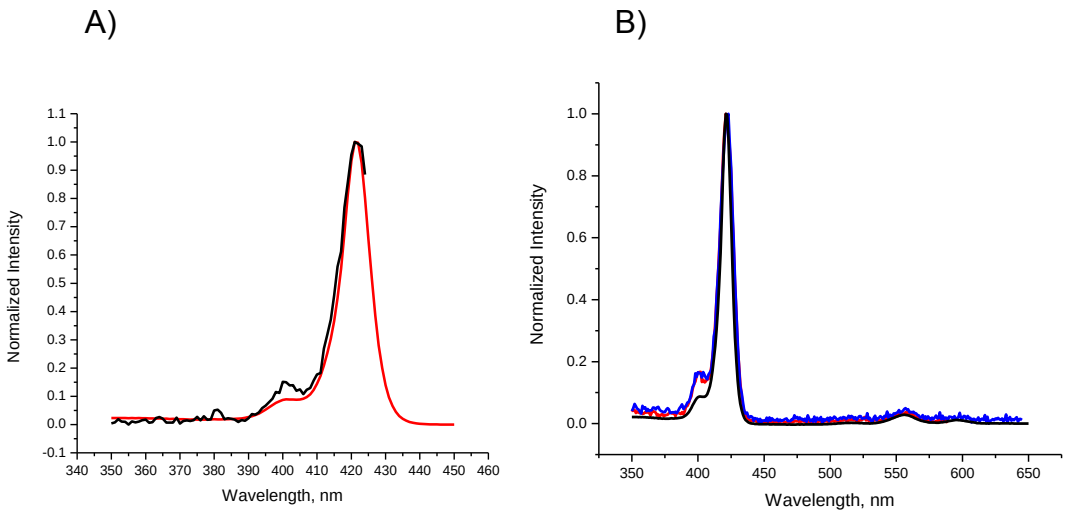

Figure A5.3. A) Excitation scan (black) and absorption spectrum (red) overlap for ZnDATPP in CH_3OH emission at 428 nm. B) Excitation scan and absorption spectrum (red) overlap for the sample fluorescence emission at 600nm (black) and 650 nm (blue).

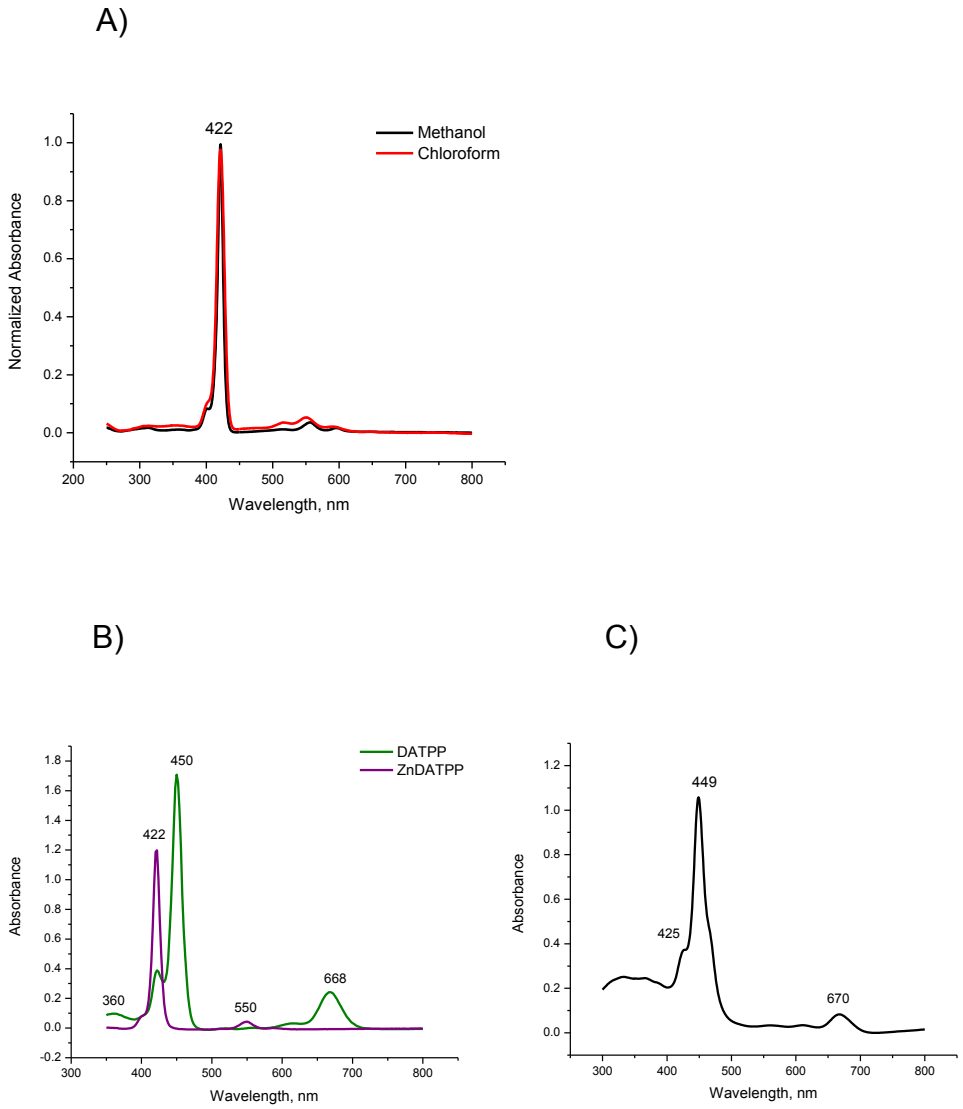

Figure A5.4. A) Comparison of absorbance spectra in methanol and chloroform; B) Comparison of absorbance spectra of DATPP and ZnDATPP in chloroform; C) Absorbance spectrum of ZnDATPP in chloroform after photodamage.

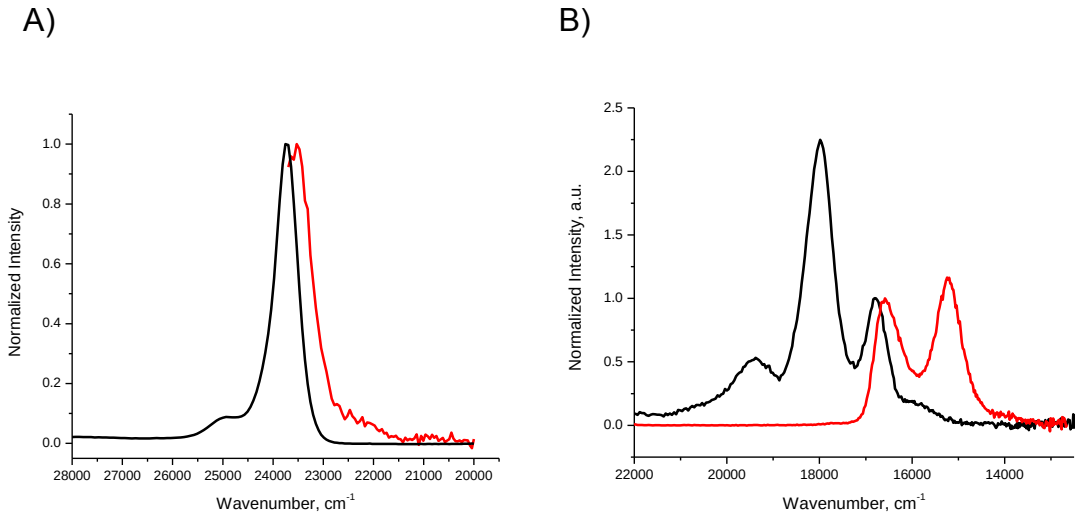

Figure A5.5. A) Normalized B-Band absorption and emission. B) Q band absorption and emission spectra normalized at the Q(0,0) position.

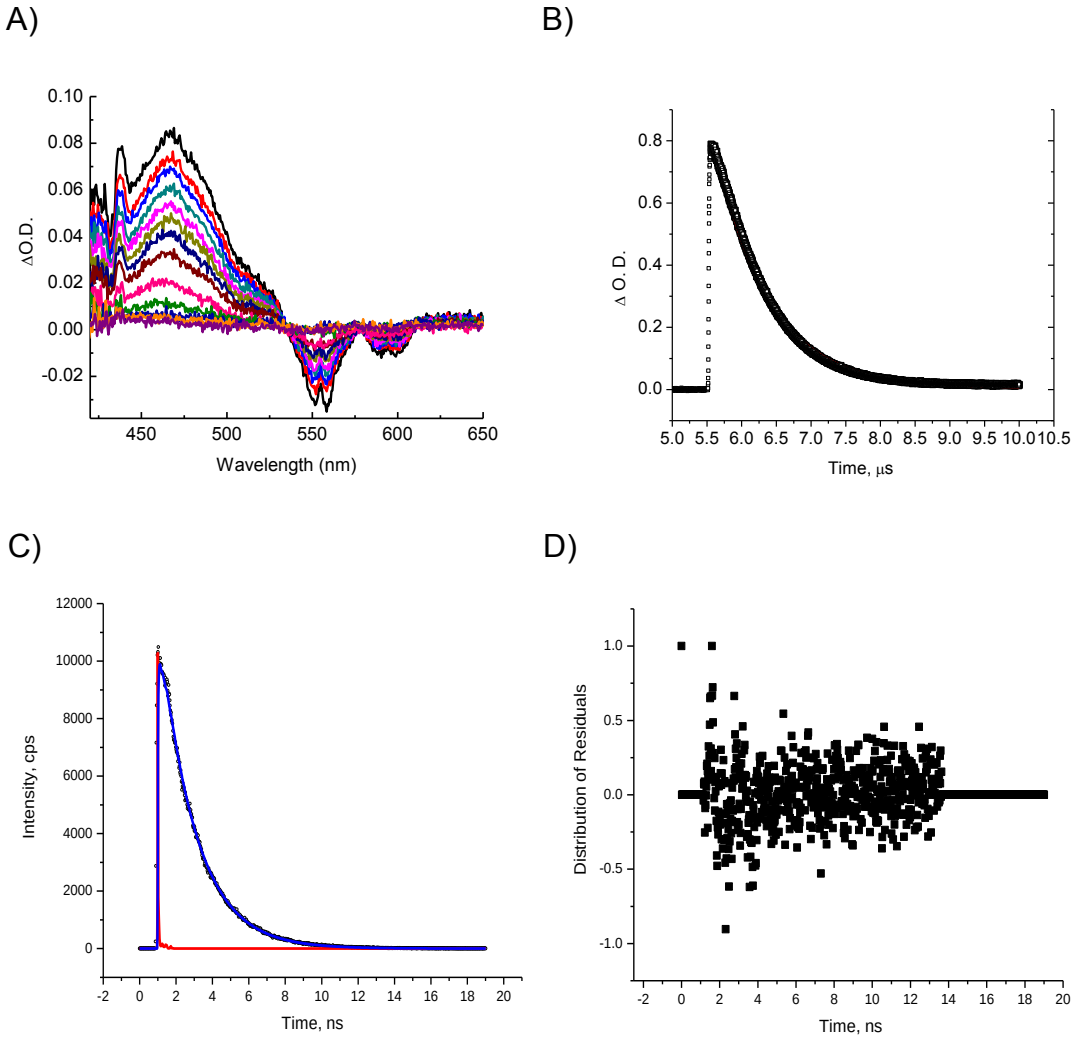

Figure A5.6. A) Transient absorption spectra of ZnDATPP in methanol, λ_{ex} = 532 nm. B) Triplet transient decay monitored at 467 nm (τ_T = 0.76 μs). C) First excited singlet state decay with λ_{ex} set at 400 nm and the emission monitored at 650 nm (τ_S = 1.90 ns). Open circles for B and C represent decay profile while the blue lines represent single exponential decay fit. The red curve in C is the instrument response function. D) Distribution of residuals for decay fit in C).

Table A5.1. Spectroscopic and photophysical data of ZnDATPP relative to ZnTPP.

	ZnTPP, benzene[77]	ZnDATPP, $CHCl_3$	ZnDATPP, CH_3OH
B band E_{max}^{abs}, cm^{-1}	23655	23724	23752
$E_{max,}^{em} cm^{-1}$	23501	23402	23529
S_2 – S_0 stokeshift	154	322	224
$Q^{0,0}$ band E_{max}^{abs}, cm^{-1}	17007	16949	16806
$E_{max,}^{em} cm^{-1}$	16722	16528	16556
S_1–S_0 stokeshift, cm^{-1}	285	421	350
Φ_f (S_1)	0.0348	0.0535	-
τ (S_1), ns	1.70	1.65	1.90

Table A5.2. Limiting mean molecular area of meso-tetrasubstituted porphyrin molecules with varying number of polar groups.

Porphyrin	Mean Molecular Area, nm^2	References
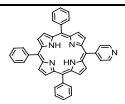	0.80	132
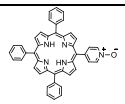	0.80	132
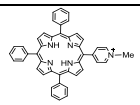	0.80	132
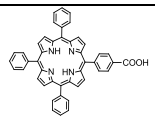	0.90,0.68	132, 136
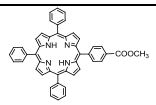	No monolayer, 0.46	132, 136
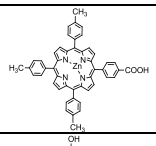	0.50	171
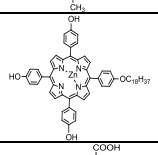	1.04	172
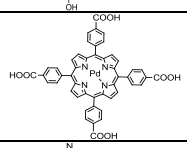	~0.70	137
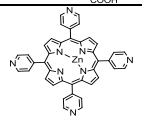	0.51, 0.65	134, 138

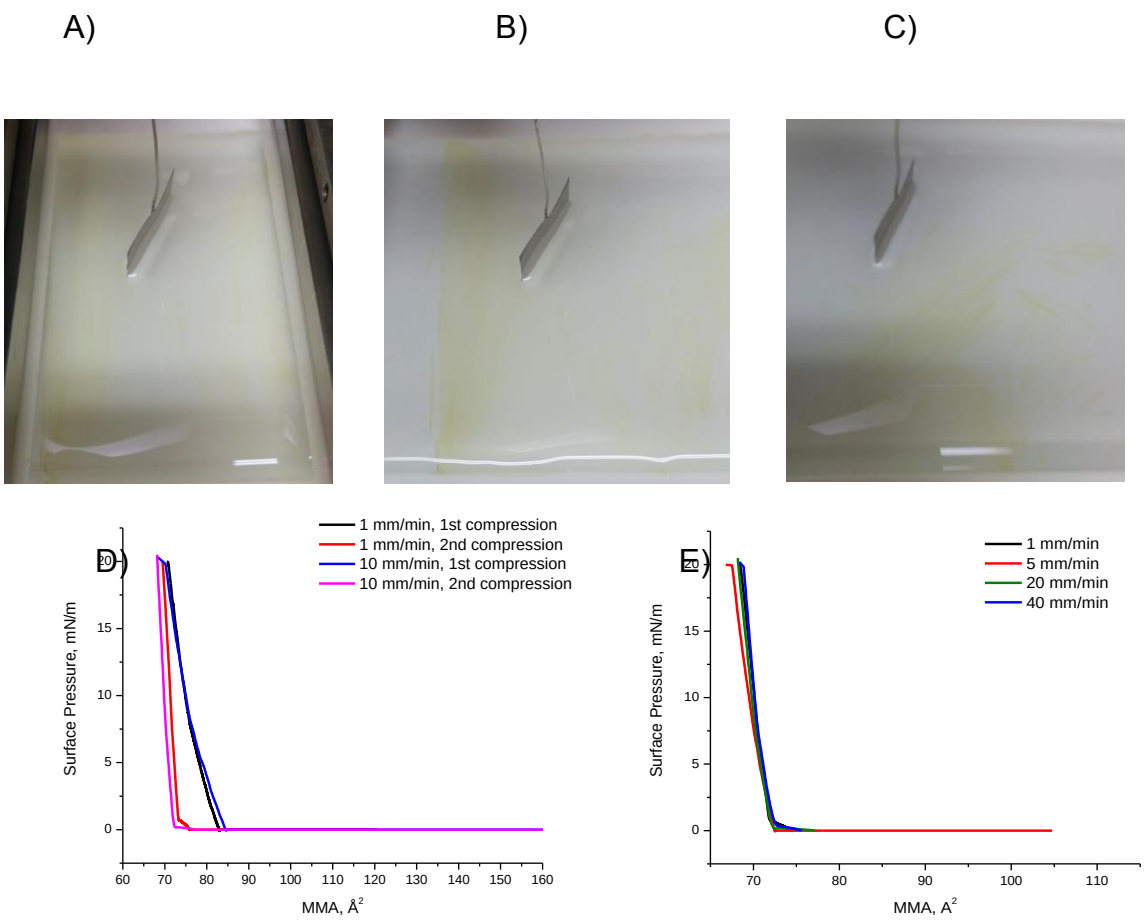

Figure A5.7. Photographs of ZnDATPP domains on the water surface after the first compression. A) compression to maximum π (>70 mN·m^{-1}) at a rate of 10mm/min. B) and C) Re-expansion to π = 0 mN·m^{-1}. D) Comparison of hysteresis profile of Langmuir monolayers compressed to π = 20 mN·m^{-1}at rates of 1mm·min^{-1} and at 10 mm·min^{-1}. E) π-A isotherms for the 2nd compression of the same Langmuir monolayers at varying compression rates.

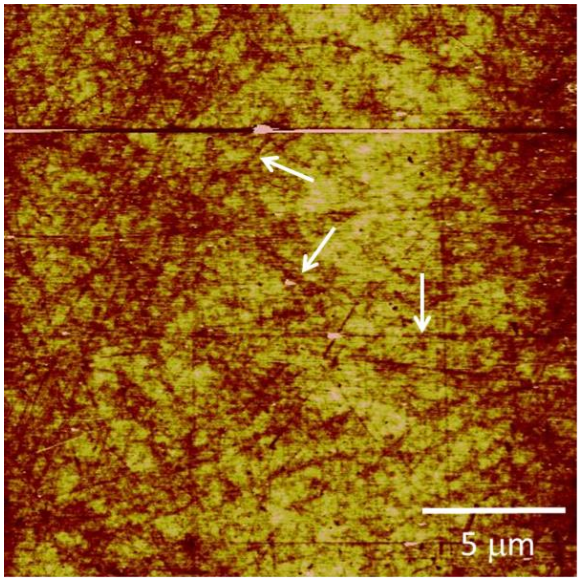

Figure A5.8. AFM image of ZnDATPP LB monolayer film deposited on quartz at 20 mN/m. Average RMS roughness of a 400 μm^2 was calculated to be 1.6 nm with skewness $>$ 0. Note the presence of lines crisscrossing the image (see arrows for examples). These correspond to the edges of ZnDATPP aggregates with different tilt directions.

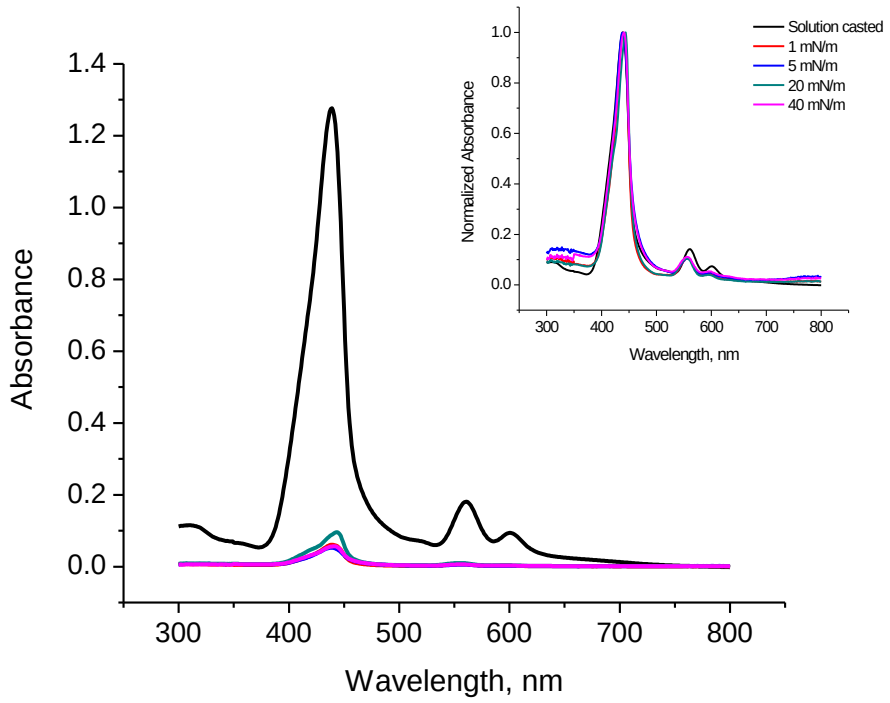

Figure A5.9. UV-Vis absorption spectra of solution cast ZnDATPP films and LB films prepared at different surface pressures. Varying the deposition surface-pressure varies the intermolecular distance of ZnDATPP in the LB film while solution cast film introduces high dye concentration on the substrate. Inset: Normalized UV-Vis absorption spectra showing the solution cast and LB films have the same profile.

Calculation of the excitation rate:

To estimate the number of population (from the ground state) which are pumped to the excited state are directly estimated by measuring the loss (including the care for attenuation / loss by bare solvent) in the laser power just by measuring the difference in power before and after the sample, as absorbed photons directly correspond to excited molecules (A1.1). For the ZnTPP systems singlet to triplet intersystem crossing efficiency

is near to 1 with rate of the order of ≤ nanoseconds. [1, 2] Therefore, such measurement can directly estimate the first excited triplet state population. (Experimental details: λ_{ex} = 532 nm, input power: 29 mW, 84% transmittance for cuvette (1 cm path length) + solvent, 93% transmittance for bare glass (0.5 mm thickness) film).

Table A5.3: Calculated number of excited triplets per second

Concentration / layers	Loss in power (mW)	Number of excited triplets/s
5 x 10^{-6} M	3.0	8 x 10^{15}
15-layers	1.0	2 x 10^{15}

$$\text{Number of incident photons per second} = \frac{\text{Power}}{\text{Energy of one photon of 532 nm}}$$

$$= \frac{\text{Power}}{hc/\lambda} \qquad \text{(A1.1)}$$

$$= \frac{\text{Power}}{3.73\times10^{-19}\,J}$$

where, h is Plancks' constant and c is the velocity of light.

Supporting Information for Chapter 6

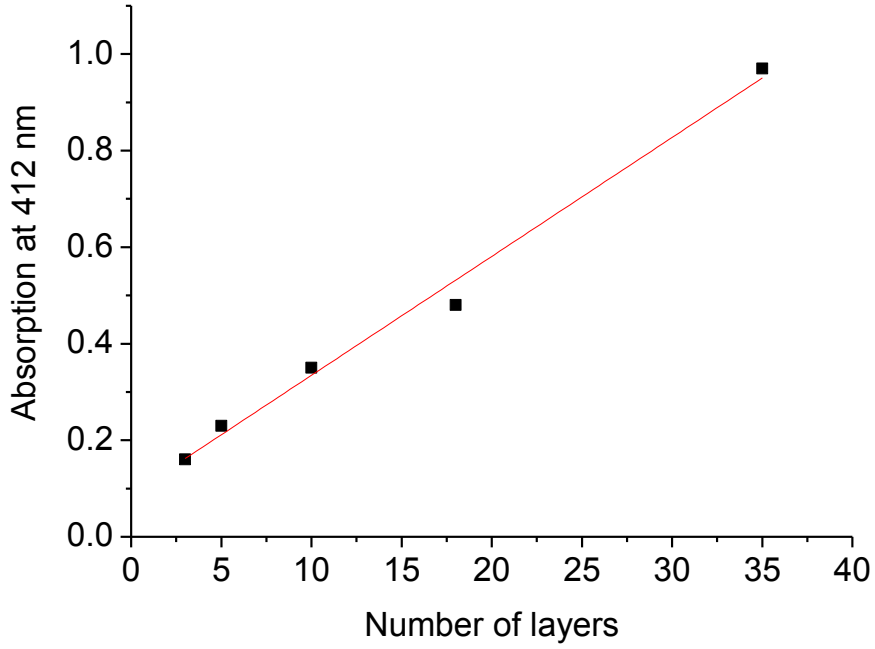

Figure A6.1 Plot of the absorption intensity at λ_{max} = 412 nm vs the number of dipping cycles. Equation of the line is y = 0.025x + 0.088; R^2 = 0.99

Table A6.1 Comparison of spectroscopic data for ZnTCPP in different matrices.

Spectroscopic Property	in Ethanol	in ZMPB/PVA	in ZMP/PVA	Literature[11]
λ_{max} (abs), nm				
Soret band	426	430	431	424
Q(1,0)	558	562	561	558
Q(0,0)	598	602	601	597
λ_{max} (em), nm				
Q(0,0)	604	604	604	602
Q(1,0)	658	658	658	654

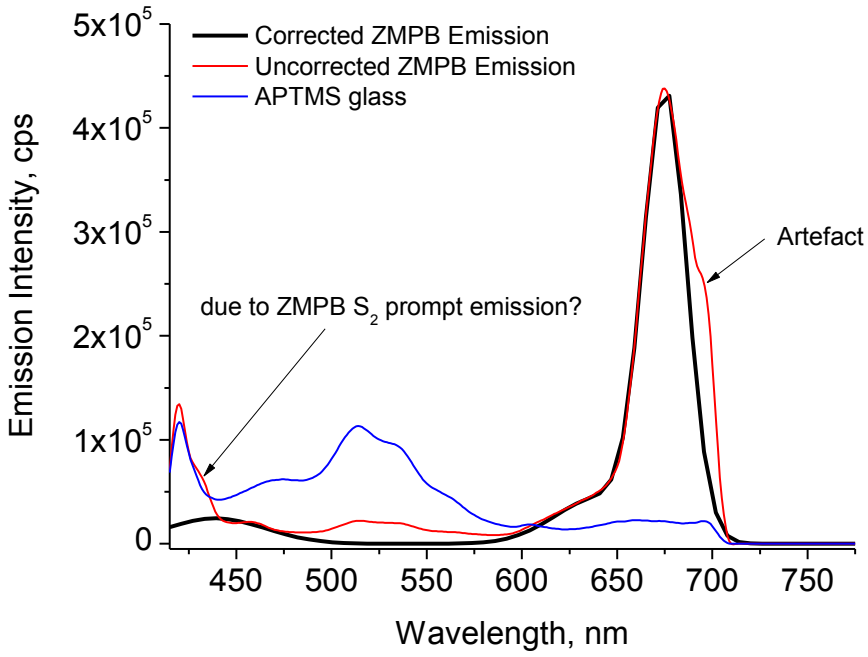

Figure A6.2 Emission spectrum of 35 layers of ZnTCPP-BPY MOF excited at 405 nm. The spectrum was corrected for emission of APTMS by fitting the curve with multiple Gaussians and subtracting the peaks ascribed to APTMS

Approximation of number of molecules required for NCPU-TTA

In Chapter 5, the molarity of ZnDATPP in solution, in which we observed NCPU-TTA was 5 x 10^{-6} M. Approximating the excitation path to be a cylinder with radius = 0.1 cm and length = 0.5 cm, the number of molecules required is:

$$N = MVN_A = \left(\frac{5\ x\ 10^{-6}\ moles}{1000\ cm^3}\right)(\pi)(0.05\ cm)^2(0.5\ cm)\left(\frac{6.02\ x\ 10^{23}\ molecules}{mole}\right)$$

$$= 1\ x\ 10^{13}\ molecules$$

The volume occupied by these number of molecules is given by:

$$V = (1\ x\ 10^{13} molecules)\frac{(1.6\ x\ 10^{-7} cm)(1.6\ x\ 10^{-7} cm)(1.2\ x\ 10^{-7} cm)}{ZMPB\ molecule}$$

$$= 5\ x\ 10^{-8} cm^3$$

and the thickness of the film necessary to have the required amount of molecules in the excitation path is:

$$h = \frac{V}{\pi r^2} = \frac{5\ x\ 10^{-8} cm^3}{\pi(0.05\ cm)^2} = 58\ nm$$

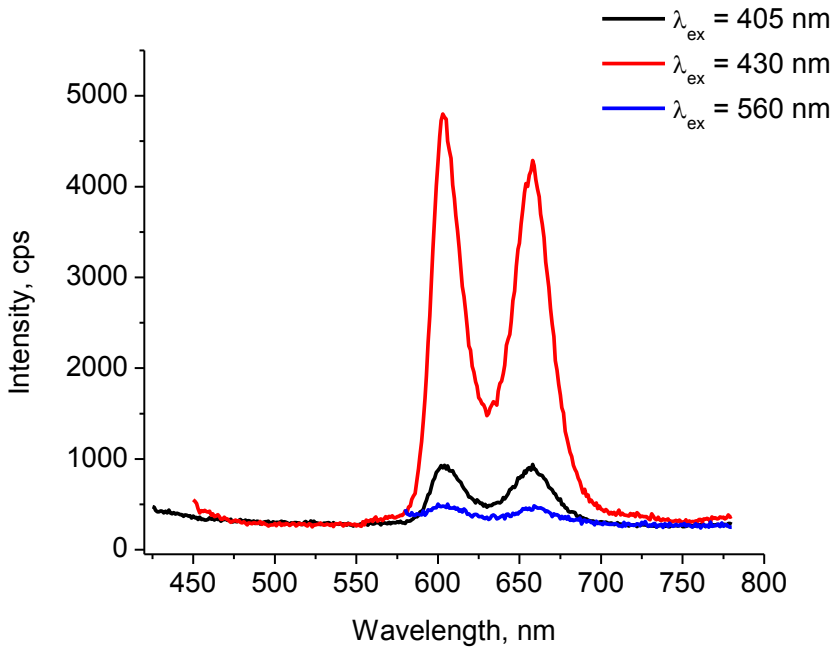

Figure A6.3. Emission spectra of ZMPB in PVA at different excitation wavelengths.

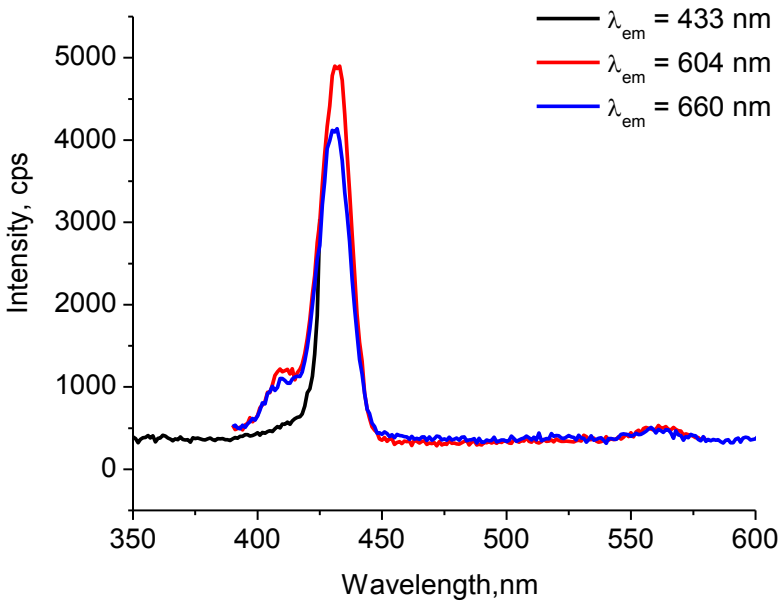

Figure A6.4. Excitation scans of the different emission peaks of ZMPB in PVA films.

Powder XRD Peak List

Table A6.2 Powder XRD peak list for ZMPB Crystals

No.	2θ (°)	d (Å)	Height (counts)	FWHM (°)	Int. I (counts·°)	Int. W (°)
1	5.33(3)	16.57(9)	583(24)	0.35(4)	315(32)	0.54(8)
2	7.65(3)	11.55(4)	843(29)	0.31(3)	337(26)	0.40(4)
3	9.37(4)	9.43(4)	349(19)	0.40(5)	149(42)	0.43(14)
4	9.86(5)	8.96(4)	468(22)	0.49(10)	242(43)	0.52(12)
5	10.61(4)	8.33(3)	298(17)	0.24(4)	76(23)	0.25(9)
6	11.13(7)	7.94(5)	262(16)	0.76(12)	212(37)	0.81(19)
7	15.112(13)	5.858(5)	1886(43)	0.534(16)	1352(40)	0.72(4)
8	17.098(17)	5.182(5)	436(21)	1.15(9)	592(38)	1.36(15)
9	21.20(5)	4.188(9)	124(11)	0.63(10)	128(17)	1.0(2)
10	22.87(2)	3.885(4)	192(14)	0.55(4)	136(17)	0.71(14)
11	31.8(3)	2.81(3)	24(5)	2.4(3)	61(11)	2.6(10)

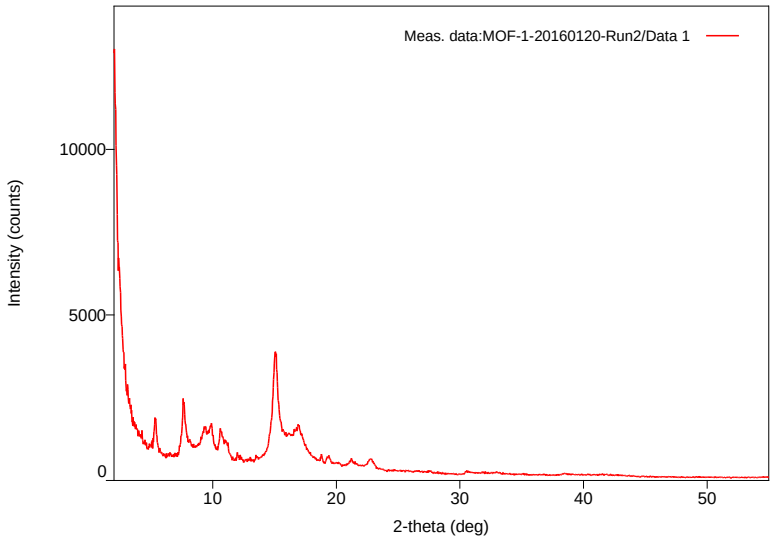

Figure A6.5 Powder XRD patterns for ZMPB.

Table A6.3 Powder XRD peak list for ZMP Crystals

No.	2θ(°)	d (Å)	Height (counts)	FWHM (°)	Int. I(counts·°)	Int. W(°)
1	5.39(4)	16.39(12)	250(16)	0.71(16)	268(41)	1.1(2)
2	7.55(3)	11.70(4)	822(29)	0.84(5)	1326(38)	1.61(10)
3	18.231(7)	4.8623(19)	4964(70)	0.408(8)	2944(24)	0.593(13)
4	22.68(3)	3.917(5)	317(18)	0.61(5)	383(11)	1.21(10)
5	30.39(3)	2.939(3)	113(11)	0.18(3)	24(4)	0.22(5)
6	33.30(15)	2.688(11)	21(5)	2.0(4)	59(10)	2.8(11)

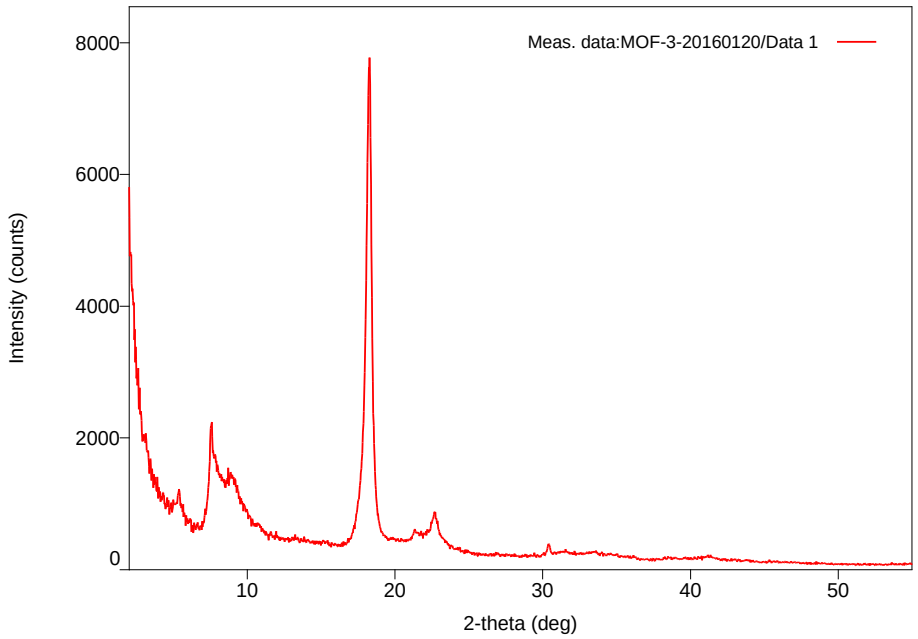

Figure A6.6 Powder XRD patterns for ZMP.